UNIVERSITY OF ZURICH, INSTITUTE OF ORGANIC CHEMISTRY

# HEMIPORPHYRAZINES

## SYNTHESIS, PHOTOPHYSICAL PROPERTIES & REACTIVITY

MASTER THESIS

SABRINA MANUELA HUBER

ZURICH, MAY 2012

*Nur lebende Fische schwimmen gegen den Strom…*

# *ABSTRACT*

DNA quadruplex structures are attracting great scientific interest because of increasing evidence that these structures play important roles in biological processes ranging from replication, transcription, and recombination to telomere integrity. The use of small molecules to selectively target these structures *in vivo* is emerging as a promising way to interfere with telomere replication in tumor cells and provides potential anticancer agents. A large number of quadruplex binding ligands have already been reported. In general, they selectively interact with terminal GGGG-tetrads via π-π stacking interactions. However, in addition to GGGG-tetrads, GCGC-tetrads are known to be involved in quadruplex formation *in vitro*. Even though these so-called "mixed tetrads" might also have biological relevance, selective GCGC-tetrad binding probes have not yet been reported.

Hemiporphyrazines (Hps) are non-aromatic, 20 π-electron phthalocyanine (Pc) derivatives that consist of two co-facial pyridine rings and two co-facial isoindole units linked through four aza bridges. Due to their planarity, extended π-conjugation, and $C_2$-type symmetry, they are good candidates for selectively targeting GCGC-tetrads. Unsubstituted Hps are, however, notoriously insoluble materials and therefore little is known about their chemical and photophysical properties. As a consequence, this Master thesis is focused on the synthesis, structure, photophysical and reactivity properties of Hps to assess their potential as future GCGC-tetrad binding ligands.

Free-base hemiporphyrazine ($HpH_2$) was synthesized and its structure was analyzed by single crystal X-ray diffraction. $HpH_2$ adopts a nearly planar structure and its macrocyclic core contains alternating double and single bonds. This is consistent with the non-aromatic character of these compounds. Furthermore, $HpH_2$ has a very high water affinity and readily absorbs water from the atmosphere to form a yellow monohydrate ($HpH_2 \cdot H_2O$). This compound has a saddle-shaped conformation and distinct photophysical properties.

The use of bulky metal triflates ($M(OTf)_2$) as sources of metal ions during macrocyclization furnished metallo Hps (MHps) with enhanced solubility properties. Octahedral zinc and nickel *trans*-ditriflate hemiporphyrazine complexes "$HpH_2Zn(OTf)_2$" and "$HpH_2Ni(OTf)_2$" provide two such examples.

In contrast to $HpH_2$, these compounds are highly soluble in MeOH, DMSO, and DMF. X-ray diffraction analysis of $HpH_2Zn(OTf)_2$ and $HpH_2Ni(OTf)_2$ confirmed that the Hp scaffold is largely unaffected by the introduction of $M(OTf)_2$. In both cases, a neutral Hp ligand adopts a planar conformation and exhibits similar trends in bond lengths as compared to $HpH_2$.

$HpH_2Zn(OTf)_2$ was used as soluble model of planar Hps to investigate the photophysical and reactivity properties of the Hp scaffold in solution. Soluble aggregates and crystalline materials of planar hemiporphyrazines exhibit relatively strong absorbance of visible light (450 nm – 600 nm) and red luminescence (600 nm – 700 nm). The saddle-shaped hemiporphyrazine monohydrate ($HpH_2 \cdot H_2O$), in contrast, exhibits very little absorbance of visible light in solution and in the solid state. Upon photoexcitation at 380 nm, $HpH_2Zn(OTf)_2$ and $HpH_2$ exhibit multi-wavelength emissions centered at 450 nm and 650 nm. The emissions at 450 nm are highly anisotropic, while the emissions at 650 nm are fully depolarized with respect to a plane-polarized excitation source. These results suggest that excitonic coupling of aggregated and crystalline hemiporphyrazines results in increased absorbance and emission of visible light from $S_0 \leftrightarrow S_1$ transitions that are usually symmetry-forbidden in isolated species. Previous theories proposed that the dual-wavelength emission of Hps is a result of excited state intramolecular proton transfer (ESIPT). However, $HpH_2Zn(OTf)_2$ is incapable of ESIPT, but nevertheless shows concentration-dependent dual-wavelength emission. Consequently, it is hypothesized that the true basis of this feature is due to emissive $S_1 \rightarrow S_0$ and $S_2 \rightarrow S_0$ transitions in aggregated and crystalline hemiporphyrazines. These results provide important new design considerations for Hp-based materials by highlighting the differences in photophysical properties of planar versus non-planar Hps as well as the presence of excitonic luminescence from aggregated and crystalline Hps.

Due to its non-aromatic, 20 π-electron system, the Hp scaffold is reactive towards chemical modifications. Upon palladium catalyzed hydrogenation, $HpH_2Zn(OTf)_2$ absorbs two equivalents of hydrogen directly to the macrocyclic core to furnish a new compound "$HpH_4Zn(OTf)_2$". This compound is stable towards atmospheric oxidation at room temperature, but is dehydrogenated to $HpH_2Zn(OTf)_2$ in nitrobenzene solution at 180 °C. Hydrogenation is associated with a change in conformation from planar to saddle-shaped as well as a color change from red to yellow. The absorption of $HpH_2Zn(OTf)_2$ in the visible region of the electromagnetic spectrum is blue-shifted from 530 nm to 460 nm upon reduction.

The synthesis of water soluble Hps is essential for the evaluation of the Hps' stability in neutral aqueous solution and their potential as GCGC-tetrad selective probes. As a consequence, various substituted phthalonitrile as well as 2,6-diaminopyridine precursors were synthesized that will be used in subsequent macrocyclization reactions. The resulting water soluble Hps will then be subjected to direct GCGC-tetrad binding assays, cellular uptake, and cytotoxicity studies to evaluate the Hps' potential as GCGC-tetrad ligands.

# *ACKNOWLEDGEMENT*

The accomplishment of this Master thesis was made possible by the essential contributions of many people who supported me all along the way with ideas, advice, encouragement, services, and good company. In particular, I would like to express my sincere gratefulness to:

*Prof. Dr. Nathan W. Luedtke* for his continuous guidance and support. His excellent cooperation and continuous enthusiasm strongly contributed to the realization of this work.

*Martin Seyfried* for his outstanding assistance at the beginning of this project. His thoughts and ideas helped to develop the objectives of my Master thesis.

*Jean-Christophe Prost* and *Urs Stalder* for measuring all mass spectra as well as *PD Dr. Anthony Linden* for X-ray crystal structure determinations.

The present and past members of the Luedtke group, especially *Fabian Roth*, *Marco Brandstätter,* and *Ulrieke Rieder* for the pleasant working atmosphere, joyful coffee breaks, and revision of this work.

My family, especially my parents, *Beat* and *Elisabeth Huber*, for their financial assistance and constant support of my personal ambitions and *Sandro Freiermuth* for his encouragement and understanding.

# *TABLE OF CONTENTS*

# *LIST OF FIGURES AND SCHEMES*

***Figures:***

***Schemes:***

# *CHAPTER 1*

# *INTRODUCTION*

## *1.1 Double-Stranded DNA and its Topologies*

Deoxyribonucleic acid (DNA) stores all the genetic information required for the development and functioning of living organisms. It consists of two intertwined, linear polymers which are assembled from four different nucleotides of variable order. A single nucleotide is composed of a nitrogenous base (adenine (A), guanine (G), cytidine (C), or thymidine (T)), a pentose (2'-deoxyribose), and a phosphate group. Together, the nucleobase and the sugar, joined via a β-N-glycosidic bond, define a nucleoside. The phosphate units bridge the nucleosides via phosphodiester bonds at the 3'-OH and 5'-OH of the pentose, forming the sugar-phosphate DNA backbone (Figure 1.1, left).

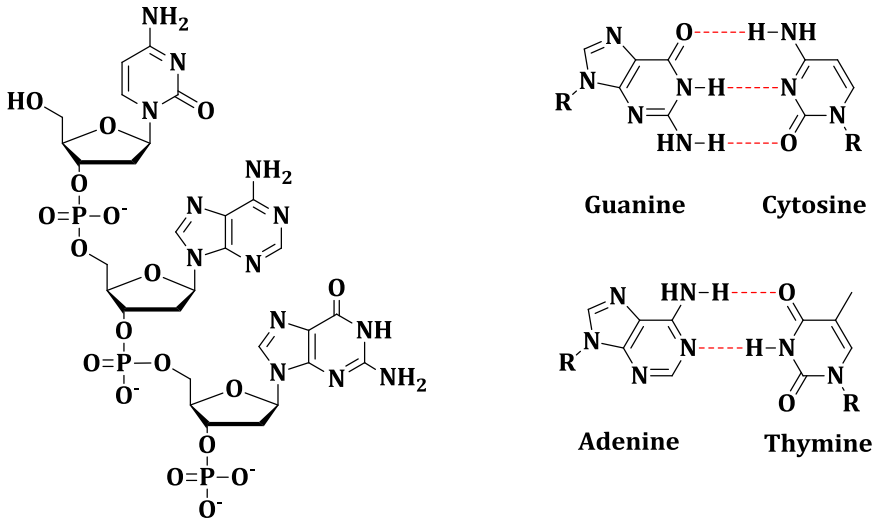


**Figure 1.1:** Left: Schematic composition of a DNA strand; Right: Canonical Watson-Crick base pairing between G & C and A & T.

DNA was first discovered inside the nuclei of human white blood cells by the Swiss physiological chemist Friedrich Miescher in 1869,[1] but it was not until 1953 that the topology of the double-stranded B-DNA was solved by Watson and Crick with the help of over 80 years of accumulated experimental data.[2] The structure is characterized by two anti-parallel polynucleotide strands which form a right-handed double helix defined by a major and a minor groove (Figure 1.2, middle). While the sugar-phosphate backbone winds around the outside of the helix, the bases stack on top of each other in the core of the helical structure. The topology of DNA is stabilized by canonical Watson-Crick base pairing (Figure 1.1, right), where G interacts with C via three hydrogen bonds and A forms two hydrogen bonds with T. The B-DNA helix makes a turn every 3.4 nm and the distance between two neighboring base pairs measures 0.34 nm. This results in about 10 base pairs per turn for an ideal helical arrangement (Figure 1.2, middle).

Double-helical DNA can adopt several distinct topologies depending primarily on the base sequence and solvent composition. Apart from the well-known B-DNA, which predominates *in vivo* under relative high humidity conditions, A-DNA (Figure 1.2, left) and Z-DNA (Figure 1.2, right) are the major two structural variants.[3]

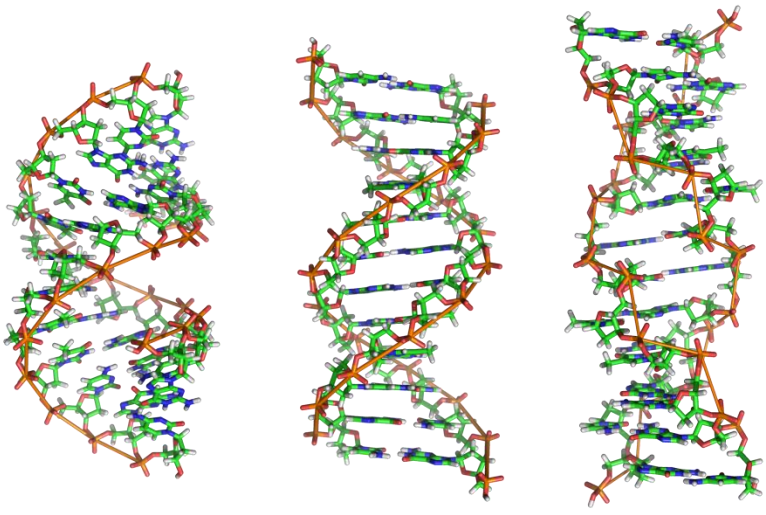

A-DNA B-DNA Z-DNA

**Figure 1.2:** Three major structural variants of double-helical DNA.[4]

A-DNA is a right-handed double helix fairly similar to B-DNA, but with a more contracted helical structure. It mainly exists under dehydrating low humidity conditions[5], has 11 residues per rotation, and a smaller rise/turn compared to B-DNA. This results in a deepening of the major and a shallowing of the minor groove. The base pairs of A-DNA are considerably displaced from the helical axis and are inclined to it by ~ 20° (Figure 1.2, left).[3] The planes of the nucleotide bases in B-DNA, in contrast, are nearly perpendicular to the helical axis (Figure 1.2, middle).

Z-DNA is a left-handed duplex structure with a dinucleotide repeat unit which is generally confined to alternating deoxyguanosine and deoxycytidine residues (Figure 1.2, right).[3, 6] While the deoxycytidines are in the *anti*-conformation (Figure 1.3, left), the deoxyguanosines are in the unusual *syn*-orientation with respect to the sugar (Figure 1.3, right).[7] The characteristic zigzag backbone of Z-DNA is a result of these alternating *syn*-/*anti*-conformations of the nucleobases around the glycosidic bond. Normally, the *syn*-conformation of pyrimidines is unstable because of sterical interference between the sugar residue and the pyrimidine oxygen atom double bonded to C2.

In Z-DNA, there is a single narrow groove corresponding to the minor groove of B-DNA. There is no major groove. The formation of this structure is generally unfavorable, but it can be promoted by alternating purine-pyrimidine sequences, negative DNA supercoiling, and high salt concentrations that reduce the electrostatic repulsion between the two closest phosphate groups.

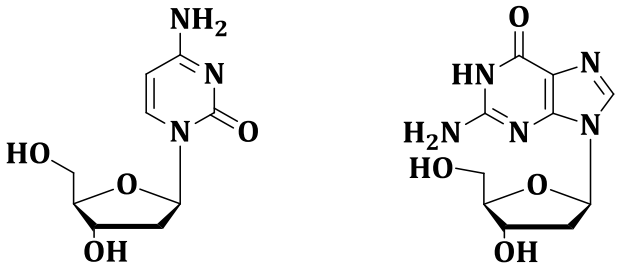


***anti*-Cytidine** ***syn*-Guanosine**

**Figure 1.3:** *Anti*-cytidine (left) and *syn*-guanosine (right).

### *1.2 Single-Stranded DNA and its Topologies*

Double-stranded DNA is of great importance for information storage when it is packed as chromatin. However, during metabolically active processes like replication and transcription a single-stranded DNA template is transiently required. Single-stranded DNA is therefore sometimes considered as biologically relevant, while the duplex structure can be regarded as the biologically inactive form. DNA is not limited to double-helical conformations, but is a highly flexible and dynamic macromolecule that can fold into a wide variety of single-stranded structures. Hairpin, triplex, G-quadruplex, and i-motif are examples of well-defined single-stranded DNA structures (Figure 1.4).

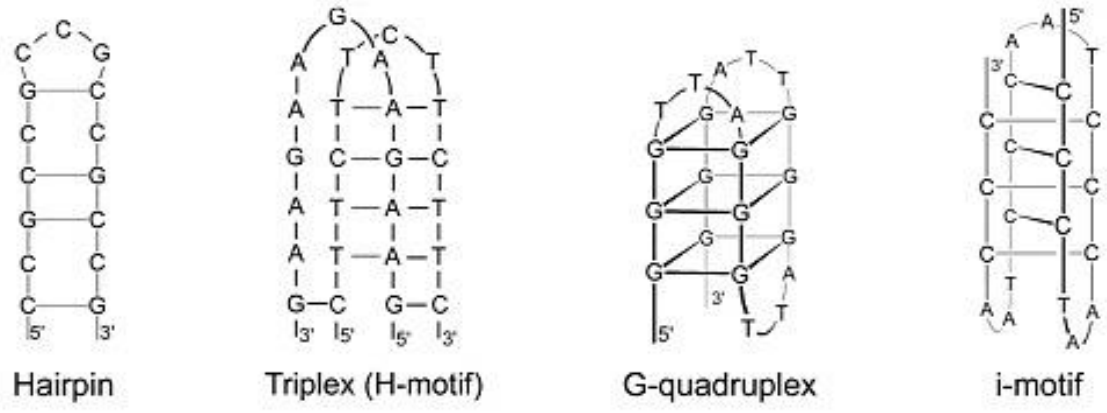


**Figure 1.4:** Examples of secondary structures that can be adopted by single-stranded DNA.

DNA sequences, capable of adopting single-stranded structures *in vitro*, appear frequently in biologically significant regions of the eukaryotic genome, namely in promoter regions and around recombination hotspots, suggesting that they may play a regulatory role *in vivo*.[8] Their formation is largely controlled by the types of hydrogen-bonding patterns that nucleic acids can adopt. In addition to the classical Watson-Crick base pairs A·T and G·C, a plethora of non-canonical base pairing can occur, including Hoogsten, and hemiprotonated $C^{+}$·C base pairing (Figure 1.5).[9]

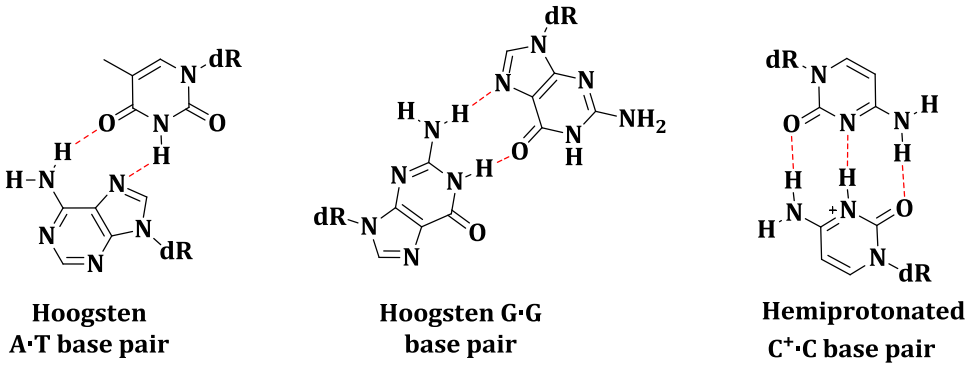


**Figure 1.5:** Non-canonical base pairing present in single-stranded DNA structures.

While Hoogsten hydrogen bonding stabilizes triple helix-containing and G-quadruplex structures, hemiprotonated $C^+$·C pairs are observed in i-motif structures. The latter are four-stranded structures formed by two intercalated cytidine-rich duplexes at slightly acidic pH (Figure 1.4).[10]

### *1.3 G-Quadruplexes*

G-quadruplexes are tetrastranded helices formed by guanosine-rich nucleic acids.[11] They are characterized by the vertical stacking of two or more G-tetrads (or G-quartets) arising from the co-planar, $C_4$-symmetric arrangement of four guanines which interact through hydrogen bonds between the Watson-Crick edge of each guanine base and the Hoogsteen edge of its neighbor (Figure 1.6).[11] There is a pronounced channel of negative electrostatic potential along the vertical axis of a G-quadruplex because of the closely-spaced guanine oxygen atoms that point all towards the center of a G-quartet. Monovalent cations can engage in electrostatic interactions with the sugar-phosphate backbone and the guanine carbonyl groups within this channel and stabilize quadruplexes according to the following order: $K^+ > NH_4^+ > Na^+ > Li^+$, due to the relative desolvation energies and ionic radius for optimal sphere coordination within the quadruplex cavity.[12] The selective stabilization of G-quadruplexes by potassium ions *in vitro* occurs already at potassium ion concentrations in the range of 10 mM – 50 mM which is well below the 120 mM of KCl usually present in cells.[13] Nevertheless, the existence of G-quadruplexes has not yet been definitively demonstrated in living mammalian cells or whole organisms.

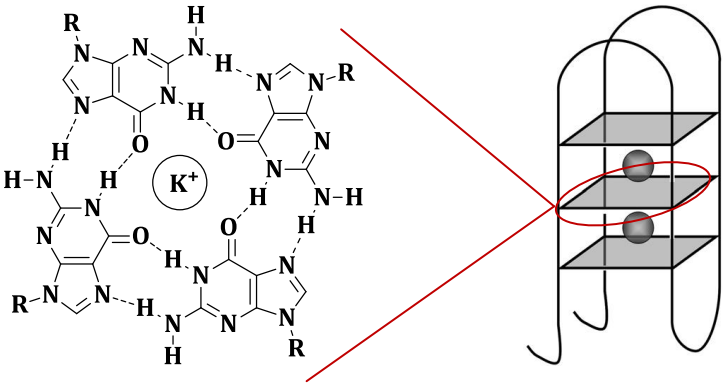


**Figure 1.6:** Left: Structure of a G-quartet, with four guanines arranged around a central potassium ion; Right: Schematic representation of a cation-stabilized G-quadruplex consisting of three stacked G-quartets.

G-quadruplexes exhibit highly diverse structural polymorphism depending on the number of strands involved, strand orientation, variation in loop size, the kind of ions present, and the nucleic acid sequence (Figure 1.7).[14-18] G-quadruplexes can be formed from one (intramolecular), two (bimolecular), or four (tetramolecular) strands of DNA. Depending on the conformation of the glycosidic bond between the guanine base and the sugar, the adjacent strands of a G-quadruplex may run in a parallel or an anti-parallel way. Tetramolecular G-quadruplexes typically contain parallel strands with all bases in *anti*-conformations (Figure 1.7, A). Complexity arises in bimolecular quadruplexes due to the necessity of loop formation to connect the two strands. These loops can be diagonal (linking diagonally opposite anti-parallel strands (Figure 1.7, B)), lateral (linking adjacent anti-parallel strands (Figure 1.7, C)), or external (around the side of the structure linking parallel strands (Figure 1.7, E)). Intramolecular G-quadruplexes give rise to highly complex topologies containing diagonal, lateral, or external loops, depending on the nucleic acid sequence (Figure 1.7, D and E).[19]

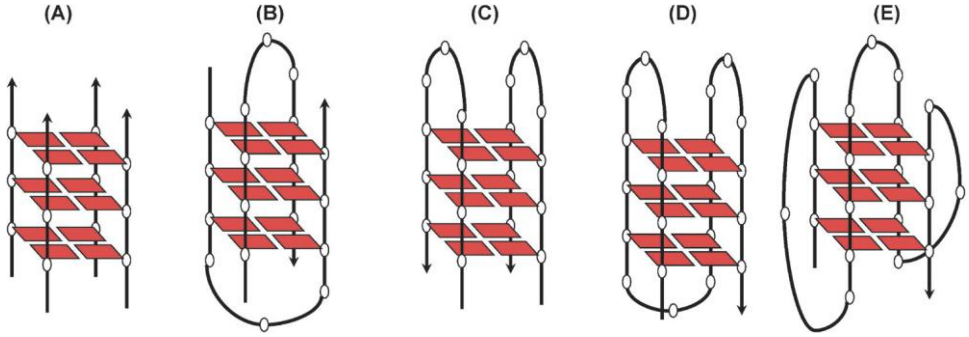


**Figure 1.7:** Structure and topology of G-quadruplexes: (A): Tetramolecular with parallel strands; (B): Bimolecular with diagonal loops; (C): Bimolecular with lateral loops; (D): Unimolecular with lateral loops; (E): Unimolecular with one diagonal and two external loops.[19]

While the presence of G-quadruplexes in humans is still an open question, evidence for their occurrence in genomic DNA is accumulating. Bio-informatic analyses have identified more than 375'000 sequences in the human genome with propensity to fold into G-quadruplexes.[20] Interestingly, these sequences were overrepresented in promoter regions of proto-oncogenes and the 3'-telomeric ends of chromosomes (telomeres) and less abundant in tumor-suppressor genes and open reading-frames.[21] Furthermore, DNA sequences with the ability to form G-quadruplexes are involved in the regulation of gene transcription, recombination, programmed cell death, and chromosome stability.[22-24]

Telomeres, located at the ends of chromosomes, consist of DNA tandem repeats whose integrity is required for the cell to avoid sequence loss during cell division, end-to-end fusion of non-homologous chromosomes, and attack by nucleases (Figure 1.8). In eukaryotes the telomeric nucleotide repeat is TTAGGG, with telomere length varying from 5 kb to 15 kb.[25-27] The terminal 150 - 200 bases at the 3' end of human telomeres form a single-stranded overhang whose exact structure is not yet fully established, although loop-type arrangements have been suggested from electron microscope studies.[25-27] Since DNA polymerase is unable to completely replicate the lagging strand, telomeres shorten in somatic cells due to DNA replication by 50 - 200 bases after each cell division. When the telomeres are shortened to a critical length (Hayflick limit) the somatic cells stop dividing and undergo senescence.

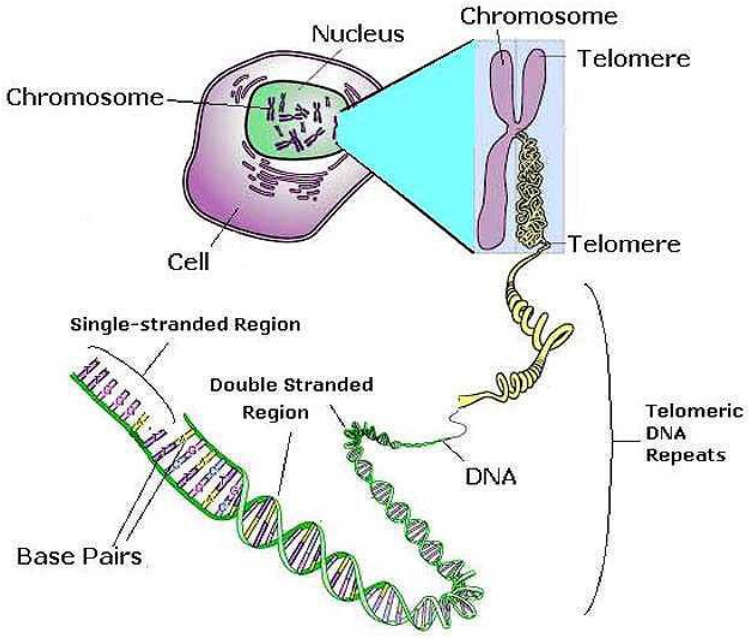


**Figure 1.8:** Schematic representation of telomeres.[28]

Tumor cells can maintain their telomere length due to the over-expression of telomerase. This reverse transcriptase enzyme catalyzes the synthesis of telomeric DNA repeats using an RNA template. It prevents progressive telomere shortening in cancer cells and supports their immortalization. Since telomerase is over-expressed in 80 – 85 % of cancer types and undetectable in most normal somatic cells, it is an interesting target for cancer therapeutics.[29] It has been reported that the folding of the 3' single-stranded overhang into G-quadruplex structures inhibits telomerase activity (Figure 1.9, right). Furthermore, G-quadruplex formation can influence gene expression of *c-myc, c-kit*, and *K-ras* which are all involved in carcinogenesis.[30-32] This suggests that G-quadruplexes in promoter regions are capable of inhibiting oncogene transcription (Figure 1.9, left).

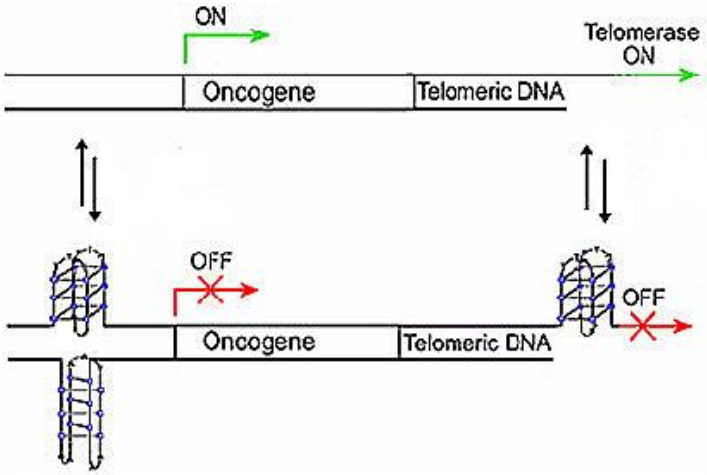


**Figure 1.9:** Schematic representation of the potential roles of G-quadruplexes in the control of oncogene expression (bottom, left) and telomerase inhibition (bottom, right).[13]

### *1.4 G-Quadruplex Binding Ligands*

The potential abilities of G-quadruplexes to inhibit telomere extension and oncogene transcription has generated great interest in the design and synthesis of small molecules that stabilize G-quadruplex structures and prevent the growth of cancer cells *in vivo*. A large number of G-quadruplex ligands have already been reported that display varying degrees of affinity and specificity for G-quadruplex DNA.[33-39] Most of these compounds are planar, hetero-aromatic systems which interact with external G-quartets via π–π stacking.

In addition to the external G-tetrads, other structural features of G-quadruplexes including the loops, grooves, and central channel have been targeted by the design of small molecules (Figure 1.10). G-quadruplex ligands can be divided into three main categories: π–π stacking, groove/loop binding, and central channel binding ligands. While the π–π stacking small molecules represent the most studied and sophisticated class of G-quadruplex ligands, the latter two categories comprise only a few examples and still require much development.

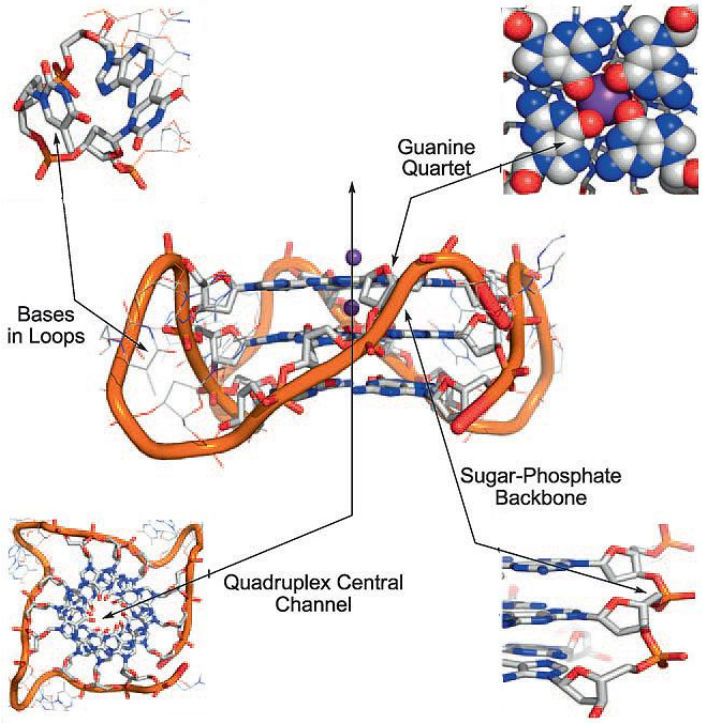


**Figure 1.10:** Structural features of a G-quadruplex that can be targeted for selective recognition.[40]

*1.4.1 π– π Stacking Ligands*

The majority of π–π stacking ligands contain a planar surface with extended π–conjugation that selectively stacks on top of G-tetrads. Initially, DNA intercalating agents were designed for quadruplex binding, assuming that such ligands will intercalate between stacked G-quartets. Haider *et al.* developed an acridine derivative substituted at 3- and 6-positions with 3-pyrrolidinopropionamide (BSU6039) (Figure 1.11, A1) and studied its interaction with the *Oxytricha nova* telomeric DNA sequence d(GGGGTTTTGGGG) by crystallographic analysis.[41] They found that the heterocyclic acridine system stacks on an external G-quartet (end-stacking) whereas the amine-containing side arms, protonated under physiological conditions, are involved in electrostatic interactions with the negatively charged sugar-phosphate backbone of G-quadruplex DNA. Their observation that the aromatic moiety of the ligand interacts with the G-quartets via end-stacking rather than being intercalated between two G-quartets of a quadruplex, was in agreement with earlier NMR and molecular modeling studies conducted with a wide variety of ligands and quadruplexes.[42, 43]

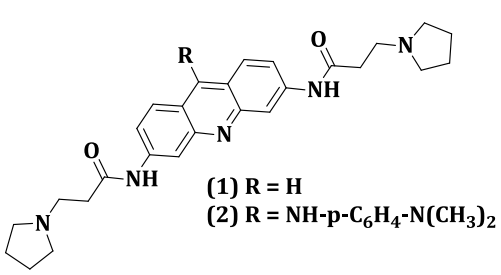


**A** (1) BSU6039, (2) BRACO-19

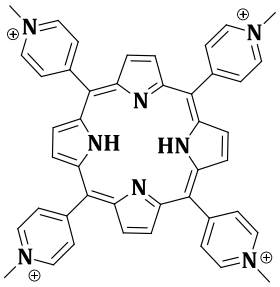

**B** TmPyP4

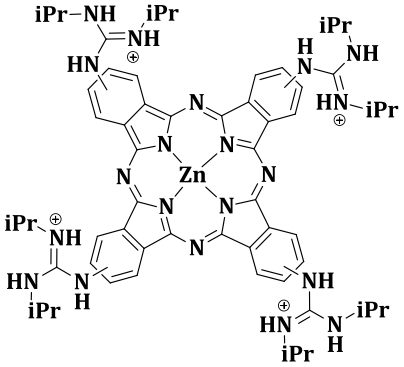

**C** Zn-DIGP

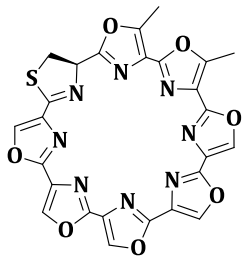

**D** Telomestatin

**Figure 1.11:** G-quadruplex π–π stacking ligands.

The information obtained from the BSU6039 crystal structure was used to design BRACO-19 (Figure 1.11, A2). Due to the presence of an additional substituent on the acridine ring system, this compound is able to interact with three G-quadruplex grooves. As a consequence, the compound shows a higher degree of stabilization and quadruplex vs. duplex selectivity than BSU6039. In addition, it was reported that BRACO-19 inhibits telomerase activity ($IC_{50}$ = 115 nM) and cancer cell proliferation.

Porphyrin-based aromatic systems with N-methyl groups have also been investigated as selective G-quadruplex ligands. A well-studied example is *meso*-5,10,15,20-tetrakis-(N-methyl-4-pyridyl)porphine (TMPyP4, Figure 1.11, B). It inhibits telomerase activity ($IC_{50}$ = 0.7 - 10 μM) and down-regulates *c-myc* oncogene expression.[44-46] Nevertheless, the interest in employing TmPyP4 is somewhat counterbalanced by its lack of selectivity and moderate to acute toxicity in normal cell lines.[47] TMPyP4 binds to duplex, triplex, G-quadruplex, single-stranded, and bulk genomic DNA with similar affinities ($K_d$ ~ 200 nM).[48, 49] The compound has significantly contributed to the understanding of the ligand-quadruplex interactions, but its use *in vivo* for probing the involvement of quadruplex in biological assays is questionable.

Phthalocyanines (Pcs) possess an attractive scaffold for the design of G-quadruplex probes because it provides a more extended aromatic system than the porphyrin skeleton. Pc-based G-quadruplex probes generally exhibit better structure selectivity than porphyrin ligands. Zinc tetrakis-(diisopropylguanidine) phthalocyanine (Zn-DIGP, Figure 1.11, C), which was developed in the Luedtke laboratory, was the first example of a high-affinity G-quadruplex ligand exhibiting both "turn-on" luminescence and the ability to knock-down RNA expression.[50] It exhibits a 5000-fold quadruplex *vs.* duplex selectivity as well as a very strong binding interaction with *c-myc* quadruplex DNA ($K_d \leq 2$ nM). In contrast to TmPyP4, Zn-DIGP is non-toxic *in vivo.* It exhibits good cellular uptake and is able to suppress luciferase expression which was attributed to G-quadruplex-mediated promoter inhibition.[50] This bodes well for the anticancer potential of guanidine-modified Pcs and related macrocycles.

Finally, telomestatin (Figure 1.11, D), a natural product isolated from *Streptomyces anulatus* 3533-SV4,[51] is a notable exception among the π-stacking ligands. In contrast to previously discussed G-quadruplex probes which contain positive charges, telomestatin is a neutral macrocycle. Nevertheless, it is one of the strongest and most specific telomerase inhibitors ($IC_{50}$ ~ 1 μM).[44-46] The ideal shape complementary between telomestatin and the G-tetrads results in good G-quadruplex affinity ($K_d$ ~ 30 nM) and good selectivity (70-fold lower affinity to duplex DNA).

*1.4.2 Groove/Loop Binding Ligands*

There are significant chemical and conformational differences between G-quadruplex and duplex grooves and therefore groove binding ligands can differentiate between quadruplex and duplex structures. Since groove dimensions vary with the structure of quadruplexes, groove binding could offer enhanced selectivity for a particular G-quadruplex topology. Martino *et al.* reported that the small molecule Distamycin A (Dist–A) (Figure 1.12, left) interacts with the quadruplex $[d(TGGGGT)]_4$ in a 4:1 binding mode, with two distamycin dimers binding simultaneously two opposite grooves of the quadruplex (Figure 1.12, right).[52] In this structure two Dist-A molecules, oriented in an anti-parallel, staggered fashion, adopt crescent shapes and establish four hydrogen bonds with guanines of the quadruplex (Figure 1.12, right). Dist-A displays high affinity toward both G-quadruplex and duplex DNA and lacks the selectivity necessary for a competitive quadruplex ligand.[53, 54] Nevertheless, Dist-A exemplifies that G-quadruplex recognition by groove-binding is both theoretically and practically possible and motivates further studies in this field. Recently, octahedral metal complexes with planar ligands have been designed for groove/loop binding.[40] Since the metal is protected by an octahedral ligand arrangement, it is unable to stack on G-tetrads and interacts with the grooves/loops and the phosphate backbone of G-quadruplexes.

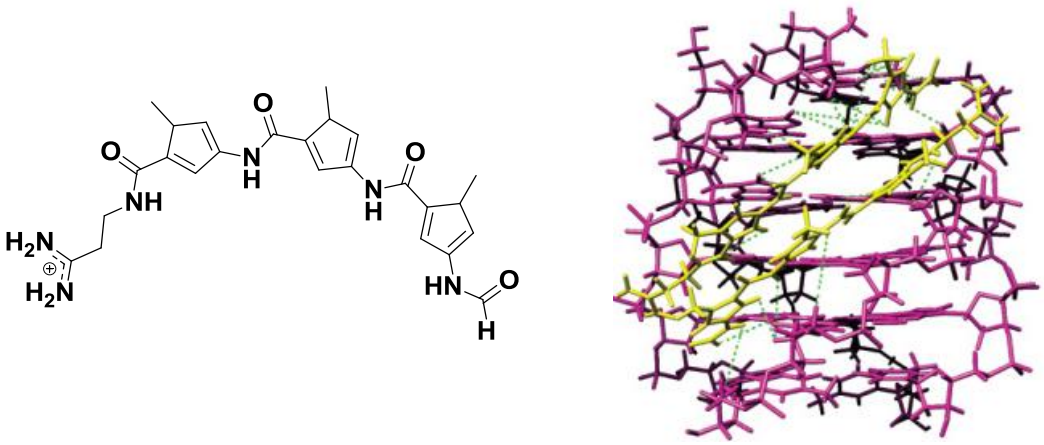


**Figure 1.12:** Left: Structure of Distamycin A; Right: Side view representation of the 4:1 complex Dist-A/$[d(TGGGGT)]_4$. Dist-A and $[d(TGGGGT)]_4$ are reported in yellow and magenta, respectively.[52]

*1.4.3 Central Channel Binding Ligands*

The design of G-quadruplex ligands, selectively interacting with the central channel, still needs to be largely investigated. Rodriguez *et al.* designed and synthesized N-(2-aminoethyl)-N'-(9-anthracenylmethyl)-1,2-ethanediamine capable of selectively inducing parallel quadruplex formation from unfolded DNA in the absence of monovalent cations (Figure 1.13, left).[55] While the anthracene moiety stacks onto an external G-quartet, the ammonium centers induce G-quadruplex folding through hydrogen bonding and cation-dipole interactions thus mimicking potassium ions within the central channels of quadruplexes (Figure 1.13, right).


**Figure 1.13:** Left: Structure of N-(2-aminoethyl)-N'-(9-anthracenylmethyl)-1,2-ethanediamine; Right: Proposed mode of how N-(2-aminoethyl)-N'-(9-anthracenylmethyl)-1,2-ethanediamine interacts with a G-quadruplex.[55]

### *1.5 Methods to Investigate G-Quadruplex/Ligand Interactions*

The evaluation of G-quadruplex affinity and specificity requires efficient and robust *in vitro* assays to effectively monitor and quantify G-quadruplex DNA/ligand interactions. Nowadays, a wide variety of biophysical and biochemical methods are available. Techniques like UV-Vis, fluorescence spectroscopy, and circular dichroism (CD) can be readily used to obtain information about ligand binding affinity and conformation of G-quadruplexes, whereas techniques like isothermal calorimetry (ITC) and surface-plasmon resonance (SPR) are useful for obtaining thermodynamic and kinetic parameters of these interactions.

X-ray, NMR, and dynamic simulation studies are used to obtain structural parameters involved in G-quadruplex/ligand interactions with atomic resolution.[19] There is no single technique available which provides a complete picture of the quadruplex/ligand interactions and usually it is necessary to use a combination of different methods. Nevertheless, UV-Vis, fluorescence, and CD spectroscopy are favored because of their rapidness, readily accessible technologies, small amounts of material they require, and their non-destructive character. These methods are usually used for melting measurements which provide information about the stabilization or destabilization of the quadruplex structure by the ligand under investigation.

### *1.6 Alternative Quadruplex Structures*

Previous experimental and theoretical studies focused on quadruplexes containing only GGGG-tetrads (G-tetrads). However, formation of mixed tetrads could dramatically increase the diversity of quadruplex structures by allowing nucleic acid sequences, lacking $G_n$-repeats, to adopt these four-stranded structures. Earlier NMR studies have shown that Watson-Crick G·C pairs can align through hydrogen-bonding to form GCGC-tetrads (Figure 1.14).[56-60] These studies demonstrated that GCGC-tetrads can switch between two distinct alignment geometries. In a "direct alignment" the two G·C pairs are aligned opposite to each other (Figure 1.14, left), whereas in the "slipped alignment " the major groove edges of two guanine bases are positioned opposite each other (Figure 1.14, right). In the latter case, a monovalent cation coordinates the central nitrogen and oxygen atoms of the guanine bases to stabilize the structure. While the direct GCGC-tetrad alignment is formed in $Na^+$-solution,[59] the slipped alignment is observed in $K^+$-solution.[60]

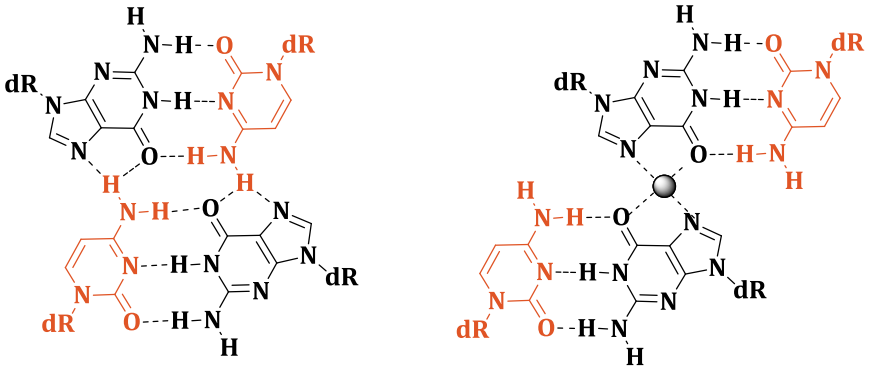

**Figure 1.14:** Potential GCGC-tetrad formation involving either direct (left) or slipped (right) alignment of major groove edges of two Watson-Crick GC pairs.

GCGC-tetrads have been observed in a wide range of DNA quadruplexes and recent studies have shown that GCGC-tetrad containing quadruplexes might be of biological relevance. Kettani *et al.* reported that the nucleic acid sequence d(GCGGT$_3$GCGG), containing the CGG fragile X triplet repeat, dimerizes in solution through head-to-tail alignment of hairpins. The resulting quadruplex contains a pair of central GCGC-tetrads flanked by GGGG-tetrads. In contrast, GGGC repeats in adeno-associated viral DNA can fold into a quadruplex containing central GGGG-tetrads flanked by GCGC-tetrads.[59] Nevertheless, the existence of GCGC-tetrads *in vivo* remains an open question.

### *1.7 Objectives*

Since their discovery DNA G-quadruplex structures have been the focus of extensive research. There is an increasing appreciation of the role these structures may play in biological processes ranging from replication, transcription, and recombination to telomere function.[61] In addition to the well studied GGGG-tetrads, GCGC-tetrads can participate in quadruplex formation *in vitro.* These structures may therefore also occur *in vivo* and have potential biological significance.

While there are a large number of GGGG-tetrad binding ligands available, selective GCGC-tetrad binding ligands have not yet been reported. This Master thesis is therefore focused on the design and synthesis of small molecules that can potentially recognize GCGC-tetrad-containing quadruplex structures with high affinity and specificity. The design strategies for highly selective GCGC-tetrad ligands are primarily based on planar, aromatic macrocyclic ring systems that exhibit high charge and shape complementary with the GCGC-tetrads constituting a quadruplex. This work can be summarized by three main goals:

1) Search for a synthetically accessible, macrocyclic scaffold that has extensive shape complementary with GCGC-tetrads. This scaffold should be compatible with the introduction of small modifications to generate small libraries of compounds.

2) Synthesis, purification, and single crystal growth of the selected scaffold and related derivatives to study their exact structural and electronic properties.

3) Investigation of the photophysical and reactivity properties of the selected scaffold to assess its potential as a GCGC-tetrad binder.

# *CHAPTER 2*

# *HEMIPORPHYRAZINES*

### *2.1 Macrocyclic Scaffolds for G-Quadruplex Recognition*

Porphyrin- and phthalocyanine-based macrocyclic scaffolds are particularly attractive for designing ligands with high affinity and specificity for quadruplex structures. On one hand, they often exhibit poor affinity for the standard B-form of DNA because their rigid structure and large size prevent them from intercalation into duplex DNA. On the other hand, their broad aromatic surface allows for maximal aromatic overlap between the ligand and an external G- or mixed-tetrad (Figure 2.1).

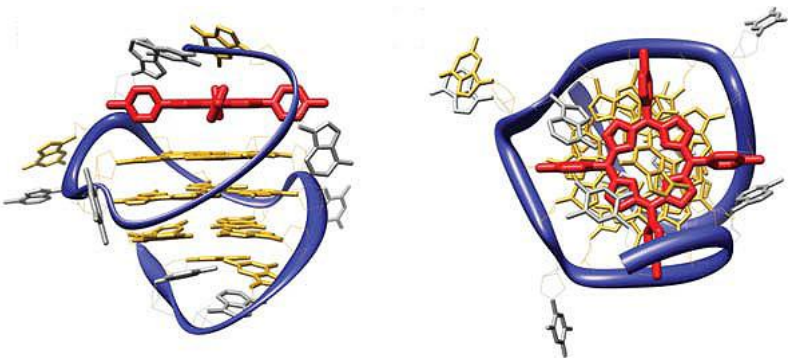

**Figure 2.1:** Side- (left) and top-views (right) of the NMR structure of TMPyP4 with quadruplex DNA.[36]

The ubiquitous role of natural porphyrins in vital processes like photosynthesis and cellular metabolism has motivated chemists to exploit this family of macrocycles in nucleic acid chemistry. The ability of a synthetic porphyrin derivative to interact with DNA was first reported in 1979 by Fiel *et al.* who showed that TMPyP4 (Figure 1.11, B) can bind to calf thymus DNA by intercalation as well as external electrostatic association.[62] Its use as a G-quadruplex ligand was reported for the first time in 1999 (Section 1.4.1).[63]

Since then, various porphyrin-like macrocycles, including corroles, porphyrazines, phthalocyanines, and sapphyrins, have been used in the development of selective G-quadruplex ligands.[64] Guanidine-modified phthalocyanines such as Zn-DIGP (Figure 1.11, C) exhibit some of the most exceptional properties in terms of G-quadruplex affinity and G-quadruplex *vs.* duplex DNA selectivity (Section 1.4.1). As a consequence, our GCGC-tetrad ligand design has been focused on a Pc-related macrocyclic scaffold.

Among others, Zn-DIGP revealed the importance of charge and shape complementary between the ligand and the GGGG-quartets for high affinity and specificity interactions. Since GCGC-quartets exhibit $C_2$-symmetry, the $C_4$-symmetric Pcs were not considered ideal compounds for targeting these structures. In contrast, a planar, $C_2$-symmetric macrocycle with extended π-conjugation was identified as a suitable framework. Hemiporphyrazines (Hps), formally derived from Pcs by the replacement of two opposite isoindole moieties by two pyridine rings, thereby became the targeted scaffold (Figure 2.2, right).

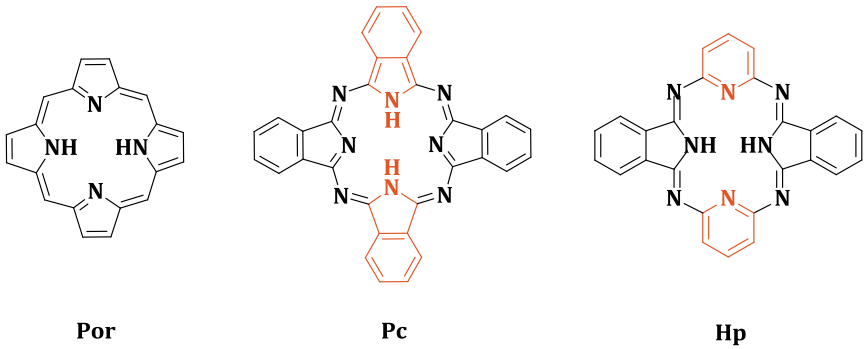


**Figure 2.2:** Left: Structure of porphyrin (Por); Middle: Structure of phthalocyanine (Pc); Right: Structure of hemiporphyrazine (Hp).

## *2.2 Current Knowledge on Hemiporphyrazines*

### *2.2.1 Physical and Chemical Properties*

First synthesized by Elvidge and Linstead in 1952,[65] hemiporphyrazines (Hps) are $C_{2v}$-symmetric, planar macrocycles with two co-facial pyridine rings and two co-facial isoindole units linked through four aza bridges (Figure 2.2, right and Figure 2.3). Known features of these compounds include high thermal stability and oxygen insensitivity.[66] The inner cavity of Hps is well-suited for the coordination of a large number of transition metals. Hp complexes containing Co, Ni, Cu, Zn, Fe, Mn, Pd, Pb, $GeCl_2$, VO, InCl, and Li have been reported.[67-75]

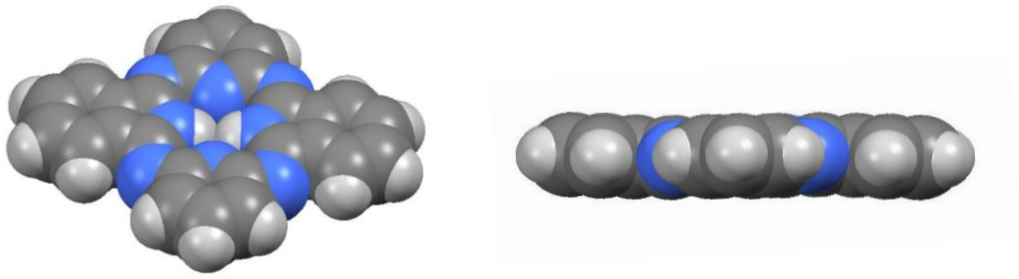

**Figure 2.3:** Graphical representation of space-filling models of hemiporphyrazine free base ($HpH_2$).

Hps are non-aromatic compounds with a cross-conjugated 20 π-electron system. As a consequence, they display different chemical and physical properties compared to the highly aromatic Pcs. Hps exhibit enhanced chemical reactivity and rapidly hydrolyze in the presence of aqueous acid.[65] In contrast to metallo Pcs (MPcs), metallo Hps (MHps) exhibit a very strong tendency toward octahedral ligand coordination even with metals of $d^8$-$d^{10}$ configuration like zinc, nickel, or copper that normally exhibit square planar or tetrahedral coordination complexes. The 1:1 or 1:2 adducts with $H_2O$, hydrogen halides, or solvent molecules are directly obtained from the macrocyclization reaction.[68] This is a result of the low degree of π-electron delocalization across the macrocycle and the high asymmetry of the Hp ligand core. Early NMR and IR studies on germanium and tin Hps confirmed that the isoindole nitrogen atoms bind to the metal much stronger than the nitrogen atoms from the pyridine rings which retain much of their original character.[72, 76]

Unsubstituted Hps and MHps show very low solubility in organic solvents. In the solid state, they are involved in strong π–π stacking interactions with an interplanar distance of 3.36 Å which is very similar to those of graphite (3.35 Å) and Pc (3.38 Å).[77] Good solubility can be obtained with appropriate peripheral substitution like the introduction of lipophilic chains on the isoindole moiety and/or the pyridine ring (Figure 2.4). The corresponding alkyl- or alkoxy-substituted nickel Hps are accessible by heating the corresponding pre-substituted diiminoisoindolines, diaminopyridines, and nickel acetate in butanol (Figure 2.4).[70] The resulting substituted Hps are typically obtained as a 1:1 mixture of constitutional isomers, exhibiting either $C_{2v}$- or $C_{2h}$-symmetry depending on the relative orientation of the peripheral substituents. [66]

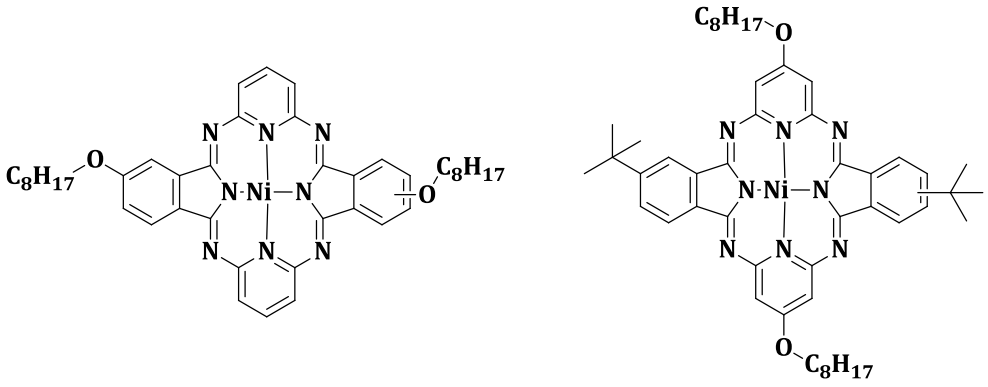


**Figure 2.4:** Representative structures of peripheral substituted Hps with good solubility.

NiHp was the first Hp crystal structure reported.[78] In contrast to the corresponding planar NiPc, NiHp exhibits a saddle-shaped, non-planar conformation. This has been ascribed to a core contraction that is necessary to effectively coordinate the low-spin Ni(II) ion.[79] In contrast, the metallated high-spin Hp monohydrate complexes, MHp·$H_2O$ (M = Mn(II), Co(II), Cu(II), Zn(II)) are reported to possess a planar geometry in analogy to the structure of the anhydrous free base ligand $HpH_2$ (Figure 2.3).[77] This shows that hemiporphyrazines are conformational very flexible molecules that likely exhibit rapid dynamic equilibria between planar and saddle-shaped conformations in solution.

Hps are conformational more flexible and electronically less rigid than Pcs. Metallated Pcs generally carry a dianionic charge on the ligand, while MHp complexes with dianionic, monoanionic, and neutral ligands have been reported.[65, 68, 74] Hps also exhibit a great synthetic versatility and can be obtained as ladder-type polymers in which the monomeric units are arranged in a planar way along the polymer chain (Figure 2.5) or as axially bridged stacked systems to which one refers to as co-facially assembled polymers (Figure 2.7).[66, 80-82]

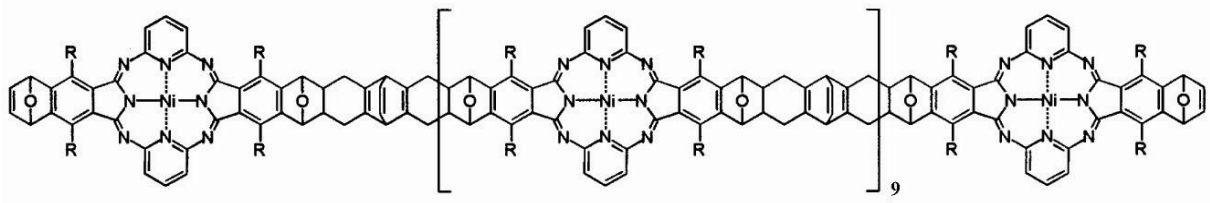

**Figure 2.5:** Schematic representation of Hp-based ladder-type polymer.[66]

Ladder-type polymers can be obtained by repetitive Diels-Alder reactions of enophilic (Figure 2.6, left) and dienophilic Hps (Figure 2.6, right). The nonamer was the highest oligomer prepared according to this strategy.[66] In contrast, ladder-type polymers that contain phthalocyanines as stabilizing units are more difficult to obtain because an asymmetrically substituted phthalocyanine is required for their preparation.

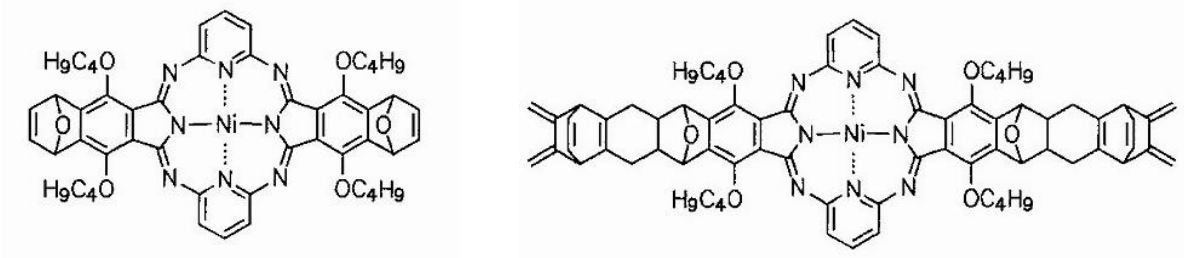

**Figure 2.6**: Representative structures of enophilic (left) and dienophilic (right) MHps.[80]

*2.2.2 Applications*

Hps have received relatively little interest as units for molecular organic materials due mainly to their low chemical stability in aqueous acidic solution and limited solubility properties. Works in this field have mainly focused in three directions, namely electrical conductivity, non-linear optical (NLO) properties, and catalysis.

Marks *et al.* reported the synthesis and electrical conductivities of co-facially linked MHp polymers $[M(Hp)O]_n$, where M = Si and Ge (Figure 2.7). The resulting polymers are structurally well defined with average degrees of polymerization of ≈ 25 (M = Si) as well as 60 (M = Ge) units. They exhibit both high air and thermal stability.[83] The stacked Ge and Si polymers turned out to be insulating materials ($10^{-11}$ – $10^{-12}$ $\Omega^{-1}$ $cm^{-1}$) and doping with iodine did not improve their conductivity. This was attributed to the partial destruction of the polymer M-O-M framework upon iodination.[83] Theoretical calculations performed by Honeybourne suggested that undoped, co-facially assembled Hps exhibit low σ values at room temperature as a result of large band gaps.[84]

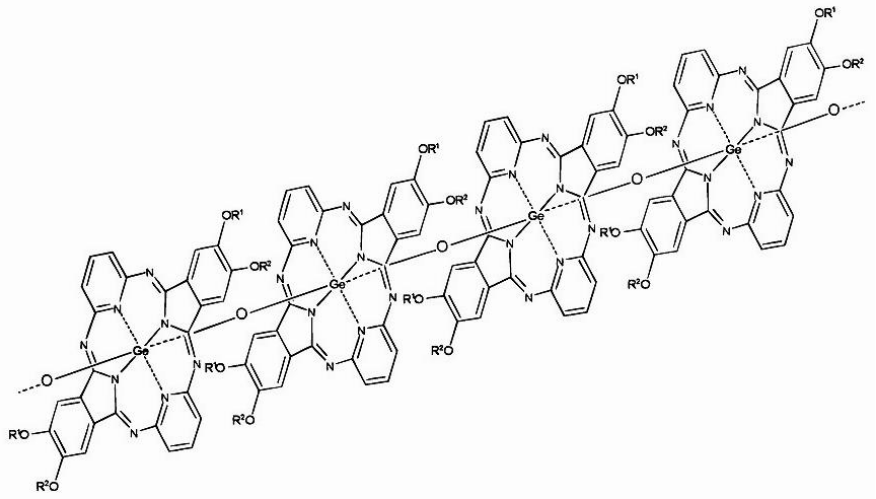


**Figure 2.7**: Schematic representation of co-facially assembled [Ge(Hp)O]-polymer.[66]

Early electrical conductivity studies were focused on Hp thin films. In analogy to Hp polymers, they had an insulating character with σ values between $10^{-7}$ and $10^{-17}$ $\Omega^{-1}$ $cm^{-1}$ at 100°C. These investigations also suggested that Hp thin films are inert to $N_2$, $O_2$, CO, $CH_4$, $SO_2$, $CO_2$, $H_2$, $NH_3$, $H_2S$, $N_2O$, $NO_2/N_2O_4$, NO, $Cl_2$, and HCl. No variation of the conductivity was observed upon exposure to these gases.[85, 86] As a consequence, additional synthetic effort is needed for the development of Hp-based materials with interesting electrical and magnetic properties.

Due to their semi-delocalized, π-conjugated systems Hps are potentially useful as nonlinear optical materials. Dini *et al.* reported the multiphoton absorption properties of five Hps with different central atoms ($H_2$, $GeCl_2$, InCl, Pt, Pb) and the dynamics of their excited states under irradiation using nano second laser pulses at 532 nm.[74] The metal-free and platinum Hps (Figure 2.8) displayed saturation of optical transmittance within incident fluence values of 6 $J \cdot cm^{-2}$ which suggests that Hps are strong non-linear absorbers and an interesting class of molecules for photonic applications.

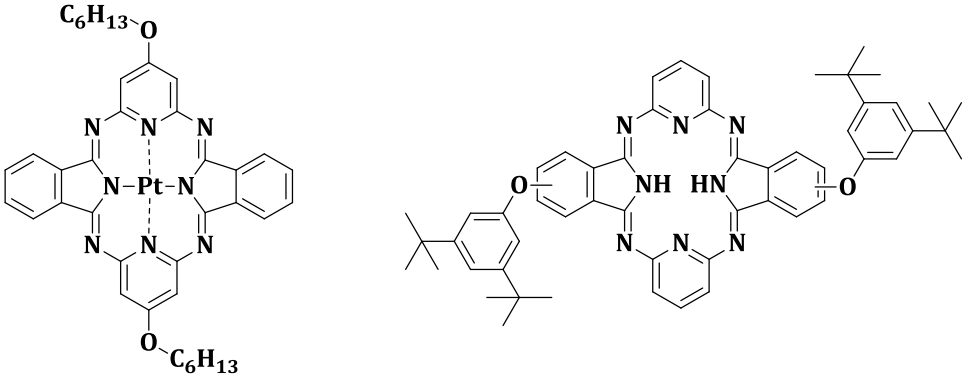


**Figure 2.8**: Left: Structure of $(HexO)_2HpPt$; Right: Structure of $(t Bu_2PhO)_2HpH_2$.[74]

The catalytic activity of Hps has been evaluated for several manganese Hps in the oxidation of cyclooctene to cyclooctene epoxide by potassium monopersulfate (Figure 2.9).[87] In the absence of a nitrogenous base, the Hp compound did not exhibit any catalytic activity. However, upon addition of pyridine to the reaction mixture, significantly enhanced oxygenation rates were observed. This suggests that the presence of an axial ligand in the coordination sphere of the MHp may be important for promoting its catalytic activity.[87] Campaci *et al.* reported that pyridine coordination to manganese makes the metal prone to oxidation by monopersulfate and promotes the formation of an oxo-MnHp intermediate which oxidizes the olefin more efficiently than monopersulfate itself.[87] On the basis of these preliminary results, a catalyst based on Hps exhibiting both high activity and reaction yields appears feasible.

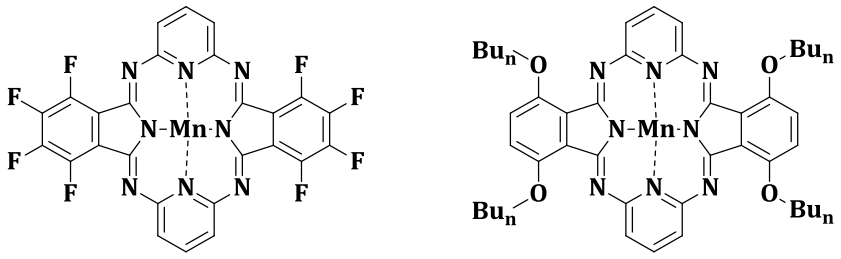

**Figure 2.9**: Structures of MnHps used to explore the catalytic activity of Hps in oxygenation reactions.[87]

In conclusion, Hps have not yet found broad use as functional materials. This is, in part, due to the lack of experimental studies on Hps. A better understanding of the physical and chemical properties of Hps will be required for the future design and realization of Hp-based conductors, non-linear optical devices, and catalysts.

### *2.3 Hemiporphyrazines as GCGC-Tetrad Probes*

Hps are interesting targets for the design of π-π stacking GCGC-tetrad ligands because they can present a large, planar surface with similar molecular dimensions as GCGC-tetrads (Figure 2.10). Apart from the shape complementary, the Hp scaffold exhibits additional features which potentially help to increase its affinity and selectivity towards GCGC-tetrads. Its $C_2$-symmetry matches the symmetry of a GCGC-tetrad and makes asymmetrically substituted Hps easy accessible. Macrocycles with different peripheral substituents could be used to fine-tune the interactions between the ligand and the grooves of quadruplex structures.

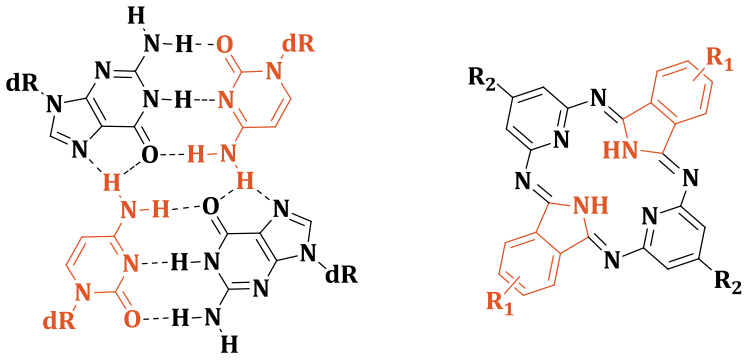


**Figure 2.10**: $C_2$-symmetric structures of GCGC-tetrad (left) and $HpH_2$ (right).

Porphyrin- and phthalocyanine-based quadruplex ligands are conformational rigid compounds that ideally stack on top of planar structures. However, since quadruplexes have highly dynamic and flexible topologies, they are not constantly locked in a planar conformation and are subject to conformational distortions. As a consequence, it is of potential importance that fluorescent probes also exhibit conformational flexibility to adapt to the quadruplex structure. Hemiporphyrazines are ideal targets for conformational flexible quadruplex probes, being able to adopt both planar and saddle-shaped conformations.

In theory, Hps have good requirements for GCGC-tetrad recognition. Nevertheless, a good understanding of the chemical and physical properties of the Hp skeleton is required for evaluating the potential of Hps as selective GCGC-tetrad ligands. This Master thesis focuses on the investigation of the synthesis and structure of the Hp macrocycle and some of its metal derivatives. One of the key goals is to obtain a soluble Hp analogue that allows for photophysical characterization and reactivity studies of the Hp skeleton in solution. These results will be required for future investigations that will be aimed at the synthesis of a water soluble Hp that can be used for GCGC-tetrad binding assays.

# *CHAPTER 3*

# *SYNTHESIS AND STRUCTURE OF HEMIPORPHYRAZINES*

### *3.1 Reaction Mechanism*

One straight forward method for the synthesis of hemiporphyrazines involves heating of two starting materials in a 1:1 ratio in the presence of a high boiling solvent like 1-chloronaphthalene or nitrobenzene.[65, 67, 68] Phthalonitrile and 2,6-diaminopyridine derivatives are the most commonly used starting materials. 1,3-diiminoisoindoline precursors can be used instead of phthalonitrile, but the reactions generally proceed in lower yields.

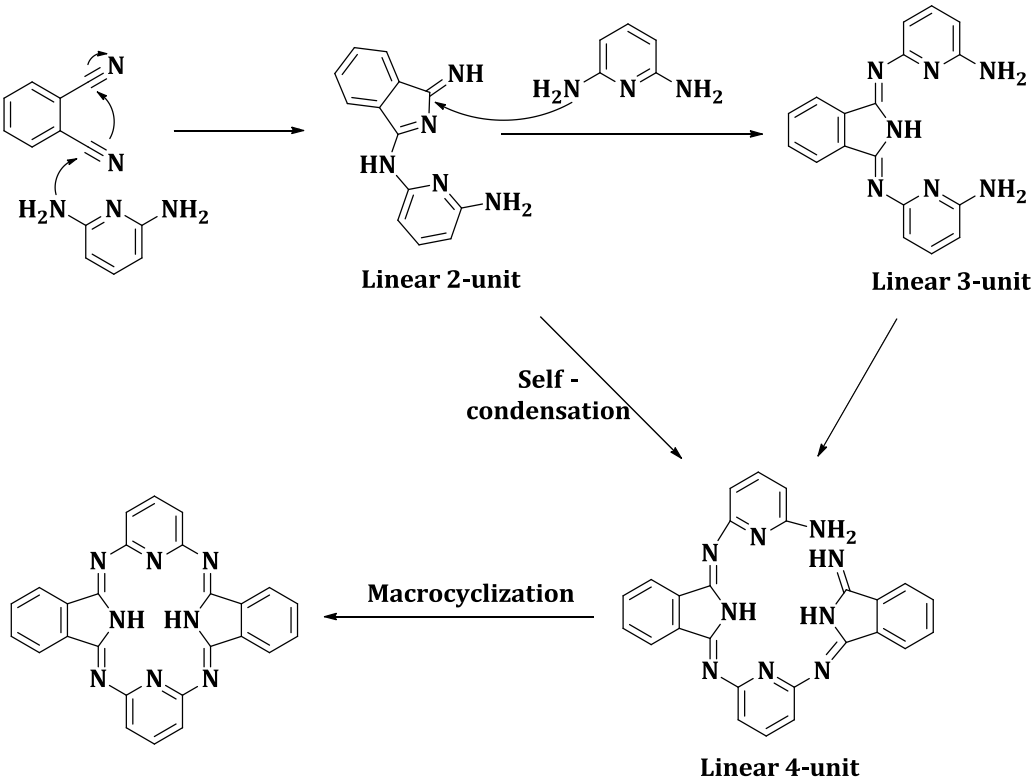


**Figure 3.1**: Abbreviated reaction mechanism of hemiporphyrazine formation.

Metallo hemiporphyrazines (MHps) can be obtained either directly from the macrocyclization reaction when conducted in the presence of a metal ion source or after macrocycle formation by heating metal-free Hp in the presence of a metal ion. In general, the direct synthetic route is preferred because it exhibits an enhanced reaction rate and results in higher yields. The metal ion can serve as a template during the macrocycle assembly and thereby reduces the formation of polymeric byproducts.

While the mechanism of Pc formation has been extensively studied,[88] there are no mechanistic investigations on Hp formation. However, due to the Hps' structural resemblance to Pcs it is likely that both macrocycles are assembled according to the same mechanistic principles. These steps are characterized by successive oligomerization of the starting materials followed by ring closure to the macrocycle (Figure 3.1). [65] Thereby, two mechanistic routes are reasonable in which the key intermediate (linear 4-unit) is formed by either self-condensation of two dimers (linear 2-unit) or by stepwise oligomerization of monomers via a trimer (linear 3-unit) (Figure 3.1).[65]

The formation of linear polycondensation byproducts containing more than four units was proposed to be a result of reaction intermediates with unfavorable *anti*-conformations around one or more of the carbon-nitrogen bonds (Figure 3.2, middle).[65] The presence of bivalent metal ions can diminish the formation of byproducts by forcing the carbon-nitrogen bonds to adopt a *syn*-conformation by simultaneously coordinating the isoindole and pyridine nitrogen atoms (Figure 3.2, right).

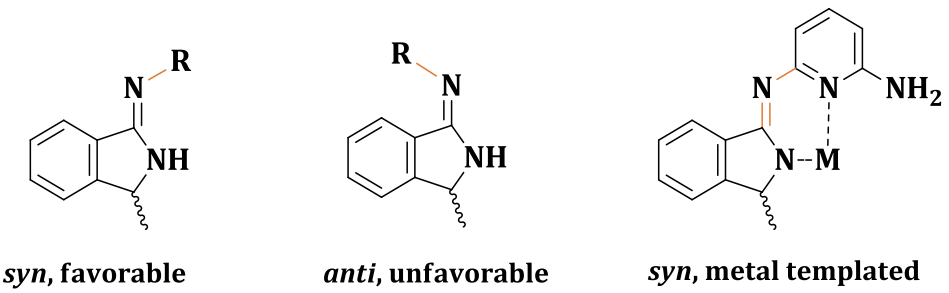


**Figure 3.2**: Possible conformations around the carbon-nitrogen bond during macrocyclization.

### *3.2 Synthesis and Structure of Free Base Hemiporphyrazine*

Free-base hemiporphyrazine ($HpH_2$) (**1**) was prepared by heating equal amounts of phthalonitrile and 2,6-diaminopyridine in the presence of 1-chloronaphthalene. Compound **1** was thereby obtained as red needles after recrystallization from nitrobenzene in 60 % yield (Scheme 3.1). Shorter reaction times (< 19 h) as well as lower temperatures (< 180 °C) resulted in an open chain product containing one isoindole and two pyridine units. This indicates that macrocyclization occurs by a stepwise mechanism with a three-unit species as a key intermediate rather than a two-unit precursor undergoing self-condensation (Figure 3.1).

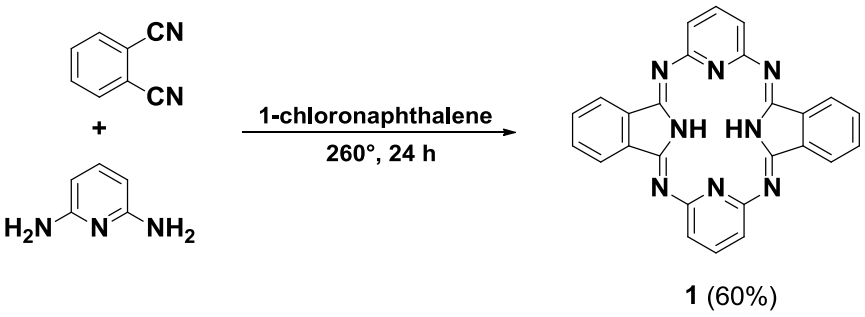


**Scheme 3.1**: Synthesis of $HpH_2$ (**1**).

In 1986, a relatively low quality X-ray structure of **1** was reported (R = 0.115).[77] The structure was refined without hydrogen atoms and was insufficient for reliable bond length analysis. Crystals suitable for a high quality X-ray diffraction structure determination were therefore grown by slow cooling of a saturated methyl-naphthalene solution from 180 °C – 25 °C over two days under inert atmosphere. The resulting structure at 160 K (R = 0.049) was found to have different unit cell parameters than the previously published structure (Figure 3.3).

Aside from small distortions, $HpH_2$ (**1**) adopts a nearly planar structure. The four inner nitrogens form an elliptical core of around 13.7 $Å^2$. The nitrogen atoms of the isoindole moieties are separated by 3.867(2) Å, whereas the distance between the two pyridyl nitrogen atoms is 4.506(2) Å. Despite the presence of repulsive interactions between the isoindole hydrogen atoms (N-H•••H-N distance = 2.12(3) Å) in the center of the macrocycle, both hydrogens of $HpH_2$ (**1**) are nearly co-planar in the crystal structure (Figure 3.3).

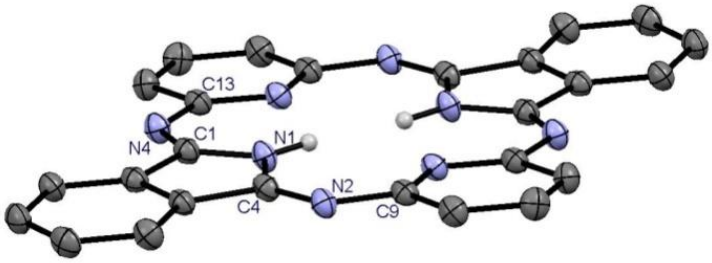


**Figure 3.3**: Crystal structure of $HpH_2$ (**1**). 50% displacement ellipsoids are shown and selected hydrogen atoms have been omitted for clarity.

The skeleton of **1** is build of alternating double and single bonds, consistent with the non-aromatic character of Hps. Thereby, the C4-N2 bond length measures at 1.276 Å which is in the range of carbon-nitrogen double bonds and the C9-N2 distance is 1.394 Å which is consistent with a carbon-nitrogen single bond.

$HpH_2$ (**1**) is a sparingly soluble compound and is only partially soluble in DMSO and DMF at room temperature. Good solubility in these solvents is only observed at temperatures above 180 °C. The poor solubility of **1** is possibly a result of the extensive stacking interactions between individual Hp molecules observed in the crystal packing of $HpH_2$ (Figure 3.4 and Section 2.2.1).

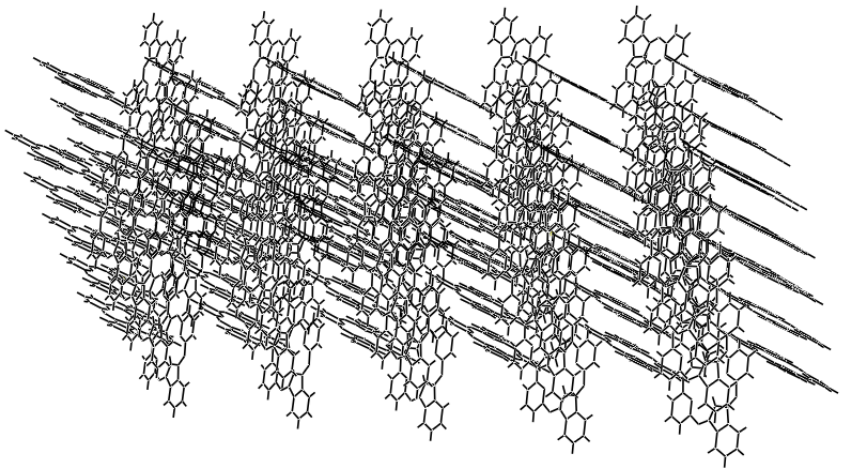

**Figure 3.4:** Packing diagram of $HpH_2$ (**1**).

### *3.3 Structure of Free Base Hemiporphyrazine Monohydrate*

Free-base hemiporphyrazine ($HpH_2$) (**1**) has a very high water affinity. It readily absorbs water from the atmosphere to form a yellow monohydrate ($HpH_2 \cdot H_2O$) (**2**) which can be converted back into the red anhydrous ligand by heating the macrocycle at temperatures above 150 °C in dry benzyl alcohol or nitrobenzene.[65]

Good crystallographic analysis for $HpH_2 \cdot H_2O$ (**2**) has already been reported (R = 0.068).[79] In contrast to **1**, **2** is characterized by a non-planar, saddle-shaped conformation (Figure 3.5). The N2-C9 bond length of **2** (1.411(4) Å) is slightly longer than the corresponding N2-C9 bond of **1** which has a length of 1.394(2) Å (Figure 3.3). This suggests a smaller extent of π-conjugation across the pyridine units in $HpH_2 \cdot H_2O$ (**2**) as compared to $HpH_2$ (**1**). The nitrogen atoms of the isoindole moieties are separated by 4.041 Å, while the distance between the two pyridyl nitrogen atoms measures 4.441 Å (Figure 3.5). Consequently, the elliptical core of **2** (14.09 $Å^2$) is slightly larger than the one of **1** (13.7 $Å^2$).

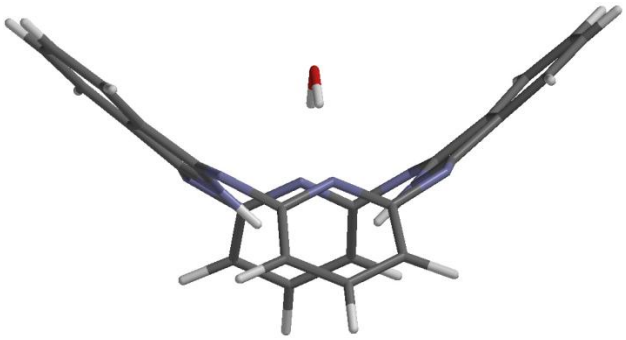

**Figure 3.5**: Published crystal structure of $HpH_2 \cdot H_2O$ (**2**).[79] Atoms are labeled in analogy to $HpH_2$ (**1**).

The water molecule of crystalline $HpH_2 \cdot H_2O$ (**2**) is located between two neighboring macrocycles with its two hydrogen atoms hydrogen-bonded to two pyridine nitrogen atoms of the lower Hp molecule and its oxygen lone pairs involved in hydrogen bonding with the two isoindole protons of the upper Hp molecule. This hydrogen bonding pattern in **2** causes a column-like packing of the molecules (Figure 3.6).

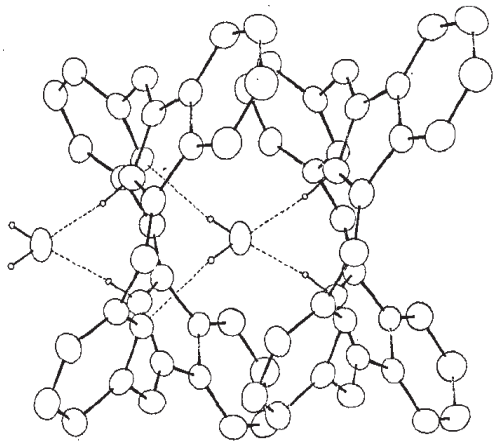

**Figure 3.6**: Column-like packing of $HpH_2 \cdot H_2O$ (**2**) mediated by $H_2O$ hydrogen bonding.[79]

The presence of hydrogen bonds is also confirmed by IR analysis which reveals very broad O-H stretching frequencies at 3400 $cm^{-1}$ and N-H stretching frequencies at 3230 $cm^{-1}$ for the hydrated ligand. In contrast, $HpH_2$ (**1**) lacks the O-H stretching frequency completely and the N-H stretching is sharp (Figure 3.7).

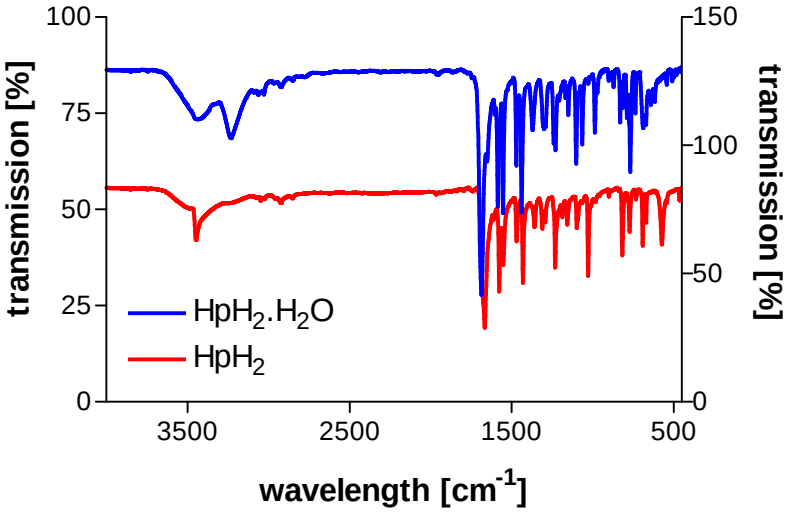


**Figure 3.7**: IR spectra of $HpH_2 \cdot H_2O$ (**2**) and $HpH_2$ (**1**).

### *3.4 Metallo Hemiporphyrazines*

*3.4.1 Zinc Hemiporphyrazine*

MHps are generally obtained from the reaction of $HpH_2$ (**1**) with the appropriate metal acetate or halide.[65] The resulting compounds are sparingly soluble in organic solvents and therefore difficult to fully characterize in solution. It was hypothesized that the solubility of unsubstituted MHps can be controlled by the choice of the counter ions which occupy the axial positions of the central metal ion. Bulky counter ions should be able to prevent stacking interactions between the planar macrocycles and improve the solubility of unsubstituted Hps. Metal-triflates were identified as suitable metal ion sources for this purpose. Thereby, reactions containing a 2 : 2 : 1 mixture of 2,6-diaminopyridine, phthalonitrile, and $Zn(OTf)_2$ in refluxing nitrobenzene give a red crystalline substance $HpH_2Zn(OTf)_2$ (**3**) in 69 % isolated yield (Scheme 3.2). This new zinc Hp complex is soluble in MeOH, DMSO, and DMF and can be handled in the presence of oxygen and traces of water without decomposition. Crystals of **3** suitable for crystallographic characterization were grown in concentrated methanol solutions by slow diffusion of diethyl ether. Two types of crystals were obtained. The first was a relatively low quality crystal type which gave a crystal structure consistent with elemental analysis and NMR data of $HpH_2Zn(OTf)_2$ (**3**). While reliable bond lengths cannot be ascertained from this X-ray data, the molecular framework of the model is dependable. In this structure, the Hp ligand is essentially planar and the axial coordination sites of octahedral zinc are occupied by triflate ions (Figure 3.8).

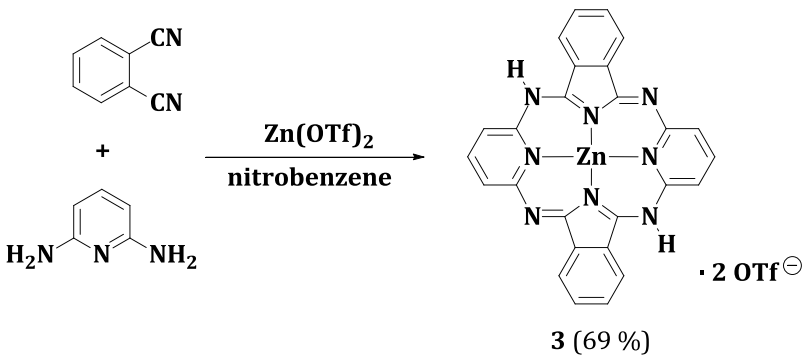


**3** (69 %)

**Scheme 3.2**: Synthesis of $HpH_2Zn(OTf)_2$ (**3**).

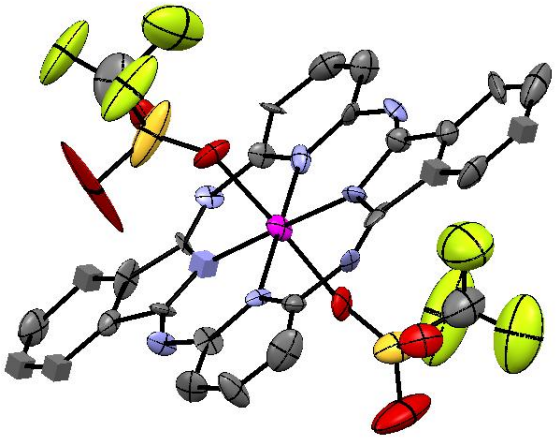

**Figure 3.8**: Preliminary X-ray structure of $HpH_2Zn(OTf)_2$ (**3**). Selected hydrogen atoms have been omitted for clarity.

The second crystal type gave very high quality diffraction data and was found to be the methanolysis product of $HpH_2Zn(OTf)_2$ (**3**) where methanol had displaced the axial triflate ions from zinc. The resulting structure of "$HpH_2Zn(MeOH)_2{\cdot}2(OTf)$" is $C_{2h}$-symmetric, where the two exchangeable N-H protons on the ligand are at diagonal *meso* nitrogen atoms (Figure 3.9). The triflate counterions (omitted for clarity in Figure 3.9) act as acceptors of O-H•••O hydrogen bonds from methanol (H•••O = 1.95(3) Å) and N-H•••O hydrogen bonds from the *meso* nitrogen atoms (H•••O = 2.13(2) Å).

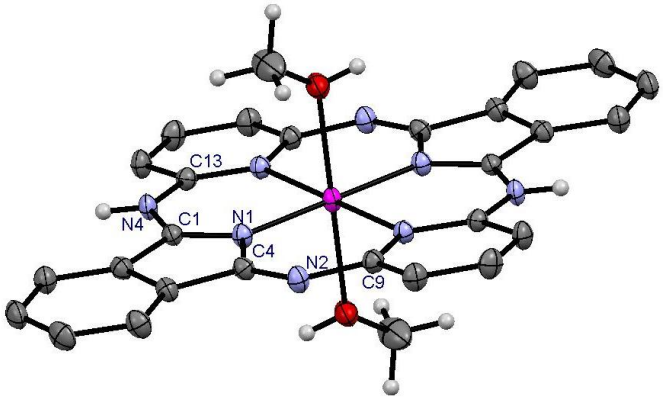


**Figure 3.9:** Crystal structure of $HpH_2Zn(MeOH)_2{\cdot}2(OTf)$ containing two equivalents of MeOH. The triflate counterions and selected hydrogen atoms have been omitted for clarity. 50% displacement ellipsoids are shown.

In previous MHps the Hp ligand carried a -2 or -1 charge in complexes containing Pb(II), Co(II), Cu(II), Ge(IV), Li(I), Ni(II), Fe(II), Mn(II), Sn(IV), or Cr(II).[65, 68, 72, 75, 89, 90] There are only a small number of "neutral ligand" metallo hemiporphyrazines of the type $HpH_2MX_2$ reported, where M = Cu(II), Ni(II), or Zn(II), and X = Cl or Br.[68] In these complexes, the charge of the metal ion is balanced by the axial ligands to give a neutral Hp ligand. $HpH_2Zn(MeOH)_2{\cdot}2(OTf)$ represents the first example of a neutral, metallated Hp ligand crystal structure. One might consider a zwitterionic representation for the Hp ligand in this complex (Figure 3.10, left), but bond length analyses indicate that the neutral representation (Figure 3.10, right) is more informative, where the N1-C1 and N1-C4 bond lengths are highly asymmetric, at 1.328(2) Å and 1.409(2) Å, respectively. Likewise, C1-N4 and C4-N2 are also asymmetric, at 1.331(2) Å and 1.274(2) Å, respectively (Figure 3.9). These bond lengths reveal the presence of an alternating pattern of single and double bonds consistent with a greater contribution from the neutral resonance structure (Figure 3.10, right).

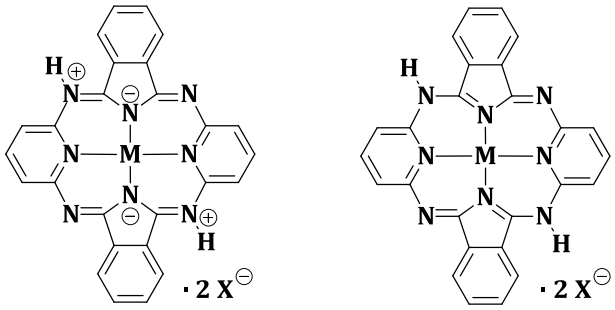

**Figure 3.10**: Schematic representation of zwitterionic (left) and neutral (right) resonance structures of $HpH_2Zn(OTf)_2$ (**3**).

The number of publications on neutral-ligand MHp complexes is limited due to the fact that $HpH_2$ (**1**) is usually deprotonated upon metal insertion to give a dianionic ligand (Figure 3.11). The dianionic form of the ligand is thermodynamically more stable than the neutral Hp ligand. Increased reaction times (> 4 h) under otherwise identical reaction conditions resulted exclusively in the formation of the known dianionic zinc hemiporphyrazine complex.[68] This was accompanied by a loss of solubility in methanol and a color change from red to green.

In addition, the dianionic Hp ligand was obtained directly by the use of solvents and metal ion sources such as $ZnCl_2$ and 1-chloronaphthalene. Consequently, the formation of $HpH_2Zn(OTf)_2$ (**3**) is dependent on the exact metal ion source, reaction solvent, and reaction time.

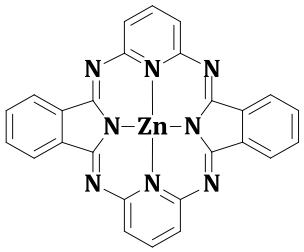


**Figure 3.11**: Schematic representation of zinc hemiporphyrazine containing a dianionic Hp ligand.

*3.4.2 Nickel Hemiporphyrazine*

To evaluate whether the same synthetic strategy developed for $HpH_2Zn(OTf)_2$ (**3**) can be applied for the synthesis of other soluble MHps having the basic formula $HpH_2M(OTf)_2$, phthalonitrile and 2,6-diaminopyridine were heated in the presence of $Ni(OTf)_2$. Thereby, $HpH_2Ni(OTf)_2$ (**4**) was obtained as red crystals in 72 % isolated yield. In analogy to **3**, **4** is highly soluble in MeOH, DMSO, and DMF.

Crystals of **4** suitable for X-ray diffraction were obtained from concentrated methanol solutions by slow diffusion of diethyl ether. The resulting structure of $HpH_2Ni(MeOH)_2{\cdot}2OTf$ (Figure 3.12) is isostructural with $HpH_2Zn(MeOH)_2{\cdot}2OTf$ (Figure 3.9). The Hp ligand is again neutral and exhibits a planar conformation. The axial coordination sites of nickel are occupied by methanol molecules. This suggests that the triflate counterions are only weakly bound to the central metal ion and are readily exchanged by solvent molecules. $HpH_2Zn(MeOH)_2{\cdot}2OTf$ shows small distortions from a perfect octahedral geometry, but $HpH_2Ni(MeOH)_2{\cdot}2OTf$ is completely symmetrical. While the Ni1-O1 and Ni1-O1’ distances measure at 2.115 Å, the Ni1-N3 as well Ni1-N3’ bond lengths are 2.189 Å and the nickel and isoindole nitrogen atoms (Ni1-N1 and Ni1-N1’) are separated by 1.976 Å (Figure 3.12).

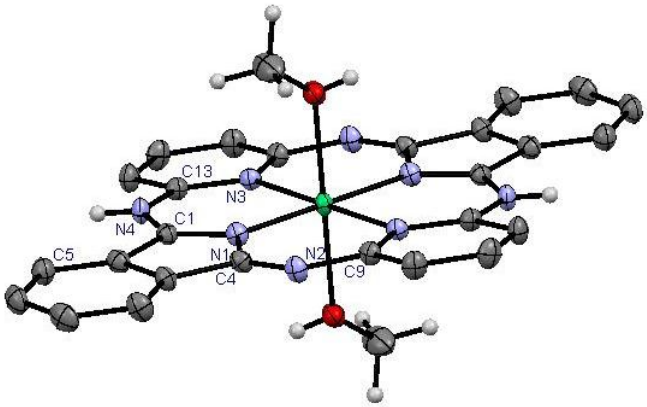


**Figure 3.12**: Crystal structure of $HpH_2Ni(MeOH)_2 \cdot 2(OTf)$ containing two equivalents of MeOH. The triflate counterions and selected hydrogen atoms have been omitted for clarity. 50% displacement ellipsoids are shown.

In contrast, the bond lengths between zinc and the axially coordinated methanol molecules are asymmetrical. The Zn1-O1 distance measures 2.246 Å while the Zn1-O2 bond length is 2.308 Å (Figure 3.9). Similar trends are also observed for the Zn-(pyridine-nitrogen) and Zn-(isoindole-nitrogen) bonds (Section 3.4.1).

The fact that the MeOH molecules exhibit an increased distance to the central metal ion in $HpH_2Zn(MeOH)_2 \cdot 2OTf$ than $HpH_2Ni(MeOH)_2 \cdot 2OTf$ can be explained by the crystal field theory. This model states that the more electrons occupy the d-orbitals that are directed toward the ligand the longer the M-L distances are due to electrostatic repulsion. Assuming an octahedral geometry for both $HpH_2Ni(MeOH)_2 \cdot 2OTf$ and $HpH_2Zn(MeOH)_2 \cdot 2OTf$, the $d_z^2$-orbital is directed toward the oxygen atom of the methanol molecule. Consequently, the M-O distance will depend on the number of electrons in the $d_z^2$-orbital. The Ni(II) ion has a singly occupied $d_z^2$-orbital. The Zn(II) ion on the other hand has two electrons in its $d_z^2$-orbital and therefore shows an enhanced electrostatic repulsion towards the axially coordinated methanol molecule and therefore increased Zn-O bond lengths.

In summary, soluble MHp complexes can be obtained from macrocyclization reaction when conducted in the presence of metal triflates and nitrobenzene. The Hp ligand is largely unaffected by the introduction of metal triflates and the resulting compounds can be used as soluble Hp analogues for evaluating the photophysical and reactivity properties of planar hemiporphyrazines in solution.

# *CHAPTER 4*

# *PHOTOPHYSICAL PROPERTIES OF HEMIPORPHYRAZINES*

Hemiporphyrazines were discovered more than half a century ago,[65] but their photophysical properties remain enigmatic. Previous photophysical studies on Hps have almost exclusively focused on theoretical computation rather than on experimental investigation.[91-95] This is due, in part, to the very poor solubility of the metal-free macrocycle in organic solvents at room temperature and its high affinity towards water molecules. The resulting hydrated Hps have non-planar conformations with distinct photophysical properties.[68, 79, 92] Together with their tendency to form aggregates and possibility of excited-state tautomerization, metal-free Hps like $HpH_2$ (**1**) are very difficult to fully characterize in solution. This explains why experimental investigations on the photophysical properties of Hps have remained scarce.

The evaluation of the Hps' affinity and specificity towards GCGC-tetrads will involve UV/Vis- and fluorescence-based *in vitro* assays (Section 1.5). In order to correctly interpret these results a full understanding of the Hp photophysics in solution is essential. As a consequence, this chapter reinvestigates the photophysical properties of Hps.

## *4.1 Tautomeric Forms of Hemiporphyrazine*

Due to the non-equivalence of the four inner nitrogens of $HpH_2$ (**1**), three tautomeric forms can formally be drawn for the metal-free macrocycle (Figure 4.1, A-C). The tautomer with two central hydrogens linked to the isoindole rings (Figure 4.1, A) is considered to be the only relevant structure in the ground state because it exhibits $2^4$ resonance structures.[91, 93-95] The other two tautomers have only $2^2$ (Figure 4.1, B) and $2^3$ (Figure 4.1, C) resonance structures, respectively and are assumed to form only transiently in the excited state.

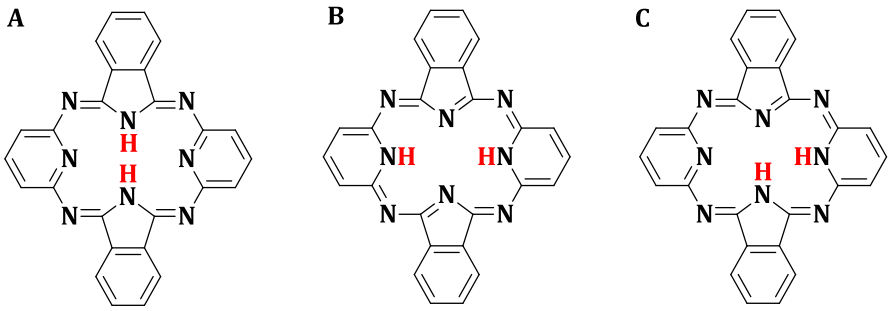


**Figure 4.1:** Possible tautomeric forms of $HpH_2$ (**1**).

Apart from resonance stabilization, the tautomers of **1** differ in their extent of π-conjugation. Tautomer A possesses isolated conjugation paths involving two benzene rings of the isoindole units and the pyridine rings, but it has no resonance structure in which the conjugation is extended over the whole macrocycle. When the two hydrogen atoms are bound to the pyridine units, a fully conjugated 20 π-electron system evolves (Figure 4.1, B).

The tautomeric forms of $HpH_2$ (**1**) have attracted much interest and have been the focus of computational studies aimed at rationalizing the photophysical properties of Hps. [91, 93-95] Hps are believed to exhibit many interesting characteristics because of the competition between several radiation-less decay paths involving the three different tautomeric forms.[93]

### *4.2 Molecular Orbitals of $HpH_2$ and $HpH_2 \cdot H_2O$*

Zakharov *et al.* simulated the electronic spectra of $HpH_2$ (**1**) and $HpH_2 \cdot H_2O$ (**2**) and calculated their molecular orbitals.[92] The HOMO of **1** is $B_1$-symmetric and characterized by the in-phase interactions between the *meso*-nitrogen atoms and the α-carbon atoms of the isoindole moieties as well as the α- and β-carbons of the pyridine rings. Out-of-phase interactions are formed by the *meso*-nitrogen and the α-carbon atoms of the pyridines, as well as the inner nitrogens and the α-carbons of the isoindoles (Figure 4.2, left).

The LUMO of **1** is $B_2$-symmetric. There are bonding interactions between the α- and β-carbons of the isoindole rings and anti-bonding interactions between the nitrogens and the adjacent carbons of the pyridine ring. The *meso*-nitrogens form bonding interactions with the α-carbons of the pyridines and anti-bonding interactions with those of the isoindoles (Figure 4.2, right).

Since a hydrogen-bonded water molecule has little influence on the electronic structure of the macrocycle, the molecular orbitals of $HpH_2 \cdot H_2O$ (**2**) are essentially the same.[92] The first excited electronic state in Hps is almost exclusively a consequence of $\pi \rightarrow \pi^*$ excitation. This transition is symmetry-forbidden and normally inactive in the electronic spectrum.[91, 92]

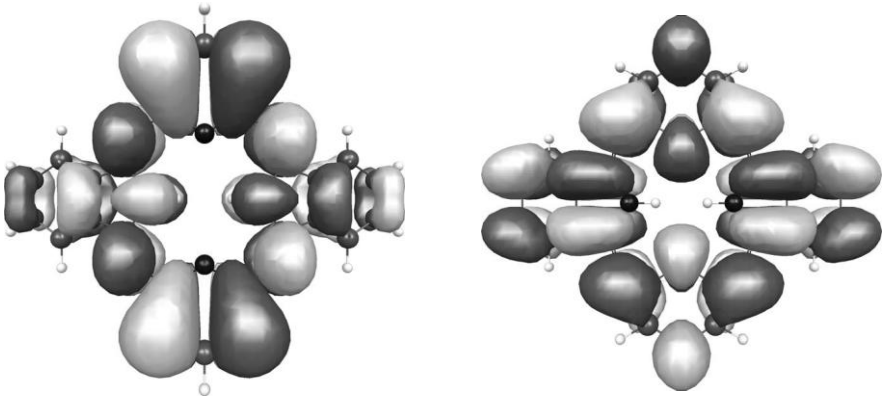

**Figure 4.2**: Left: HOMO of $HpH_2$; Right: LUMO of $HpH_2$. Analysis of MOs was carried out using the *MacMolPlt 7.1* program.[92]

### *4.3 Photophysical Properties of $HpH_2$*

Altucci *et al.* reported that the absorption spectrum of $HpH_2$ (**1**) consists of a large band centered at 350 nm with a shoulder at 420 nm (Figure 4.3, dotted line).[93] While the intense peak at 350 nm has been ascribed to $S_0 \rightarrow S_2$ transitions of tautomer A (Figure 4.1), the weak shoulder at 420 nm was assigned to the comparatively weak, symmetry-forbidden $S_0 \rightarrow S_1$ transitions of the same tautomer.[93] Since there was no significant absorbance reported in the spectral region between 500 nm – 700 nm, the participation of electronic transitions from tautomer B (Figure 4.1) was excluded.[93]

The fluorescence spectrum of **1** is characterized by a dual-wavelength emission with two emission maxima peaked at around 430 nm and 675 nm upon photoexcitation at 380 nm (Figure 4.3, solid line). The band with the maximum at 430 nm was assigned to the radiative decay of the first excited singlet state of tautomer A ($S_{1A}$). This state is populated via internal conversion (IC) from the second excited singlet state of the same tautomer ($S_{2A}$). Apart from relaxation to $S_{1A}$, $S_{2A}$ was reported to undergo IC via single or double ESIPT to either the first excited singlet state of tautomer C ($S_{1C}$) or the first excited singlet state of tautomer B ($S_{1B}$) (Figure 4.4) .

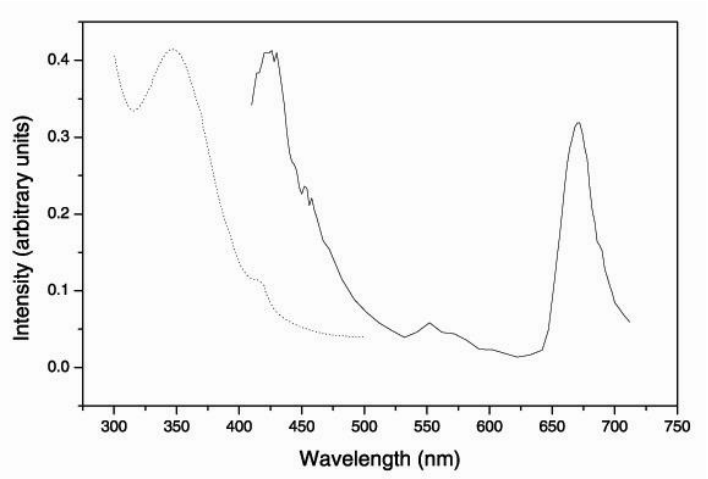


Figure 4.3: Absorption (dotted line) and emission (solid line) spectra of $HpH_2$ (**1**) in DMF upon photoexcitation at 380 nm.[93]

Since computational studies suggested that $S_{1C}$ lies at higher energy than both $S_{1A}$ and $S_{1B}$, this tautomer was proposed to form only transiently during the conversion from tautomer A to tautomer B (Figure 4.4). In agreement with these calculations the emission spectrum of **1** shows only a weak signal at 550 nm (Figure 4.3, full line).[93] Finally, the band at 675 nm was ascribed to the radiative decay of $S_{1B}$ which is formed in the excited state via double intramolecular proton transfer from $S_{2A}$ (Figure 4.4).

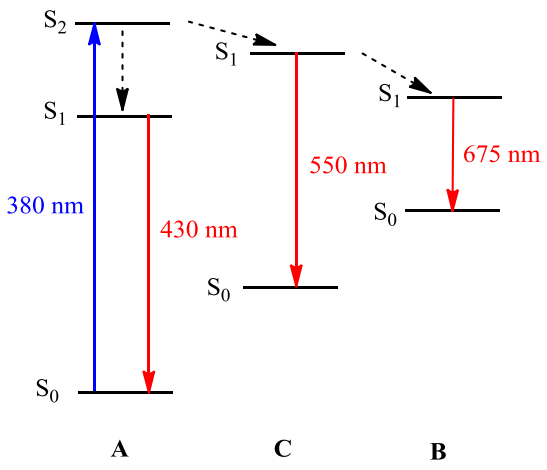


**Figure 4.4**: Previously proposed radiative and radiationless decay paths of $HpH_2$ (**1**).

The dual emission spectrum of $HpH_2$ (**1**) has been ascribed to the formation of emissive Hp tautomers in the excited state,[93-95] but the possible role of ESIPT in Hp photophysics has remained conjecture for over 50 years. Light-induced tautomerization reactions are well-known phenomena for porphyrins and phthalocyanines,[96] but there are other possible explanations for the multi-wavelength emissions from **1**, such as the presence of excitons and/or triplet excited states.[74, 97] These alternative explanations are difficult to investigate due to the low solubility of $HpH_2$ (**1**). As a consequence, we became interested in the photophysical characterization of $HpH_2Zn(OTf)_2$ (**3**) which serves as a non-tautomerizable and soluble analog of $HpH_2$ (**1**). Even though **3** has two theoretically possible tautomers, where the exchangeable protons are located on the peripheral edge of the macrocycle, these tautomers will not undergo ESIPT, given the large distances between the sites of potential exchange (Figure 4.5).

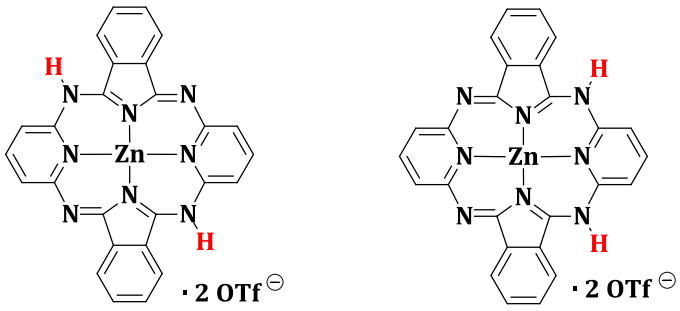


**Figure 4.5:** Tautomeric forms of $HpH_2Zn(OTf)_2$ (**3**).

### *4.4 Photophysical Properties of $HpH_2Zn(OTf)_2$ in Solution*

Upon photoexcitation at 380 nm, $HpH_2Zn(OTf)_2$ (**3**) exhibits concentration-dependent dual-wavelength emission (Figure 4.6). While 56 μM methanolic solutions of **3** exhibit multiple emissions centered at 430 nm and 630 nm, more diluted samples lack the long wavelength emission, but show enhanced fluorescence at shorter wavelengths (Figure 4.6). Since $HpH_2Zn(OTf)_2$ (**3**) is incapable of ESIPT, but nevertheless shows concentration-dependent dual-wavelength emission, it is hypothesized that the true basis for this phenomenon must be related to the aggregation state of Hps.

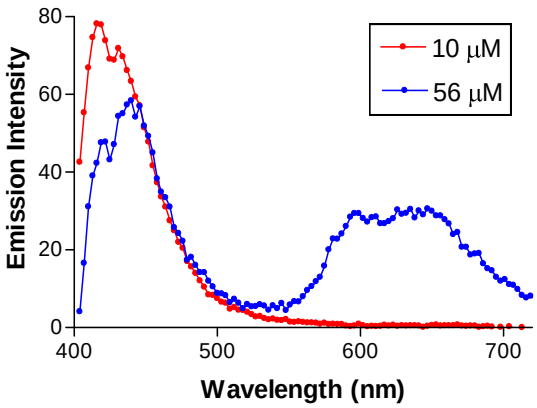


**Figure 4.6**: Emission spectra of $HpH_2Zn(OTf)_2$ (**3**) at 10 μM and 56 μM methanol solutions upon excitation at 380 nm.

To further evaluate the potential impact of aggregation on the photophysical properties of planar Hps, the absorbance spectra of **3** were measured at different concentrations (Figure 4.7). With increasing concentrations of **3**, increased molar extinction coefficients from 430 nm – 500 nm were observed. This is the same wavelength range as predicted for symmetry-forbidden $S_0 \leftrightarrow S_1$ transitions in $HpH_2$ (**1**)[91, 92] and suggests that these transitions become symmetry-allowed in the electronic spectrum upon aggregation.

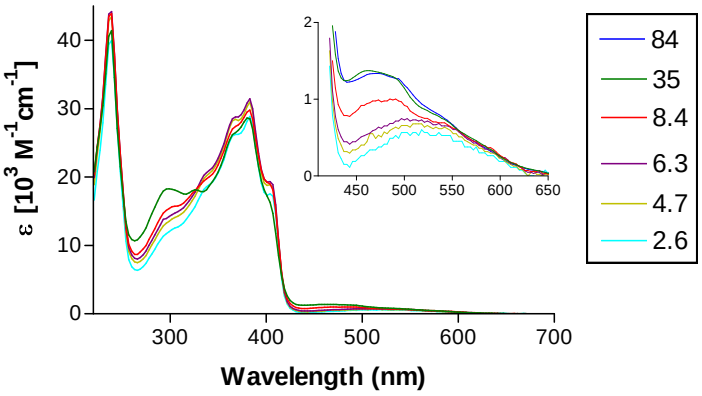


**Figure 4.7**: Absorbance spectra of $HpH_2Zn(OTf)_2$ (**3**) as a function of concentration (μM) in MeOH.

The photophysical properties of porphyrins and phthalocyanines are known to be influenced by their aggregation state. Intensity transfer between the "B-bands" (~400 nm) and "Q-bands" (500 – 650 nm) of porphyrins is enhanced by excitonic coupling between the B- and Q-transition dipoles upon aggregation in solution. This results in enhanced absorbance of the Q-band peaks and splitting of the B-band peaks.[98] Similar trends are observed for $HpH_2Zn(OTf)_2$ (**3**). Dilute methanolic solutions of **3** exhibit strong absorbance peaks centered at 370 nm ($\varepsilon$ = 30'000 $M^{-1}cm^{-1}$) and little absorbance at 450 nm ($\varepsilon \approx 0 - 100\ M^{-1}cm^{-1}$). With increasing concentration of **3**, there is a large increase in absorbance at 450 nm ($\varepsilon \approx 1'300\ M^{-1}cm^{-1}$) and complex splitting of the peaks at 350 – 400 nm (Figure 4.7).

The luminescence of **3** was measured at 450 nm and 650 nm upon photoexcitation at 380 nm at various concentrations (Figure 4.8). A linear increase in fluorescence intensity at 450 nm was observed from 0.1 – 5 μM, followed by a decrease from 7 – 15 μM. This type of linear increase of fluorescence followed by self-quenching is consistent with a monomer-dimer equilibrium between 0.1 – 15 μM. No detectable fluorescence emission was observed at 600 – 700 nm over the same concentration range (Figure 4.8). At concentrations above 20 μM, however, a non-saturating increase in fluorescence emission was observed at 650 nm which suggests the formation of aggregates.

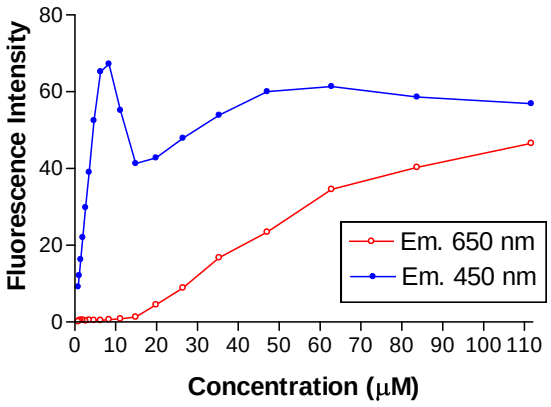


**Figure 4.8**: Concentration-dependent emission of $HpH_2Zn(OTf)_2$ (**3**) at 450 nm and 650 nm in MeOH upon photoexcitation at 380 nm.

Concentration-dependent excitation spectra (Em. = 650 nm) of **3** were measured in MeOH. They revealed two excitation maxima centered at 350 nm and 450 nm (Figure 4.9). These wavelengths are similar to those predicted for $S_0 \leftrightarrow S_2$ and $S_0 \leftrightarrow S_1$ transitions in $HpH_2$ (**1**).[91, 92]

An alternative explanation for the dual-wavelength emission of $HpH_2Zn(OTf)_2$ (**3**) is therefore direct emission from both $S_2 \rightarrow S_0$ (450 nm) and $S_1 \rightarrow S_0$ (650 nm) transitions. This is already a well-known property of aggregated porphyrins and phthalocyanines.[98-100] Aggregation increases the relative abundance of $S_2 \rightarrow S_0$ or "Soret emission" from porphyrins and phthalocyanines,[98, 99] but our results suggest a greater efficiency of $S_1 \leftrightarrow S_0$ excitation and emission for Hps upon aggregation. Even though $S_0 \rightarrow S_1$ transitions are symmetry-forbidden in isolated Hps,[91, 92] excitonic coupling present in aggregated and crystalline hemiporphyrazines might increase the oscillator strength of this transition due to coupling with $S_0 \rightarrow S_2$ transitions.

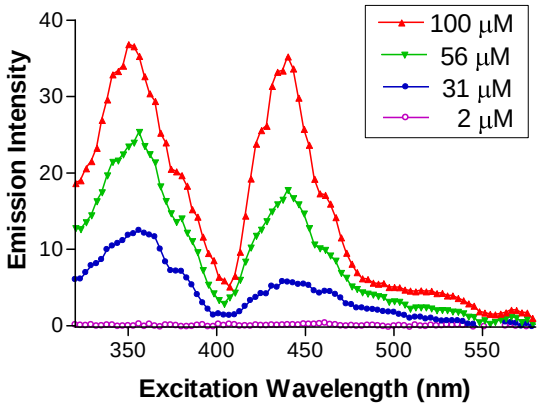


**Figure 4.9**: Concentration-dependent excitation of $HpH_2Zn(OTf)_2$ (**3**) in MeOH (Em = 600 nm).

DMSO is generally a good solvent for planar organic compounds. It should prevent aggregation of $HpH_2Zn(OTf)_2$ (**3**) and diminish its concentration-dependent photophysical properties in solution. Serial dilutions of **3** were therefore conducted in pure DMSO and the corresponding long wavelength absorbance features were measured (Figure 4.10).

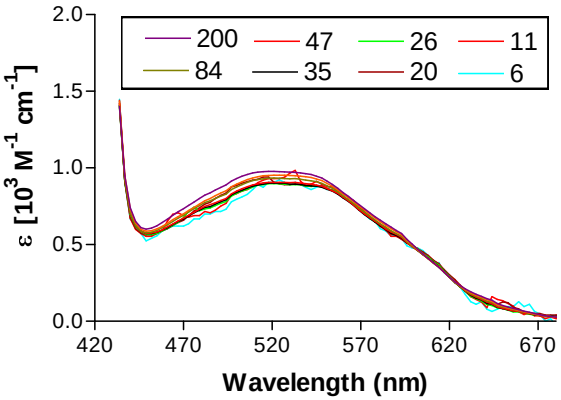


**Figure 4.10**: Concentration-dependent absorbance of $HpH_2Zn(OTf)_2$ (**3**) in DMSO (reported in μM).

In contrast to the results obtained in pure methanol (Figure 4.7), these dilutions obey Beer's law over the entire visible region. The fact that no concentration-dependent effects are observed from 430 nm – 500 nm suggests that Hp aggregation is prevented in DMSO and $S_0 \rightarrow S_1$ transitions remain symmetry-forbidden.

Crystal growth trials revealed that the triflate counterions readily exchange with solvent molecules (Section 3.4.1). As a consequence, MeOH-OTf ligand exchange reactions may have been responsible for the concentration-dependent photophysical properties of **3** observed in pure methanol. A concentration of **3** which allows for the formation of Hp aggregates (83 μM) was therefore chosen and the solvent composition was changed from 100 % methanol to 100 % DMSO. The corresponding emission spectra were recorded upon photoexcitation at 380 nm (Figure 4.11). With increasing DMSO concentrations, the emissions at 650 nm decreased until reaching zero at approximately 20 % DMSO in MeOH. In contrast, the emission intensity at 420 nm increased with increasing DMSO concentrations (Figure 4.11). These results suggest that the concentration-dependent photophysical properties of **3** are a result of aggregation, not ligand exchange.

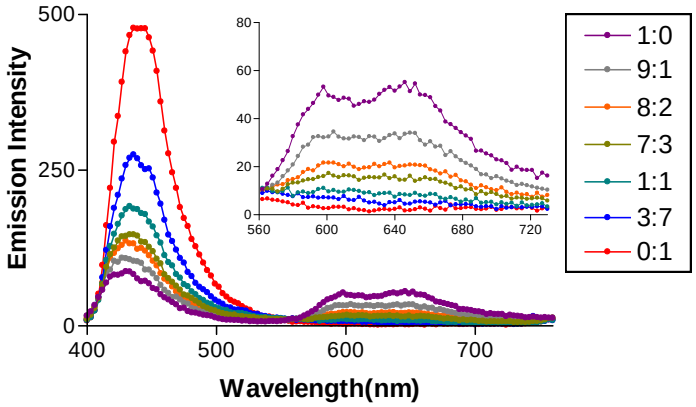


**Figure 4.11:** Emission spectra of $HpH_2Zn(OTf)_2$ (**3**) at 83μM in MeOH/DMSO mixtures upon excitation at 380 nm (reported in MeOH:DMSO ratios).

### *4.5 Photophysical Properties of Hemiporphyrazines in the Solid State*

In our experience and those of others, crystalline $HpH_2$ (**1**) is an insoluble material that readily converts to the non-planar $HpH_2 \cdot H_2O$ (**2**) in solvents containing even small traces of $H_2O$.[65, 68] This conformational flexibility has a profound influence on the Hp photophysics and makes the macrocycle difficult to fully characterize in solution. Consequently, an investigation of the photophysical properties in the solid state can provide more reliable approach for the study of $HpH_2$ (**1**) because it excludes many solvent-mediated effects.

We prepared samples by grinding each crystalline substance with KBr and pressing pellets.[101, 102] Blank-subtracted absorbance spectra of both **1** and $HpH_2Zn(OTf)_2$ (**3**) exhibit relatively strong absorbance between 450 and 600 nm, with distinct features at 500 nm and 550 nm (Figure 4.12). These wavelengths are similar to the "Q-band" transitions of 18 π-electron porphyrins and phthalocyanines.[100, 103-105] The saddle-shaped compound $HpH_2 \cdot H_2O$ (**2**), in contrast, lacks these absorbance features completely (Figure 4.12). These results are in agreement with the absorbance data of **2** and **3** in solution (Figure 4.13). The observed absorbance trends are therefore a result of different conformations of the molecules. While both **1** and **3** are planar and able to form aggregates, **2** is characterized by a saddle-shaped geometry which prevents aggregation and the absorbance at wavelengths in the visible region of the electromagnetic spectrum.

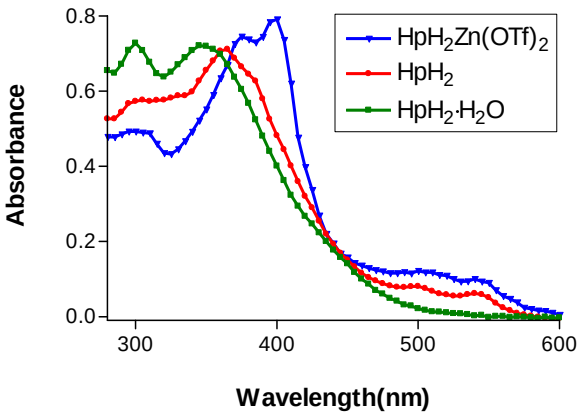


**Figure 4.12:** Absorbance spectra of $HpH_2Zn(OTf)_2$ (**3**), $HpH_2$ (**1**), and $HpH_2{\cdot}H_2O$ (**2**) in pressed KBr pellets.

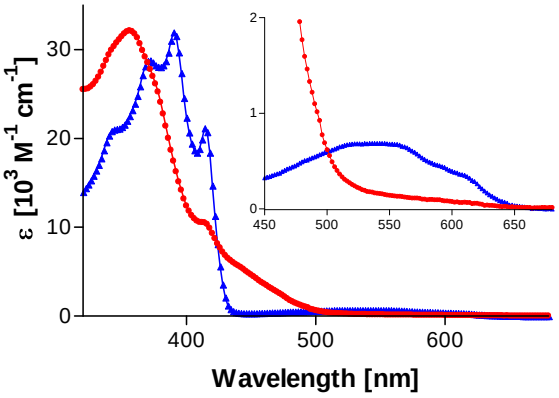


**Figure 4.13:** Absorbance spectra of $HpH_2{\cdot}H_2O$ (**2**, red) and $HpH_2Zn(OTf)_2$ (**3**, blue) in morpholine.

High background emissions from KBr prevented the analysis of the emission features in KBr pellets. Fluorescence emission data were therefore collected using thick layers of neat, microcrystalline materials randomly deposited on polystyrene surfaces. Crystals of both $HpH_2Zn(OTf)_2$ (**3**) and $HpH_2Zn(MeOH)_2{\cdot}2(OTf)$ were measured to gain further insight into the influence that the axial ligands exert on the photophysical properties of Hps. Upon excitation at 350 nm, $HpH_2$ (**1**), $HpH_2Zn(OTf)_2$ (**3**), and $HpH_2Zn(MeOH)_2{\cdot}2(OTf)$ exhibit nearly identical emission spectra, with multiple emission peaks centered at 450 nm, 480 nm, 650 nm, and 720 nm (Figure 4.14).

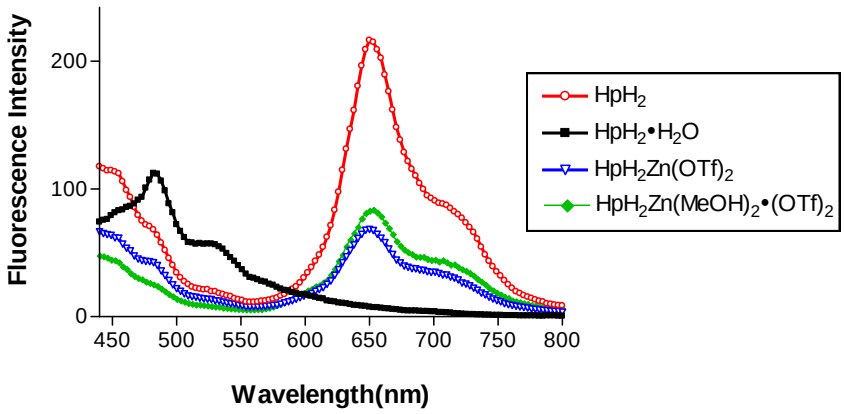


**Figure 4.14**: Fluorescence emission spectra of randomly deposited microcrystalline materials upon excitation at 350 nm.

$HpH_2 \cdot H_2O$ (**2**), in contrast, exhibits multiple emission peaks centered at 450 nm, 480 nm, and 530 nm (Figure 4.14). The luminescent emissions from $HpH_2Zn(OTf)_2$ (**3**) and $HpH_2$ (**1**) in the solid state (650-700nm) are red-shifted by approximately 180 nm as compared to the emissions from the non-planar monohydrate $HpH_2 \cdot H_2O$ (**2**). Since **3** and $HpH_2Zn(MeOH)_2 \cdot 2(OTf)$ show nearly identical luminescence features, MeOH-OTf ligand exchange cannot be responsible for the dual-wavelength emission properties of **3**. These results further demonstrate that the relative planarity of $HpH_2$ (**1**) has a large influence on its photophysical properties.

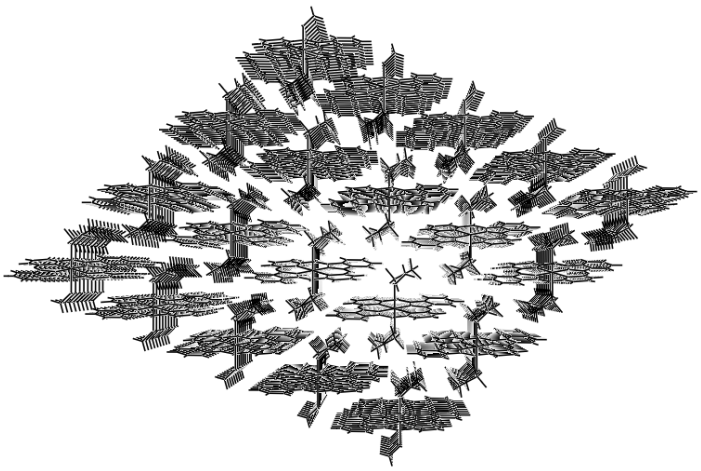

**Figure 4.15:** Packing diagram of $HpH_2Zn(MeOH)_2 \cdot 2(OTf)$.

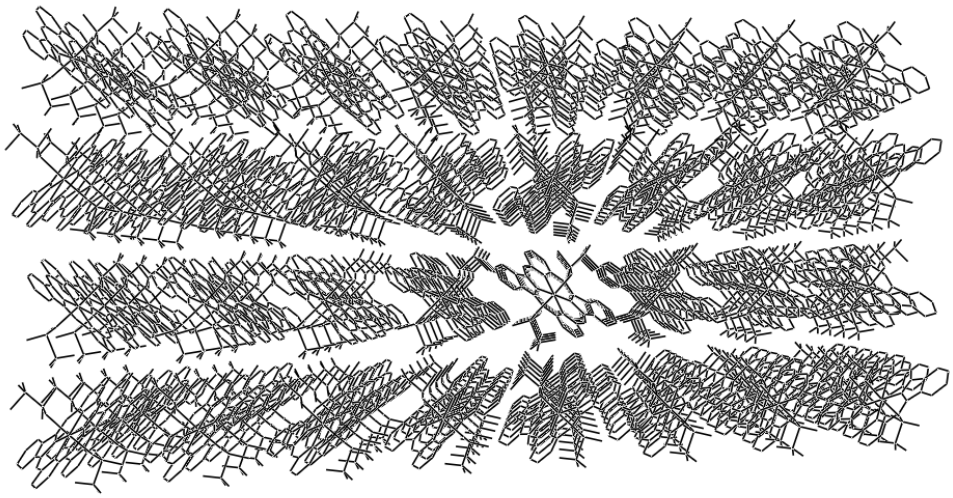

**Figure 4.16**: Packing diagram of $HpH_2Zn(OTf)_2$.

Crystal packing effects may also have a limited influence on the photophysical properties reported here. These crystalline materials exhibit highly diverse packing geometries (Figures 4.15, 4.16, and 3.4), but crystals of $HpH_2Zn(MeOH)_2{\cdot}2(OTf)$ and **1** exhibit absorbance and emission spectra nearly identical to **3** (Figure 4.14). The relative emission intensities from crystalline samples of **1** and **3** at 650 nm versus 440 nm are somewhat greater for the neat materials (Figure 4.14) as compared to the soluble aggregates in solution (Figures 4.6 and 4.11). Together with the concentration-dependent excitation spectra (Figure 4.9), these data demonstrate that the emissions at 650 nm are a result of discrete transitions present only in aggregated and crystalline Hps.

For insight into the nature of emissions from **1** and **3** at 650 nm, fluorescence emission spectra were collected using plane polarized filters (Figure 4.17).[98, 99] Neat samples of $HpH_2$ (**1**), $HpH_2Zn(OTf)_2$ (**3**), and $HpH_2Zn(MeOH)_2{\cdot}2(OTf)$ exhibit very similar behavior, where emissions from 400 – 550 nm are highly polarized and emissions from 650 nm – 700 nm are depolarized. In all three samples, the isotropic emissions from these substances at 650 nm are independent of the excitation wavelengths used (350 nm – 600 nm). Given the aggregation-dependent nature of these emissions, these polarization data further support the formation of delocalized (excitonic) excited state(s) of these materials that emit depolarized photons between 600 nm – 700 nm.

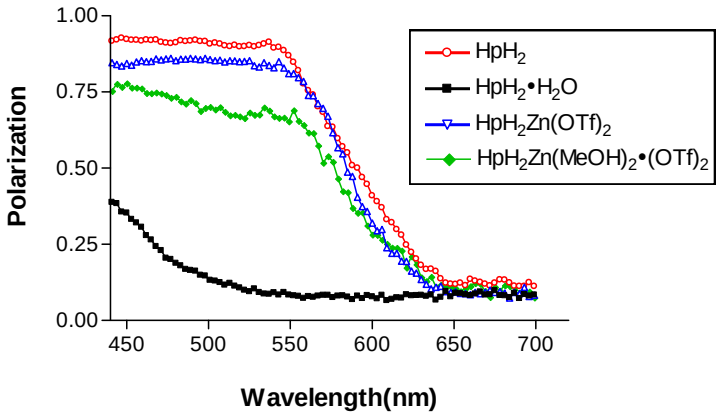


**Figure 4.17**: Fluorescence polarization of randomly deposited microcrystalline materials using excitation at 350 nm. These data were not corrected for instrument response.

# *CHAPTER 5*

# *HYDDROGENATION OF HEMIPORPHYRAZINES*

To assess the potential of Hps as selective GCGC-tetrad ligands, their chemical stability and behavior under various conditions must be determined. Oxidizing and reducing conditions are thereby of major interest because they occur in cells and are relevant to *in vivo* applications. The chemical reactivity of the Hp scaffold under these conditions has not yet been explored. Due to their non-aromatic, 20 π-electron system hemiporphyrazines are expected to exhibit lower chemical stability than the structurally related phthalocyanines. This is supported by their rapid hydrolysis in aqueous acidic media.[65]

Since Hps are often recrystallized from boiling nitrobenzene, which is oxidative under these conditions, the Hp scaffold is assumed to be stable towards mild oxidizing agents. The macrocycle's stability towards reduction has not yet been explored.

## *5.1 Hydrogenation of Porpyrin Derivatives*

Chlorins, bacteriochlorins, and bacterioisochlorins are hydrogenated porphyrin derivatives that occur in a number of vitally important natural compounds. Due to their essential role in nature, the synthesis and characterization of the corresponding tetraazaporphyrin (TAP) analogues, namely tetraazachlorins (TACs, Figure 5.1, left), tetraazabacteriochlorins (TABCs, Figure 5.1, middle), and tetraazaisobacteriochlorins (TAiBCs, Figure 5.1, right) have become of major scientific interest.[106-110] These compounds are characterized by one or two hydrogenated "exocyclic" pyrrole double bonds. Hydrogenated TAP derivatives were first synthesized in 1958 by catalytic hydrogenation of TAP by Linstead *et al.*.[106] TAP was rapidly destroyed over active catalysts such as Adams platinum oxide or W-4 Raney nickel, but the desired hydrogenation proceeded in the presence of palladium black to yield TAC (Figure 5.1, left). The hydrogenated porphyrin derivatives were relatively unstable and prone to atmospheric oxidation in the solid state and in solution.[106]

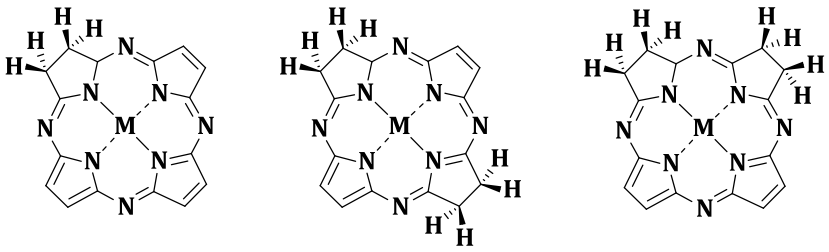

**Figure 5.1:** Structures of TAC (left), TABC (middle), and TAiBC (right).

### *5.2 Hydrogenation of $HpH_2Zn(OTf)_2$*

Since Pd black catalyzes "exocyclic" hydrogenation of porphyrin derivatives, the reactivity of $HpH_2Zn(OTf)_2$ (**3**) towards catalytic hydrogenation was investigated under identical conditions. In contrast to TAPs which undergo peripheral reduction, it was hypothesized that Hps are reactive towards skeletal hydrogenation due to their reduced ring aromaticity. It was anticipated that the iminic *meso*-nitrogen sites of **3** are reactive towards catalytic hydrogenation while the enamine-like *meso*-nitrogens are resistant towards reduction.

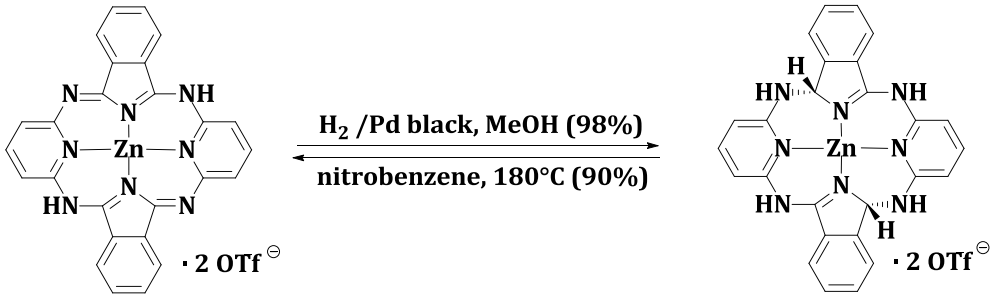


**3** **5**

**Scheme 5.1**: Reversible reduction and oxidation of $HpH_2Zn(OTf)_2$ (**3**).

The reaction of **3** under $H_2$-atmosphere in the presence of palladium black resulted in the co-facial addition of two equivalents of $H_2$ to furnish a new macrocycle "$HpH_4Zn(OTf)_2$" (**5**) (Scheme 5.1). Compound **5** is stable towards atmospheric oxidation in the solid state and can be handled in the presence of water without decomposition. Unsubstituted hydrogenated TAPs, in contrast, are unstable towards atmospheric oxidation.[106]

Crystals of **5**, suitable for crystallographic characterization, were grown from concentrated methanolic solutions by slow diffusion of diethylether/pentane (1:1). The resulting structure of $HpH_4Zn(OH_2)\cdot 2OTf$ has a saddle-shaped conformation with $C_2$-symmetry (Figure 5.2). The axial coordination site of the five-coordinate zinc ion is occupied by a water molecule which is involved in hydrogen bonding in the crystal lattice. It acts as O-H•••O hydrogen bond donor to the triflate counterions (omitted for clarity in Figure 5.2) (H•••O = 1.95(3) Å). The triflate counterions additionally accept N-H•••O hydrogen bonds from the protonated *meso*-nitrogen atoms (H•••O = 2.08(3) and 2.16(7) Å). Bond length analysis confirms reduction at the two iminic *meso*-nitrogen positions. The N4-C1 and C1-N1 bond lengths are symmetric and are in the range of carbon-nitrogen "single-bonds". They measure at 1.433(3) Å and 1.461(2) Å, respectively. In contrast, the N1-C4 (1.308(2) Å) and N1-C1 (1.461(2) Å) are highly asymmetric. These features are in agreement with the structure of **5** (Scheme 5.1).

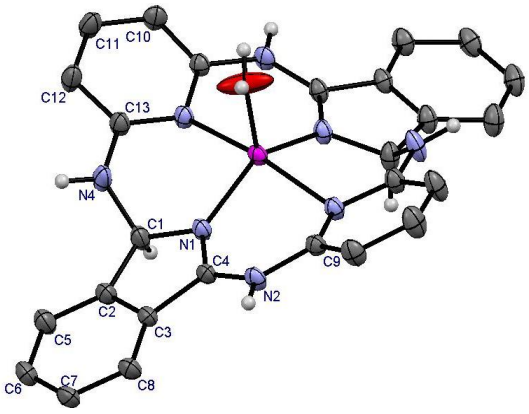


**Figure 5.2**: Crystal structure of $HpH_4Zn(OH_2)\cdot 2(OTf)$. 50% displacement ellipsoids are shown.

$^1$H-NMR analysis further confirms reduction at the iminic C-N double bonds by the presence of two distinct sets of *meso*-nitrogen hydrogens. While the hydrogens bonded to the enamine-like *meso*-nitrogens (N2) give rise to a singlet at 11.4 ppm, the singlet at 8.5 ppm can be assigned to the two hydrogen atoms attached to N4 (Figure 5.3). The signal at 6.4 ppm corresponds to the hydrogens bonded to C1 confirming reduction at the two iminic double bonds (Figure 5.3). The $C_2$-symmetry of **5** is revealed by the presence of one triplet resonance which originates from the pyridine hydrogen atoms bonded to C11.

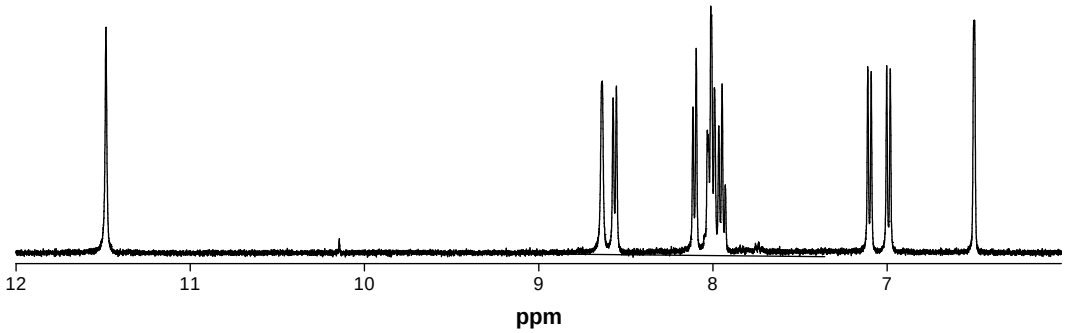


**Figure 5.3:** Extract of $^{1}$H-NMR spectrum of $HpH_4Zn(OTf)_2$ in MeOD.

According to time-dependent NMR and fluorescence measurements, **5** is stable in methanol and DMSO solution at room temperature. However, in nitrobenzene solution at 180 °C the hydrogenated macrocycle readily oxidizes back to the parent compound **3** in high yield (Scheme 5.1).

### *5.3 Photophysical Properties of $HpH_4Zn(OTf)_2$*

Hydrogenation of **3** reduces the extent of π-conjugation across the macrocyclic skeleton causing a significant color change. The initially red $HpH_2Zn(OTf)_2$ (**3**) turns yellow upon reduction to $HpH_4Zn(OTf)_2$ (**5**). These findings can be observed in the absorbance features of **3** and **5** in the visible region of the electromagnetic spectrum (Figure 5.4).

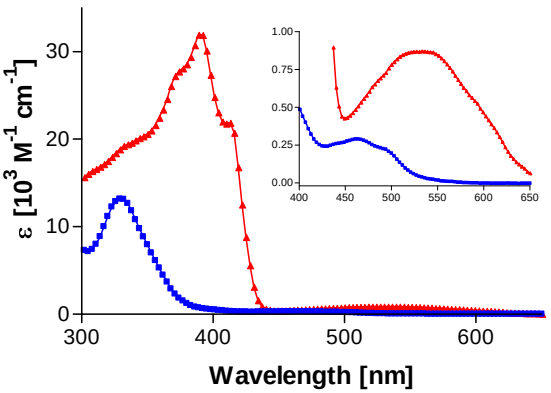


**Figure 5.4**: Absorbance spectra of $HpH_2Zn(OTf)_2$ (red) and $HpH_4Zn(OTf)_2$ (blue) obtained in DMSO.

Compound **3** exhibits a very broad, visible absorption band ($\lambda_{max}$ = 530 nm). While the origin of this absorbance is still unknown,[91, 92, 94] it is shifted to the blue ($\lambda_{max}$ = 460 nm) in the reduced form of the ligand (**5**). This suggests that the absorbance band is a result of extended π-conjugation and planarity of the macrocycle. Since the absorbance features do not change over a wide range of concentrations (200 µM – 4 µM) the possible influence of Hp aggregates can be excluded. Solutions in methanol, in contrast, exhibit aggregate formation as evidenced by concentration dependent absorbance spectra of **3** and **5** (Figures 4.7 and 5.5). The absorption bands of **5**, centered at 240 nm, 280 nm, and 320 nm, exhibit decreasing molar extinction coefficients upon dilution. In contrast, the molar extinction coefficients of the absorbance at 460 nm increase upon dilution (Figure 5.5).

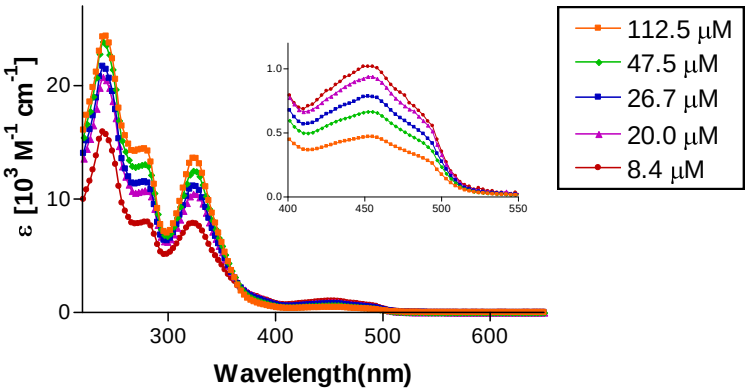


**Figure 5.5**: Concentration-dependent absorbance of $HpH_4Zn(OTf)_2$ (**5**) obtained in MeOH.

Compound **3** exhibits an emission band centered at 420 nm (Ex 350 nm) which was assigned to emissive $S_2$-states (Figure 5.6 and Section 4.4). Since the absorbance features of **3** shift to shorter wavelengths upon reduction, one would expect **5** to be luminescent at wavelengths shorter than 420 nm. Nevertheless, the emission maximum of **3** is red-shifted upon reduction. Compound **5** exhibits a broad emission peaked at 460 nm (Figure 5.6). This suggests the involvement of $S_0 \leftrightarrow S_1$ transitions that become symmetry-allowed upon hydrogenation. Emissive "d-states" can be excluded because zinc has fully occupied d-orbitals and does not typically participate in ligand-to-metal charge transfer (LMCT) reactions.

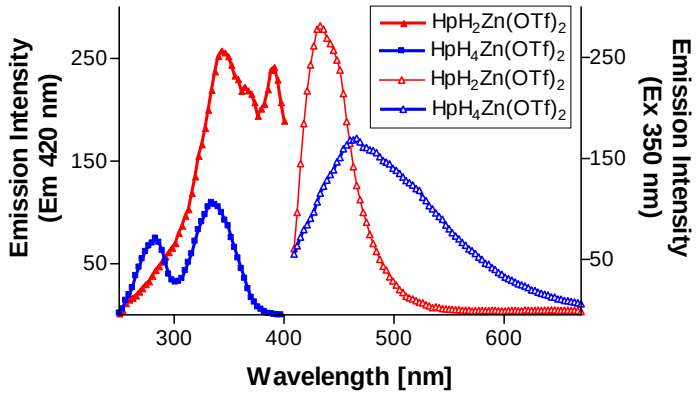


**Figure 5.6:** Excitation (Em. 420 nm) and emission (Ex. 350 nm) spectra of $HpH_2Zn(OTf)_2$ (**3**) and $HpH_4Zn(OTf)_2$ (5) obtained in DMSO solution.

### *5.4 Photophysical Properties of $HpH_4Ni(OTf)_2$*

$HpH_4Ni(OTf)_2$ (**6**) can be obtained by catalytic hydrogenation of $HpH_2Ni(OTf)_2$ (**4**) in the presence of palladium black. Compound **6** is structurally isomorphous to $HpH_4Zn(OTf)_2$ (**5**), but it is expected to exhibit distinct photophysical properties due to the presence of empty d-orbitals in Ni(II). As a consequence, the absorbance (Figure 5.7), luminescence (Figure 5.8), and excitation spectra (Figure 5.9) were recorded under the same conditions as for the analogous zinc compound.

Apart from the additional absorbance band of $HpH_4Ni(OTf)_2$ (**6**) at 430 nm, the absorption spectra of **6** and $HpH_4Zn(OTf)_2$ (**5**) are very similar to each other (Figure 5.7). This suggests that all absorptions at wavelengths shorter than 350 nm as well as the transition at around 470 nm are $\pi \rightarrow \pi^*$ transitions localized on the Hp macrocycle. The additional shoulder in the spectrum of **6** at 430 nm has previously been assigned to the promotion of an electron from a π-level of the macrocycle to the $d_{x2-y2}$-orbital of the nickel(II) atom.[91] Compound **5** lacks this transition because zinc has fully occupied d-orbitals.

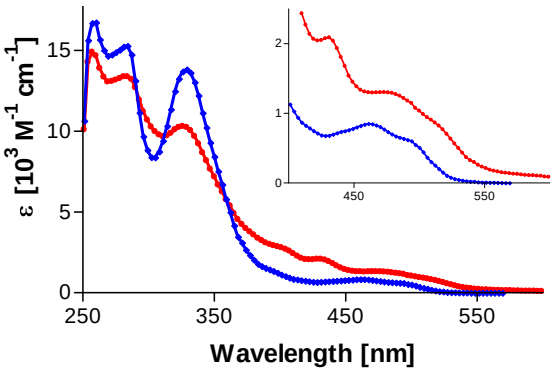


**Figure 5.7**: Absorbance spectra of $HpH_4Zn(OTf)_2$ (**5**, blue) and $HpH_4Ni(OTf)_2$ (**6**, red) obtained in DMSO.

Despite the analogousness of the absorbance features exhibited by **5** and **6**, their emission spectra are very distinct (Figure 5.8). While hydrogenation caused a red-shift of the emission maximum in $HpH_2Zn(OTf)_2$ (**3**) upon photoexcitation at 350 nm, the luminescence of $HpH_2Ni(OTf)_2$ (**4**) is blue-shifted upon reduction. Again, this can be ascribed to the presence of vacant d-orbitals in Ni(II). Nickel(II) containing macrocycles generally display complex photophysical behavior due to a combination of interconnected conformational, electronic, and vibrational changes that take place upon excitation. As a result, these molecules are known to have a very low quantum yield of fluorescence. In the case of nickel(II) porphyrins, calculations have suggested that the normally emissive $\pi \rightarrow \pi^*$ excited state of the porphyrin macrocycle deactivates to produce the lower lying singlet or/and triplet metal centered $d_{z2}$- or $d_{x2-y2}$-excited state which then repopulates the ground state. Our results suggest that the same is true for nickel(II) hemiporphyrazines. Upon photoexcitation at 350 nm ligand-centered excited states are initially populated which then rapidly relax to metal-centered excited states via ligand-to-metal charge transfer (LMCT). These metal-centered excited states return to the ground state by emitting luminescence at shorter wavelengths than zinc(II) Hps.

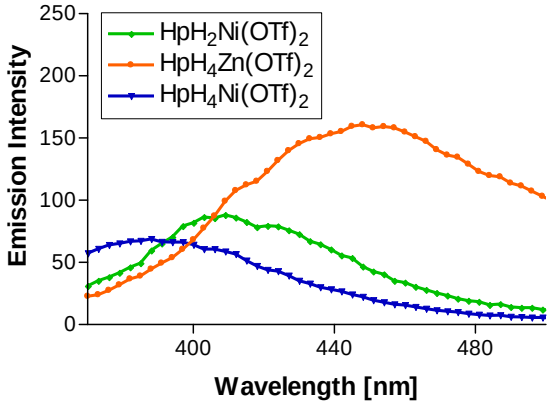


**Figure 5.8**: Emission spectra of $HpH_2Ni(OTf)_2$ (**4**), $HpH_4Ni(OTf)_2$ (**6**), and $HpH_4Zn(OTf)_2$ (**5**) in DMSO upon excitation at 350 nm.

# *CHAPTER 6*

# *SUBSTITUTED HEMIPORPHYRAZINES*

The presence of appropriate peripheral substituents in selective GCGC-tetrad Hp-based ligands is of crucial importance. They provide sufficient water-solubility and may increase the affinity and specificity towards GCGC-tetrads by interacting with the grooves/loops of GCGC-tetrads. While the previous chapters focused on unsubstituted Hps, the final chapter is devoted to the development of synthetic strategies for the introduction of peripheral substituents on the Hp skeleton.

## *6.1 Peripheral Substituted Hemiporphyrazines*

A large number of peripheral substituted Hps has already been reported. Generally, these compounds are obtained from the cyclotetramerization of the corresponding pre-substituted phthalonitrile and/or 2,6-diaminopyridine precursors.[70, 74, 111] Thereby, Hps with variable substituents on the isoindole- and pyridine ring become readily available due to their $C_2$-type symmetry.[66]

In contrast, asymmetrically substituted Pcs are more difficult to obtain. As a result of their $C_4$-type symmetry, Pcs are often synthesized by the tetramerization of a single type of substituted phthalyl compound. This results in the substitution of identical groups on all of the four isoindole rings. The regioselectivity of this reaction is poor and complex product mixtures, containing statistical mixtures of all four possible regioisomers, are typically obtained. Hemiporphyrazines, on the other hand, can be easily obtained as single isomers by the use of 2,6-diaminopyridine derivatives substituted at their 4-position like 4-bromo-2,6-diaminopyridine. This makes Hps interesting targets for applications where single isomers are required.

*6.1.1 Substituted Phthalonitrile Derivatives*

Since Hp scaffold assembly requires high temperature (> 180 °C), the substituted phthalonitrile precursors used for cyclotetramerization must display high thermal stability. Consequently, only a small number of functional groups that are stable under these conditions are typically used as substituents. Since the nitro-group is known to survive high temperature reactions, 4-nitrophthalonitrile (**9**) was considered an interesting starting material for macrocyclization. Compound **9** was synthesized according to a published procedure from phthalimide (Scheme 6.1).[112] Concentrated sulfuric acid and nitric acid readily convert phthalimide to 4-nitrophthalimide (**7**). By the action of concentrated ammonium hydroxide and ammonia, 4-nitrophthalamide (**8**) is obtained from **7**. Finally, 4-nitrophthalonitrile (**9**) was isolated by subsequent dehydration in the presence of thionyl chloride in an overall yield of 46 %.

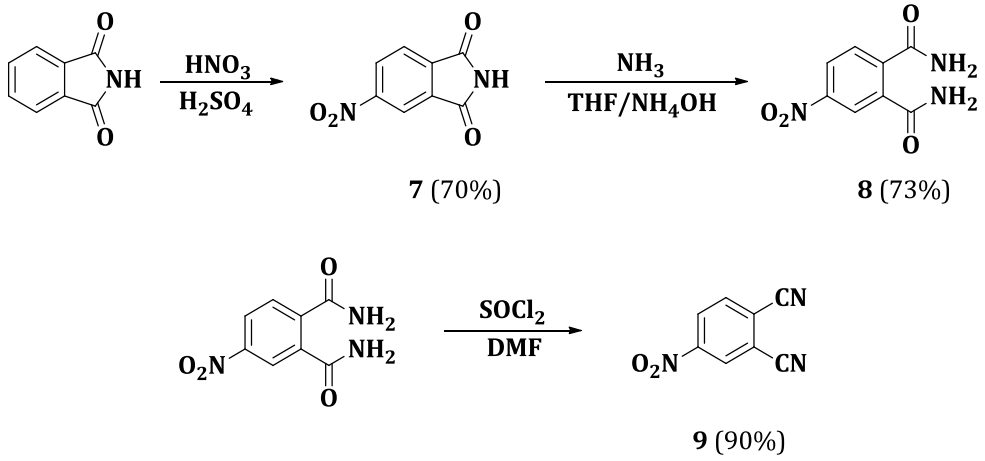


**Scheme 6.1**: Synthesis of 4-nitrophthalonitrile (**9**).

Compound **9** was used directly for macrocyclization by reacting it with 2,6-diaminopyridine in the presence of 1-chloronaphthalene at 260 °C for 24 h in analogy to the synthesis of $HpH_2$ (**1**) (Scheme 6.2). The resulting compound was isolated by vacuum filtration and recrystallized from nitrobenzene to yield **10** as brown needles in 65 % isolated yield. Even though it was previously reported that different regioisomers form by the use of asymmetrically substituted phthalonitriles for Hp assembly,[66] $^1$H-NMR studies suggest that in this particular case, the reaction furnishes a single product. While there is some possibility that the NMR signals of two different regioisomers overlap, similar results were obtained by the synthesis of tetra-amino phthalocyanines by Cong *et al.*.[113]

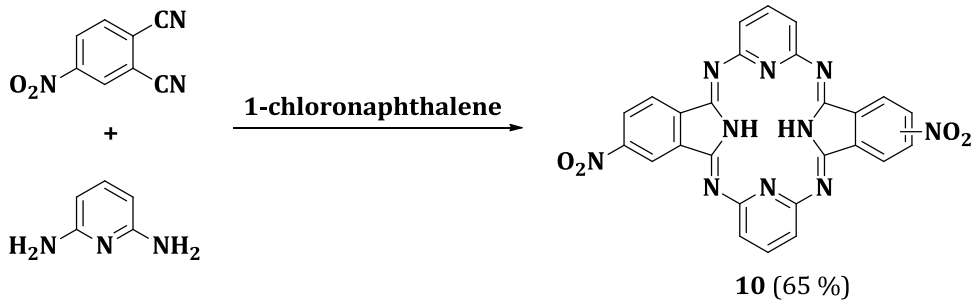


**10** (65 %)

**Scheme 6.2:** Synthesis dinitro-hemiporphyrazine (**10**).

Despite the presence of peripheral nitro-groups in **10**, the compound does not exhibit enhanced solubility compared to $HpH_2$ (**1**). Due to the lack of solubility it proved to be difficult to derivatize the nitro-groups of **10** in subsequent reactions and cosenquently the nitro-group was modified prior to macrocyclization by using **9** as starting material. 4-pyridinepthalonitrile (**13**) was considered another good candidate for macrocylization. The carbon-carbon bond linkage between the phthalonitrile and the peripheral substituent should be stable in high temperature reactions in contrast to heteroatom linkages. Compound **13** was therefore synthesized according to published procedures with a Stille coupling reaction as the key step (Scheme 6.3).[112]

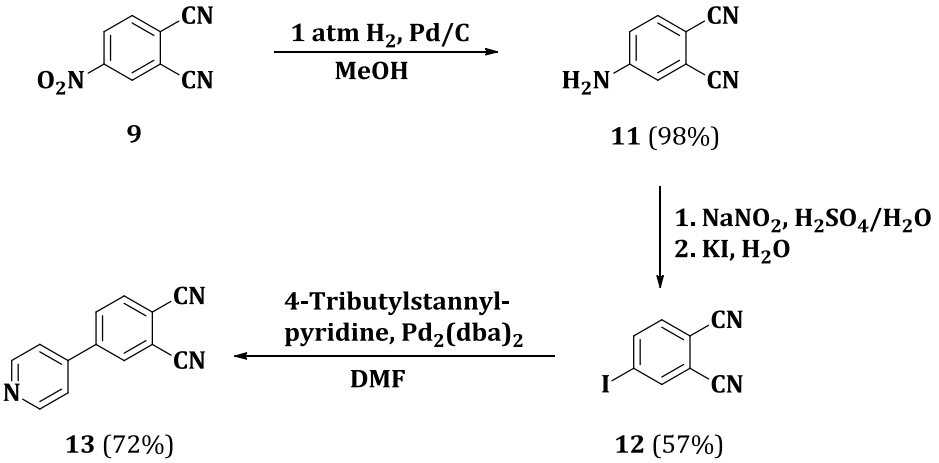


**Scheme 6.3**: Synthesis of 4-pyridinephthalonitrile (**13**).

Compound **9** was reduced under 1 atm $H_2$-atmosphere in the presence of Pd/C to furnish 4-aminophthalonitrile (**11**) in very high yield. This compound was prone to decomposition and therefore the amino-group of **11** was directly substituted by iodide via the diazonium salt to yield 4-iodophthalonitrile (**12**) which is a good electrophile for Stille cross-coupling. In this reaction **12** and 4-tributylstannylpyridine in DMF were stirred in the presence of $Pd_2(dba)_2$ at 80 °C for 17 h to furnish **13** in an overall yield of 40 %.

*6.1.2 Substituted 2,6-Diaminopyridine Derivatives*

The use of symmetrically substituted 2,6-diaminopyridine derivatives for the macrocyclization is very attractive because it avoids the formation of different regioisomers. 4-Bromo-2,6-diaminopyridine (**16**) was identified to be a key intermediate for the desired 2,4,6-substitution pattern in the pyridine ring and was synthesized according to a published procedure (Scheme 6.4).[114] The five-step synthesis afforded **16** in 37 % overall yield with a double Curtius rearrangement as a key transformation.

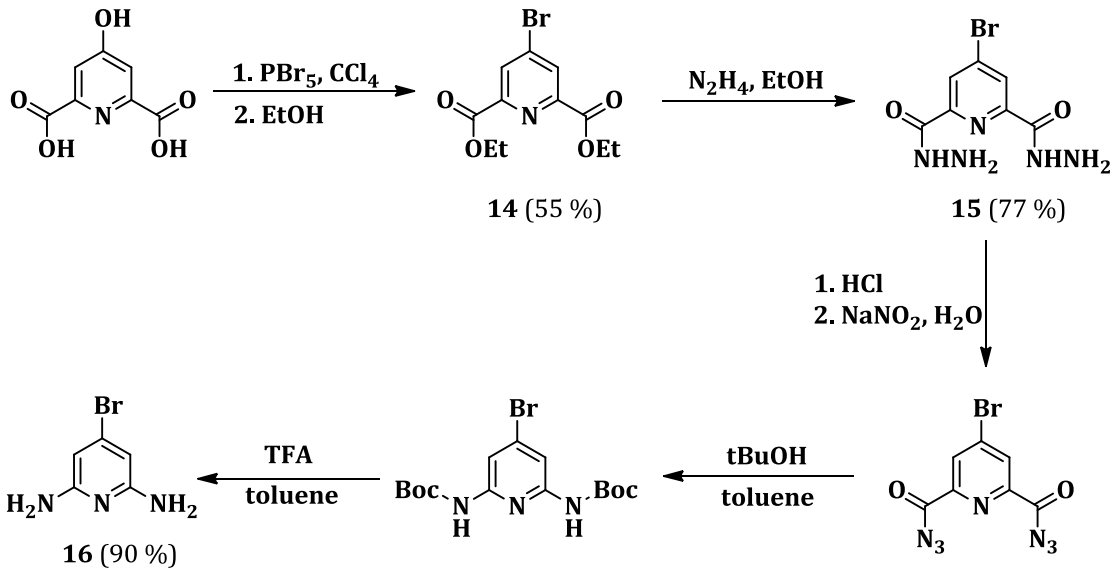


**Scheme 6.4**: Synthesis of 4-bromo-2,6-diaminopyridine (**16**).

The conversion from chelidamic acid to **14** had to be carefully monitored due to the use of a large excess $PBr_5$ in $CCl_4$ at reflux. The intermediate bis-carbonylbromide reacted exothermically with ethanol to form **14**. Conversion of the bis-ester **14** to the bis-hydrazide **15** was achieved by the use of hydrazine monohydrate in ethanol. Careful diazotization of **15** with $NaNO_2$ resulted in the formation of the bis-acyl azide which was dissolved in chloroform. The compound was treated with $MgSO_4$ to remove the water which can cause hydrolysis and considerably limit the reaction yield. To avoid spontaneous decomposition of the bis-acyl azide intermediate in its dry state, it was immediately subjected to a double Curtius rearrangement without further purification or storage. The bis-Boc derivative was deprotected with TFA in DCM to obtain the desired 4-bromo-2,6-diaminopyridine (**16**) in an overall yield of 38 %.

Compound **16** is an attractive but inconvenient precursor for the synthesis of substituted Hps because it is commercially not available and its synthesis involves five demanding steps. 3,5-dibromo-2,6-diaminopyridine (**17**) is a related compound that is much more synthetically accessible. It can be obtained from 2,6-diaminopyridine by electrophilic aromatic bromination in the presence of NBS (Scheme 6.5).

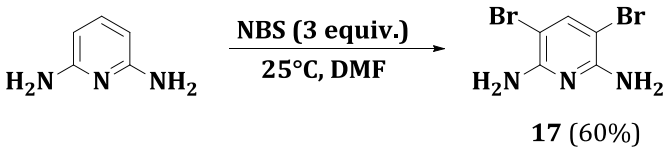


**17** (60%)

**Scheme 6.5**: Synthesis of 3,5-dibromo-2,6-diaminopyridine (**17**).

*6.1.3 Direct Substitution of Hemiporphyrazines*

Early NMR and IR studies on germanium hemiporphyrazines showed that the Hp macrocycle has little ring current associated with it and exhibits low aromaticity.[72, 76] The pyridine rings retain much of their original character and can even be considered as isolated 2,6-diamino/diimmino-pyridine units. The two pyridine moieties of $HpH_2Zn(OTf)_2$ (**3**) were therefore hypothesized to be reactive towards electrophilic aromatic bromination.

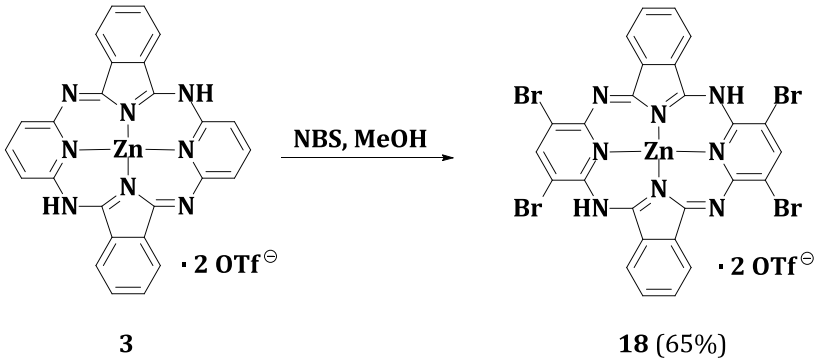


**3** **18** (65%)

**Scheme 6.6**: Direct electrophilic aromatic bromination of $HpH_2Zn(OTf)_2$.

$HpH_2Zn(OTf)_2$ (**3**) and NBS (6 equiv.) were stirred in dry DMF at 25 °C. After 4 h a tetrakis-brominated zinc hemiporphyrazine (**18**) was obtained (Scheme 6.6). The isolated yield (35 %) was significantly lower compared to the bromination of 2,6-diaminopyridine (Scheme 6.5). The major byproduct resulted from deprotonation of **3** by DMF, yielding an insoluble zinc Hp with a dianionic Hp ligand. By changing the solvent from DMF to MeOH, the yield increased to 65 %. MeOH does not deprotonate the *meso*-nitrogen atoms and therefore the insoluble dianionic ligand is not obtained. $^1$H-NMR analysis confirmed that the synthesis resulted in the complete tetrabromination of the compound. No partially brominated Hp derivatives were observed (Figure 6.1). This represents the first example where peripheral substituents are introduced onto the Hp scaffold after macrocyclization.

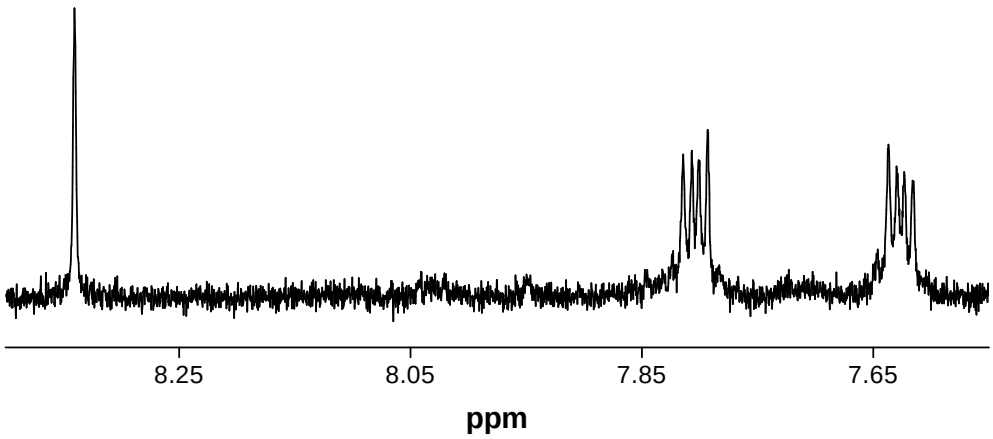


**Figure 6.1:** $^1$H-NMR spectrum of brominated Hp (**18**).

### *6.2 Water Soluble Hemiporphyrazines*

Cell-compatible G-quadruplex ligands should exhibit good water solubility and be stable in aqueous solution. Since the synthesis of a water soluble Hp has not yet been reported, it is an open question whether this macrocycle is stable in neutral aqueous solutions and applicable as an *in vivo* GCGC-tetrad binder. Geiger *et al.* were able to synthesize a partially water soluble Hp analogue by methylation of the corresponding diazahemiporphyrazine (Figure 6.2).[115] They also prepared the corresponding copper and nickel complexes, but did not assess the stability of these compounds in aqueous solution

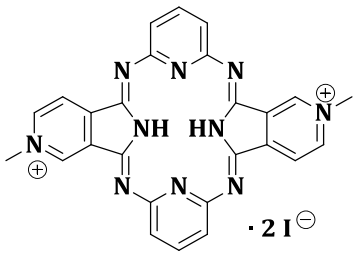


**Figure 6.2:** Structure of a water-soluble hemiporphyrazine derivative.

To directly evaluate the Hps affinity and specificity towards GCGC-tetrads, future studies will be devoted to the synthesis of a water-soluble Hp by the introduction of peripheral water-solubilizing groups either in the isoindole moiety or in the pyridine ring. The already available compounds **13**, **16**, **17**, and **18** will be used as starting materials. A key reaction will be the N-methylation of the peripheral pyridine rings to introduce a positive charge that should increase the water solubility of the Hp. Since N-methylation requires basic conditions, under which Hps are stable, hydrolysis of the macrocycle should not interfere with this synthetic procedure.

## *6.3 Outlook*

### *6.3.1 Water-Solubilizing Groups at the Isoindole Moiety*

In subsequent reactions, 4-pyridinephthalonitrile (**13**) and 2,6-diaminopyridine will be subjected to macrocyclization to furnish a pyridine substituted hemiporphyrazine. This intermediate will subsequently be N-methylated by methyl iodide in the presence of a base (Scheme 6.7).

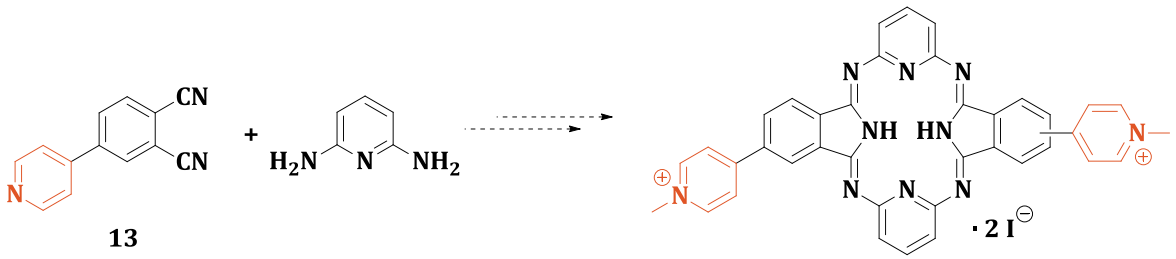


**Scheme 6.7:** Proposed synthesis of a water soluble hemiporphyrazine I.

The presence of methylated pyridine substituents should be sufficient for endowing good water-solubility. The bulky pyridine units can freely rotate along the carbon-carbon bond linkage and should inhibit π-π stacking interactions between neighboring Hp molecules. This synthetic route is very attractive, but it results in the formation of two different regioisomers. This can be prevented when water-solubilizing groups are symmetrically introduced at the pyridine ring.

### *6.3.1 Water-Solubilizing Groups at the Pyridine Moiety*

4-bromo-2,6-diaminopyridine (**16**) can be used as substrate for the formation of a water soluble Hp that will carry the water solubilizing group at the 4-position of the pyridine ring. A key intermediate in this synthetic pathway is a brominated Hp which could be subjected to a palladium catalyzed cross-coupling reaction to substitute the bromines for pyridine rings. In analogy to the previously proposed reaction sequence, N-methyl groups could be introduced by the action of methyl iodide (Scheme 6.8).

This synthetic pathway works only if the bromines are stable under the conditions used for macrocyclization. In case they should turn out not to survive high temperature reactions, **16** could be derivatized in a Stille reaction prior to macrocyclization in analogy to 4-iodophthalonitrile (**12**) (Scheme 6.3).

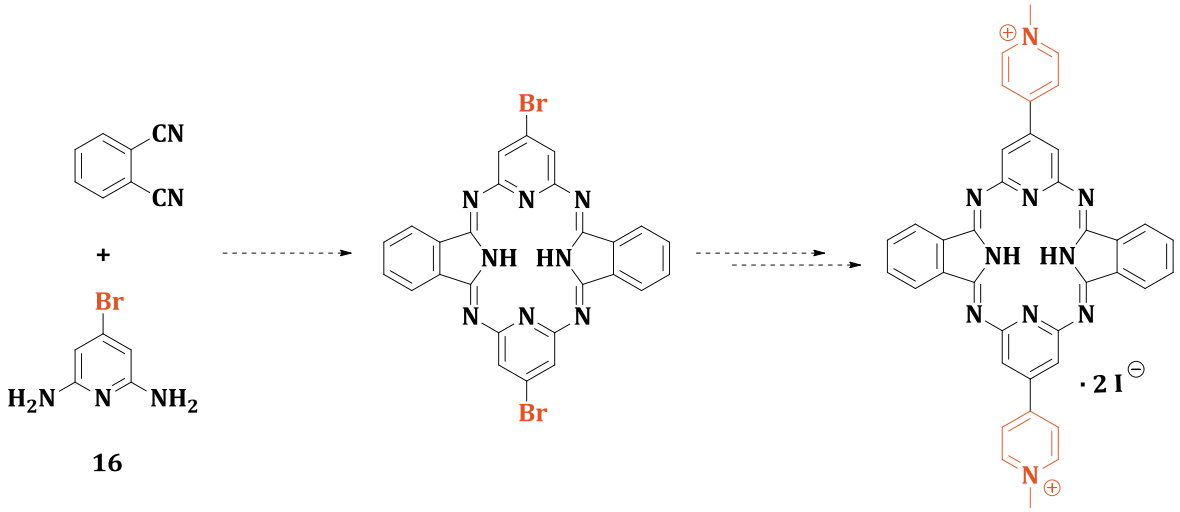


**Scheme 6.8**: Proposed synthesis of a water soluble hemiporphyrazine II.

Alternatively, **18** could be used as precursor to introduce N-methylated pyridine rings (Scheme 6.9). The resulting Hp would contain four water solubilizing groups, whereas the previous compounds were characterized by two such groups. As a consequence, this compound is expected to show enhanced water-solubility.

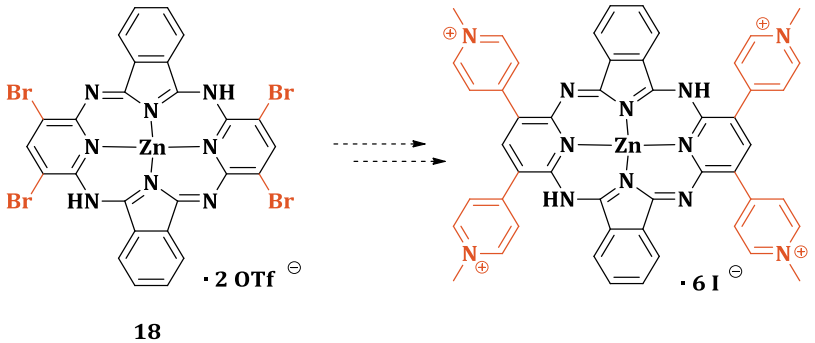


**Scheme 6.9**: Proposed synthesis of a water soluble hemiporphyrazine III.

# *CHAPTER 7*

# *SUMMARY AND CONCLUSIONS*

Hemiporphyrazines (Hps) are 4-unit macrocycles composed of two oppositely-facing isoindole moieties and two co-facial pyridine rings. Experimental studies on these compounds have remained scarce because they have been considered insoluble macrocycles that readily hydrolyze in aqueous acidic solution for over 50 years. Consequently, little is known about their chemical and physical properties and Hps have only rarely been used as building blocks for molecular materials. This thesis was aimed at expanding the current knowledge of Hp synthesis, structure, photophysical properties, and reactivity to assess their potential as selective GCGC-tetrad ligands. This work has revealed that Hps are an interesting class of compounds with promising potentials as GCGC-tetrad binding ligands and as molecular materials for NLO applications and catalysis. The body of work was enabled by the initial synthesis of $HpH_2Zn(OTf)_2$ which could be used as soluble analogue of $HpH_2$ for evaluating the photophysical properties and reactivity of the macrocycle in solution. X-ray diffraction analysis revealed that $HpH_2$ is largely unaffected by the introduction of $Zn(OTf)_2$. Both $HpH_2$ and $HpH_2Zn(OTf)_2$ contain neutral Hp ligands, are essentially planar, exhibit similar trends in bond lengths, and have almost identical photophysical properties.

The aggregation of Hps has a profound impact on their photophysical properties. Soluble aggregates and crystalline materials containing planar hemiporphyrazines exhibit relatively strong absorbance of visible light. Dilute solutions of planar Hps exhibit very little absorbance of visible light in solution. Upon photoexcitation at 380 nm, $HpH_2Zn(OTf)_2$ exhibits concentration-dependent multi-wavelength emissions centered at 450 nm and 650 nm. In contrast to previously proposed theories involving excited state intramolecular proton transfer, our results suggest direct emissions from both $S_2 \rightarrow S_0$ (450 nm) and $S_1 \rightarrow S_0$ transitions (650 nm). The oscillator strength of the $S_1 \leftrightarrow S_0$ transitions is assumed to increase as a result of excitonic coupling present in aggregated and crystalline Hps.

These results may provide both a better understanding of the NLO properties of these materials and provide important design strategies for other future applications of Hps.

Hps are reactive towards chemical modifications as a result of their non-aromatic scaffold. In the presence of palladium black, $HpH_2Zn(OTf)_2$ adds two equivalents of hydrogen co-facially to the macrocycle to furnish $HpH_4Zn(OTf)_2$. This compound is stable towards atmospheric oxidation, but oxidizes to the parent compound in nitrobenzene solution at elevated temperatures. Upon further elaboration, this reversible hydrogenation/dehydrogenation chemistry of $HpH_2Zn(OTf)_2$ might find use in Hp-based reduction/oxidation catalysis.

Furthermore, hydrogenated Hp derivatives emerge as a promising class of compounds to selectively target GCGC-tetrad containing quadruplexes. Thereby, the ligand could undergo oxidation upon quadruplex binding and change its conformation from saddle-shaped to planar (Figure 7.1). Oxidation could be driven by the resulting, energetically favorable π -π stacking interactions between the ligand and the GCGC-tetrads.

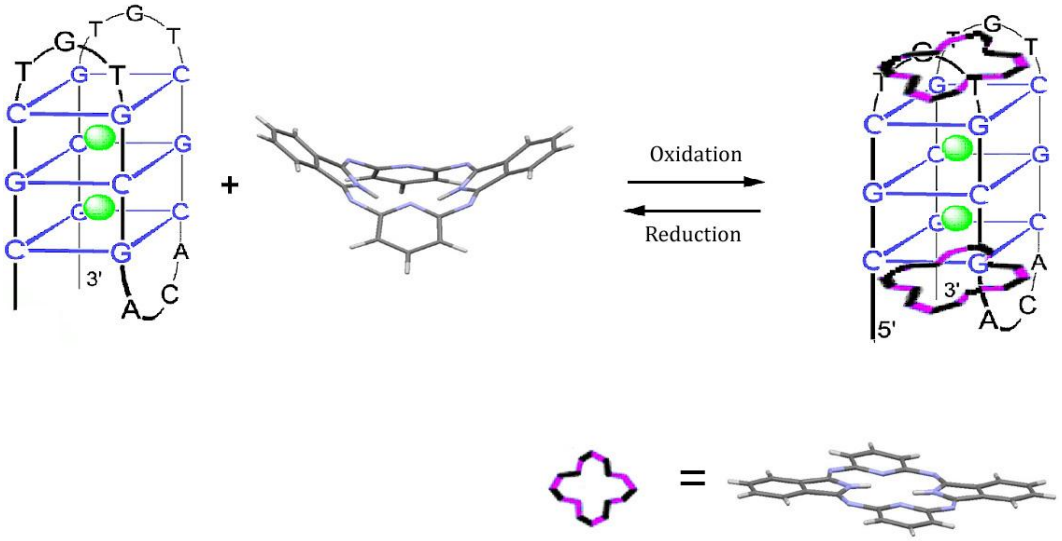


**Figure 7.1:** Schematic representation of conformational change of Hps upon binding to GCGC-tetrad containing quadruplexes.

This approach would provide simple evaluation of the G-quadruplex/ligand interactions by either absorbance or fluorescence measurements. Since reduction of Hps is accompanied by a decrease in the extent of π-conjugation across the macrocycle, the oxidized and reduced forms of the ligand exhibit distinct photophysical properties. In conclusion, Hps are interesting targets as GCGC-tetrad containing quadruplex ligands due to their $C_2$-type symmetry, planarity, and extended π-conjugation across the macrocycle. Their conformational flexibility may allow them to adapt to the quadruplex structure. Since the influence of Hp aggregation and planarity on the photophysical properties is now recognized, the peculiar photophysics of these macrocycles can be used to investigate the ligand/quadruplex interactions. Furthermore, their reactivity towards reversible redox chemistry might lead to a completely new mode of binding between ligand and quadruplex. Reduced, non-planar Hp macrocycles could undergo oxidation to planar Hps upon quadruplex binding inside cells to become capable of exerting strong π- π stacking interactions with the GCGC-tetrads of a quadruplex. To assess this hypothesis, the future synthesis of water soluble Hps will be essential.

# *CHAPTER 8*

# *EXPERIMENTAL PROCEDURES*

## *8.1 General Methods*

Phthalonitrile was purchased from *Fluka*, all other reagents were obtained in the highest commercially available grades from *Sigma Aldrich.* $^{1}$H-NMR spectra were measured on a *Bruker ARX-300* (300 MHz) or *ARX-400* (400 MHz) spectrometer (*Bruker*, Karlsruhe, Germany). The chemical shift values are given in ppm relative to the residual signal from DMSO ($\delta$ = 2.5 ppm) or MeOH ($\delta$ = 3.31 ppm). All data processing was carried out with Topspin (*Bruker*). The mass spectra were measured by the Institute of Organic Chemistry at the University of Zurich. Electrospray ionization (ESI) mass spectra were measured using an Esquire-LC from *Bruker*. Absorbance and fluorescence spectra were measured using a Spectra Max M5 from *Molecular Devices*. X-ray structure determination was performed by the Computer Chemistry and X-ray Structure Analysis Lab of Organic Chemistry at the University of Zurich. The measurements were made on an *Oxford Diffraction SuperNova* diffractometer. Elemental analysis was conducted by the Microanalysis Lab of the Institute of Organic Chemistry at the University of Zurich. Indicated values are the average of two or more independent measurements.

## *8.2 Absorbance and Fluorescence Measurements*

### *8.2.1 Absorbance Measurements in Solution*

The spectra were measured in a quartz cuvette with a 0.2 cm path length over a concentration range of 200 → 25 μM. Below 25 μM, a cuvette with a 1 cm path was used. All reported absorbance data exhibited raw absorbance values of less than 1 AU. No further data correction was performed.

*8.2.2 Absorbance Measurements in KBr*

0.3 mg of each compound was ground with 200 mg of KBr in a mortar and pestle for 5 min. The resulting powder was pressed into a pellet under reduced pressure using Specac 15T manual hydraulic press. The resulting pellets were 13 mm in diameter, 1 mm thick, and appeared transparent to the eye. The pellets were immediately measured at an angle of 30° with respect to the incident beam.

*8.2.3 Fluorescence Measurements in Solution*

The spectra were measured in a quartz cuvette with a 1.0 cm path length. All excitation and emission measurements were recorded at an angle of 90° with respect to the incident beam and all raw data were corrected for inner filter effects of absorbance at each wavelength of excitation "$A(\lambda_{ex})$". The corrected values were obtained by multiplication of the raw intensity values by a correction factor "CF": $CF = 2.303 * A(\lambda_{ex}) / (1 - 10^{-A(\lambda ex)})$ (eq. 1).[116]

*8.2.4 Fluorescence Measurements in the Solid State*

Crystalline substances were ground into a powder and loaded into a polystyrene 96-well plate to a depth of approximately 0.5 mm. All excitation and emission measurements were recorded at an angle of 0° with respect to the incident beam. Emission and polarization spectra were collected by exciting the samples at 350 nm and using a long-pass emission filter at 420 nm. No correction of the raw data was conducted.

## *8.3 Synthetic Methods*

*8.3.1 Hemiporphyrazine ($HpH_2$) (**1**)*

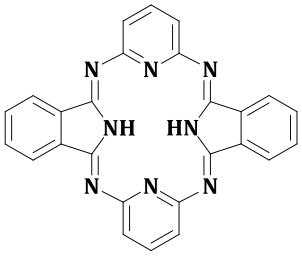


Phthalonitrile (500 mg, 3.90 mmol) and 2,6-diaminopyridine (426 mg, 3.90 mmol) in 1-chloronaphthalene (3 ml) were heated to reflux. After 24 h the solution was cooled to room temperature. The resulting precipitate was isolated by filtration and repeatedly washed with cold methanol. After recrystallization from nitrobenzene **1** resulted as red needles (1.03 g, 60 %). $^1$H-NMR (300 MHz, $d_6$-DMSO): 10.74 (*s br*, 2 H, NH), 7.99 – 7.96 (*m*, 4 H), 7.80 – 7.76 (*m*, 6 H); 6.84 (*d*, *J* = 7.8, 4 H); ESI-MS (m/z): $[M+H]^+$ calc. for $C_{26}H_{17}N_8$, 441; found 441.

The structure of **1** was confirmed by single crystal X-ray diffraction (Table 1).

**Table 1**: *Crystallographic Data of* **1**

| | | |
|---|---|---|
| Crystallised from | | 1-methylnaphthalene |
| Empirical formula | | $C_{26}H_{16}N_8$ |
| Formula weight [g·mol$^{-1}$] | | 440.47 |
| Crystal colour, habit | | red, plate |
| Crystal dimensions [mm] | | 0.05 x 0.11 x 0.20 |
| Temperature [K] | | 160(1) |
| Crystal system | | monoclinic |
| Space group | | $P2_1/n$ (#14) |
| Z | | 2 |
| Reflections for cell determination | | 3704 |
| 2$\theta$ range for cell determination [°] | | 6–148 |
| Unit cell parameters | a [Å] | 14.1690(4) |
| | b [Å] | 4.9988(1) |
| | c [Å] | 15.0572(4) |
| | α [°] | 90 |
| | β [°] | 113.547(3) |
| | γ [°] | 90 |
| | V [Å$^3$] | 977.66(5) |
| *F*(000) | | 456 |
| $D_x$ [g·cm$^{-3}$] | | 1.496 |
| μ(Cu Kα) [mm$^{-1}$] | | 0.764 |
| Scan type | | ω |
| $2\theta_{(max)}$ [°] | | 148 |
| Total reflections measured | | 8403 |
| Symmetry independent reflections | | 1951 |

| | |
|---|---|
| $R_{int}$ | 0.072 |
| Reflections with $I > 2\sigma(I)$ | 1598 |
| Reflections used in refinement | 1951 |
| Parameters refined | 158 |
| Final $R(F)$ [$I > 2\sigma(I)$ reflections] | 0.0495 |
| $wR(F^2)$ (all data) | 0.1452 |
| Weights: | $w = [\sigma^2 (F_0^2) + (0.0827P)^2 + 0.1923P]^{-1}$ where $P = (F_0^2 + 2F_c^2)/3$ |
| Goodness of fit | 1.036 |
| Final $\Delta_{max}/\sigma$ | 0.001 |
| $\Delta\rho$ (max; min) [e Å$^{-3}$] | 0.27; -0.30 |
| $\sigma(d_{(C-C)})$ [Å] | 0.002 – 0.003 |

### *8.3.2 Hemiporphyrazine Monohydrate ($HpH_2 \cdot H_2O$) (**2**)*

**1** (50 mg, 0.11 mmol) was stirred in wet benzyl alcohol at 180 °C for 2 h. The reaction mixture was slowly cooled to room temperature over 24 h. The resulting yellow needles were isolated by vacuum filtration and dried *in vacuo* (51 mg, 98 %).

### *8.3.3 $HpH_2Zn(OTf)_2$ (**3**)*

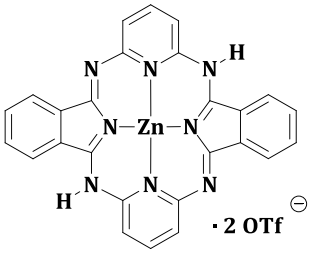


Phthalonitrile (500 mg, 3.90 mmol), 2,6-diaminopyridine (426 mg, 3.90 mmol), and $Zn(HOTf)_2$ (710 mg, 1.95 mmol) were stirred in nitrobenzene (4 ml) at 220 °C for 4 h under $N_2$. The reaction mixture was cooled to room temperature before the resulting precipitate was collected by vacuum filtration, repeatedly washed with $CH_2Cl_2$ and acetone and dried *in vacuo* to yield **3** as red crystals (641 mg, 69 %). $^1$H-NMR (300 MHz, MeOD) 8.20 (*s br*, 2 H), 8.14 (*t*, *J* = 8.0, 2 H), 7.88 – 7.82 (*m*, 8 H), 7.51 (*d*, *J* = 8.0, 4 H); Elem. Anal. for $C_{28}H_{16}F_6N_8O_8S_2Zn$: C 41.83, H 2.01, N 13.94; found: C 41.84, H 2.18, N 13.96.

The structure of **3** was confirmed by single crystal X-ray diffraction (Table 2).

**Table 2:** *Crystallographic Data of* **3**

| | | |
|---|---|---|
| Crystallised from | | MeOH |
| Empirical formula | | $C_{30}H_{24}F_6N_8O_8S_2Zn$ |
| Formula weight [g·mol$^{-1}$] | | 868.06 |
| Crystal colour, habit | | red, prism |
| Crystal dimensions [mm] | | 0.20 x 0.22 x 0.25 |
| Temperature [K] | | 160(1) |
| Crystal system | | triclinic |
| Space group | | *P*-, 1 (#2) |
| *Z* | | 1 |
| Reflections for cell determination | | 9487 |
| 2$\theta$ range for cell determination [°] | | 5.5–56.6 |
| Unit cell parameters | *a* [Å] | 8.2520(2) |
| | *b* [Å] | 10.8769(4) |
| | *c* [Å] | 11.4996(5) |
| | $\alpha$ [°] | 117.121(3) |
| | $\beta$ [°] | 95.376(2) |
| | $\gamma$ [°] | 106.102(5) |
| | *V* [Å$^3$] | 852.88(7) |
| *F*(000) | | 440 |
| $D_x$ [g·cm$^{-3}$] | | 1.690 |
| $\mu$(Mo *K*$\alpha$) [mm$^{-1}$] | | 0.939 |
| Scan type | | $\omega$ |
| $2\theta_{(max)}$ [°] | | 57 |
| Total reflections measured | | 13290 |
| Symmetry independent reflections | | 3780 |
| $R_{int}$ | | 0.019 |
| Reflections with $I > 2\sigma(I)$ | | 3518 |

| | |
|---|---|
| Reflections used in refinement | 3780 |
| Parameters refined | 260 |
| Final $R(F)$ [$I > 2\sigma(I)$ reflections] | 0.0267 |
| $wR(F^2)$ (all data) | 0.0703 |
| Weights: | $w = [\sigma^2(F_0^2) + (0.0318P)^2 + 0.5460P]^{-1}$ |
| | where $P = (F_0^2 + 2F_c^2)/3$ |
| Goodness of fit | 1.059 |
| Secondary extinction coefficient | 0.004(1) |
| Final $\Delta_{max}/\sigma$ | 0.001 |
| $\Delta\rho$ (max; min) [e Å$^{-3}$] | 0.39; -0.35 |
| $\sigma(d_{(C-C)})$ [Å] | 0.002 – 0.003 |

### *8.3.4 $HpH_2Ni(OTf)_2$ (**4**)*

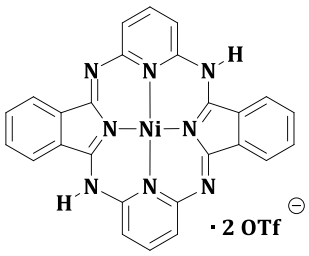


Phthalonitrile (500 mg, 3.90 mmol), 2,6-diaminopyridine (426 mg, 3.90 mmol), and $Ni(OTf)_2$ (696 mg, 1.95 mmol) were stirred in nitrobenzene (4 ml) at 220 °C for 4 h under $N_2$. The reaction mixture was cooled to room temperature. The resulting precipitate was collected by vacuum filtration, repeatedly washed with $CH_2Cl_2$ and acetone and dried *in vacuo* to yield **4** as red crystals (701 mg, 72 %).

The structure of **4** was confirmed by single crystal X-ray diffraction (Table 3).

**Table 3**: *Crystallographic Data of* **4**

| | | |
|---|---|---|
| Crystallised from | | Methanol |
| Empirical formula | | $C_{30}H_{24}F_6N_8NiO_8S_2$ |
| Formula weight [g·mol$^{-1}$] | | 861.38 |
| Crystal colour, habit | | red, prism |
| Crystal dimensions [mm] | | 0.10 x 0.12 x 0.24 |
| Temperature [K] | | 160(1) |
| Crystal system | | triclinic |
| Space group | | P$^{-}$,1 (#2) |
| Z | | 1 |
| Reflections for cell determination | | 8441 |
| 2$\theta$ range for cell determination [°] | | 4–57 |
| Unit cell parameters | a [Å] | 8.2327(6) |
| | b [Å] | 10.8637(8) |
| | c [Å] | 11.4577(6) |
| | α [°] | 117.215(6) |
| | β [°] | 95.153(5) |
| | γ [°] | 106.616(6) |
| | V [Å$^3$] | 843.49(1) |
| *F*(000) | | 438 |
| $D_x$ [g·cm$^{-3}$] | | 1.696 |
| μ(Mo Kα) [mm] | | 0.797 |
| Scan type | | ω |
| 2$\theta_{(max)}$ [°] | | 56.9 |
| Total reflections measured | | 12900 |
| Symmetry independent reflections | | 3692 |
| $R_{int}$ | | 0.025 |

| | |
|---|---|
| Reflections with $I > 2\sigma(I)$ | 3300 |
| Reflections used in refinement | 3692 |
| Parameters refined | 259 |
| Final $R(F)$ [$I > 2\sigma(I)$ reflections] | 0.0349 |
| $wR(F^2)$ (all data) | 0.0946 |
| Weights: | $w = [\sigma^2 (F_0^2) + (0.0332P)^2 + 1.0921P]^{-1}$ where $P = (F_0^2 + 2F_c^2)/3$ |
| Goodness of fit | 1.124 |
| Final $\Delta_{max}/\sigma$ | 0.001 |
| $\Delta\rho$ (max; min) [e Å$^{-3}$] | 0.52; -0.41 |
| $\sigma(d_{(C-C)})$ [Å] | 0.003 – 0.004 |

### *8.3.5 $HpH_4Zn(OTf)_2$ (**5**)*

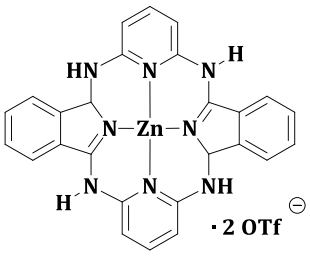


**3** (300 mg, 0.56 mmol) and Pd black (3 mg, 0.03 mmol) were stirred in methanol (2 ml) under 1 atm $H_2$-atmosphere at 25 °C for 2 h. Pd black was removed by filtration over celite and the amount of methanol was reduced to half of its initial volume under reduced pressure. The remaining solution was layered with diethylether/pentane (1:1, 0.5 ml). The resulting yellow crystals were isolated by filtration and washed with diethylether and $CH_2Cl_2$ to afford **5** as yellow crystals (278 mg, 98%). $^1$H-NMR (400 MHz, $d_6$-DMSO) 11.36 (*s br*, 2 H), 8.52 (*d*, *J* = 2.7, 2 H), 8.44 (*d*, *J* = 7.6, 2 H), 7.98 (*d*, *J* = 7.3), 7.91 – 7.81 (*m*, 6 H), 6.98 (*d*, *J* = 7.9, 2 H), 6.87 (*d*, *J* = 8.3, 2 H), 6.34 (*d*, *J* = 2.5, 2 H); $^{13}$C-NMR (100 MHz, $d_6$-DMSO) 160.84, 158.58, 150.86, 144.79, 141.77, 132.43, 131.63, 130.07, 124.79, 123.07, 108.03, 105.14, 75.93; Elem. Anal. for $C_{28}H_{22}F_6N_8O_7S_2Zn$: C 40.71, H 2.68, N 13.57; found C 40.56, H 2.75, N 13.44.

The structure of **5** was confirmed by single crystal X-ray diffraction (Table 4).

**Table 4**: *Crystallographic Data of* **5**

| | | |
|---|---|---|
| Crystallised from | | MeOH / $Et_2O$ / pentane |
| Empirical formula | | $C_{28}H_{22}F_6N_8O_7S_2Zn$ |
| Formula weight [g·mol$^{-1}$] | | 826.02 |
| Crystal colour, habit | | orange, prism |
| Crystal dimensions [mm] | | 0.20 x 0.23 x 0.28 |
| Temperature [K] | | 160(1) |
| Crystal system | | monoclinic |
| Space group | | C2/c (#15) |
| Z | | 4 |
| Reflections for cell determination | | 12426 |
| 2$\theta$ range for cell determination [°] | | 6–61 |
| Unit cell parameters | a [Å] | 20.9506(3) |
| | b [Å] | 10.1673(1) |
| | c [Å] | 16.0497(2) |
| | α [°] | 90 |
| | β [°] | 107.343(1) |
| | γ [°] | 90 |
| | V [Å$^3$] | 3263.34(8) |
| *F*(000) | | 1672 |
| $D_x$ [g·cm$^{-3}$] | | 1.681 |
| μ(Cu Kα) [mm$^{-1}$] | | 0.975 |
| Scan type | | ω |
| $2\theta_{(max)}$ [°] | | 61 |
| Total reflections measured | | 21655 |
| Symmetry independent reflections | | 4547 |
| $R_{int}$ | | 0.021 |

| | |
|---|---|
| Reflections with $I > 2\sigma(I)$ | 4152 |
| Reflections used in refinement | 4547 |
| Parameters refined | 248 |
| Final $R(F)$ [$I > 2\sigma(I)$ reflections] | 0.0351 |
| w$R(F^2)$ (all data) | 0.1009 |
| Weights: | $w = [\sigma^2 (F_0^2) + (0.0553P)^2 + 4.6680P]^{-1}$ where $P = (F_0^2 + 2F_c^2)/3$ |
| Goodness of fit | 1.060 |
| Final $\Delta_{max}/\sigma$ | 0.001 |
| Δρ (max; min) [e Å$^{-3}$] | 0.80; -0.85 |
| $\sigma(d_{(C-C)})$ [Å] | 0.002 – 0.003 |

### *8.3.6 $HpH_4Ni(OTf)_2$ (**6**)*

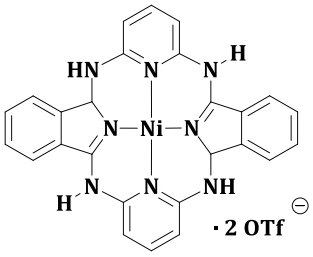


**4** (300 mg, 0.60 mmol) and Pd black (3 mg, 0.03 mmol) were stirred in methanol (2 ml) under 1 atm $H_2$-atmosphere at 25 °C for 2 h. Pd black was removed by filtration over celite and the amount of methanol was reduced to half of its initial volume under reduced pressure. The remaining solution was layered with diethylether/pentane (1:1, 0.5 ml). The resulting yellow crystals were isolated by filtration and washed with diethylether and $CH_2Cl_2$ to afford **6** as yellow crystals (296 mg, 98%). ESI-MS (m/z): $[M+H]^+$ calc. for $C_{26}H_{20}N_8Ni$, 502; found 502.

### *8.3.7 4-Nitrophthalimide (**7**)*

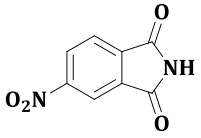

Phthalimide (20 g, 135.9 mmol) was added to a solution of fuming $HNO_3$ (28 ml) in concentrated $H_2SO_4$ (112 ml) at 0°C. The yellow reaction mixture was stirred at 35°C for 45 min before it was poured into cold $H_2O$ (400 ml). The resulting colorless precipitate was isolated by vacuum filtration and washed with $H_2O$. After recrystallization from ethanol (700 ml) **7** resulted as colorless crystals (11.2 g, 43%). $^1$H-NMR (400 MHz, $d_6$-DMSO) 11.81 (*s br*, 1 H), 8.61 (*dd*, *J* = 8.2, 2.0, 1 H), 8.43 (*d*, *J* = 2.0, 1 H), 8.07 (*d*, *J* = 8.2, 1 H); $^{13}$C-NMR (100 MHz, $d_6$-DMSO) 167.52, 167.23, 151.37, 137.29, 134.04, 134.04, 129.43, 124.46, 117.74.

### *8.3.8 4-Nitrophthalamide (**8**)*

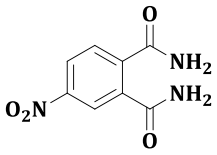

**7** (4 g, 20.8 mmol) was dissolved in THF (40 ml). Concentrated $NH_4OH$ (29 ml) was added at 40°C, before $NH_3$ was bubbled through the solution for 2 h. The solution was cooled to 0°C before the colorless precipitate was collected by vacuum filtration and washed well with $H_2O$. **8** resulted as a colorless solid (2.9 g, 67%). $^1$H-NMR (400 MHz, $d_6$-DMSO) 8.31 (*dd*, *J* = 8.3, 2.3, 1 H), 8.28 (*d*, *J* = 2.3, 1 H), 8.02 (*s*, 1 H), 7.96 (*s*, 1 H), 7.70 (*d*, *J* = 8.3, 1 H), 7.59 (*s*, 1H); $^{13}$C-NMR (100 MHz, $d_6$-DMSO) 168.66, 167.65, 147.10, 142.65, 137.22, 129.15, 124.35, 122.4; ESI-MS: 360.4 $[M+NaI+H]^+$, 242.2 $[M+MeOH+H]^+$, 231.9 $[M+Na]^+$.

### *8.3.9 4-Nitrophthalonitrile (**9**)*

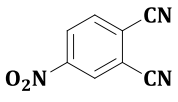

$SOCl_2$ (0.7 ml, 9.6 mmol) was added to ice-cooled DMF (7 ml). After addition of **8** (1 g, 4.8 mmol), the reaction mixture was stirred for 45 minutes at 0° before the temperature was raised to 25° for additional 2 h. The solution was poured into cold $H_2O$. The resulting colorless precipitate was isolated by vacuum filtration, washed with $H_2O$ and concentrated $NaHCO_3$, and dried in vacuo. **9** resulted as a colorless solid (650 mg, 79%). $^1$H-NMR (400 MHz, $d_6$-DMSO) 8.96 (*s*, 1 H), 8.69 (*d*, *J* = 8.2, 1 H), 8.36 (*d*, *J* = 8.2, 1 H); $^{13}$C-NMR (100 MHz, $d_6$-DMSO) 135.57, 128.91, 128.32, 121.79, 118.42, 114.20, 113.96.

*8.3.10 Dinitro-hemiporphyrazine (**10**)*

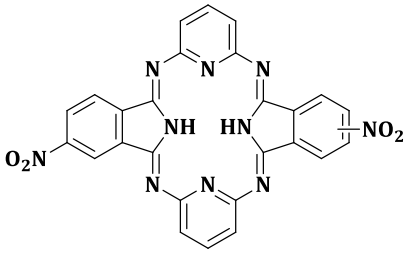

**9** (675 mg, 3.90 mmol) and 2,6-diaminopyridine (426 mg, 3.90 mmol) in 1-chloronaphthalene (3 ml) were heated to reflux. After 24 h the solution was cooled to room temperature. The resulting precipitate was isolated by filtration and repeatedly washed with cold methanol. After recrystallization from nitrobenzene **10** resulted as red needles (1.39 g, 65 %). $^1$H-NMR (300 MHz, $d_6$-DMSO): 11.23 (*s br*, 2 H, NH), 8.61 – 8.59 (*m*, 4 H), 8.24 (*d*, *J* = 8.2, 2 H), 7.90 (*t*, *J* = 4.9, 2 H), 6.95 (*d*, *J* = 7.7, 4 H).

*8.3.11 4-Aminophthalonitrile (**11**)*

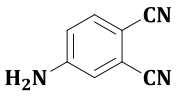

A suspension of **9** (100 mg, 0.6 mmol) and Pd/C (11.5 mg) in MeOH (3 ml) was stirred at room temperature under $H_2$ atmosphere for 6 h. Pd/C was removed by filtration over celite and MeOH was evaporated under reduced pressure. After recrystallization from MeOH **11** resulted as a white solid (84 mg, 98 %).$^1$H-NMR (400 MHz, MeOD) 7.55 (*d*, *J* = 8.7, 1 H), 7.03 (*d*, *J* = 2.3, 1 H), 6.92 (*dd*, *J* = 8.7, 2.3, 1 H).

*8.3.12 4-Iodophthalonitrile (**12**)*

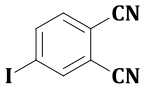

A suspension of **11** (157 mg, 1.10 mmol) in aqueous $H_2SO_4$ (25%) was cooled to 0°C. A solution of $NaNO_2$ (88 mg, 1.28 mmol) in $H_2O$ (254 µl) was added dropwise with stirring, while the temperature of the mixture was kept at 0 °C. Stirring was continued at 0°C for 30 min before KI (198 mg, 1.19 mmol) in $H_2O$ (1.2 ml) was added. The resulting reaction mixture was stirred for 90 min at room temperature before the product was extracted with EtOAc. The organic phases were washed with cold $H_2O$, $NaHCO_3$, cold $H_2O$, saturated $Na_2S_2O_3$, and cold $H_2O$, dried over $MgSO_4$ and EtOAc was evaporated under reduced pressure. After purification by flash chromatography (hexane/EtOAc 1:1) **12** resuled as orange solid (160 mg, 57 %). $^1$H-NMR (400 MHz, $CDCl_3$) 8.61 (*d*, *J* = 1.4, 1 H), 8.10 (*dd*, *J* = 8.3, 1.4, 1 H), 7.50 (*d*, *J* = 8.3, 1 H); EI-MS: 253.9 [M], 127 [M-I], 100 [M-I-CN], 75, 50.

### *8.3.13 4-Pyridinephthalonitrile (**13**)*

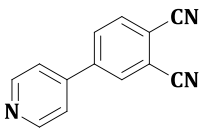


Under an argon atmosphere, **12** (80 mg, 0.31 mmol) in DMF (1 ml) was added to $Pd_2(dba)_3$ (12 mg, 0.01 mmol) in DMF (1 ml). The resulting mixture was stirred for 5 min. 4-Tributylstannylpyridine (99 mg) in DMF (1 ml) was added and the solution was stirred at 80 °C for 17 h. The reaction mixture was poured into 10 % aqueous KF (15 ml) and the product was extracted with EtOAc. The organic phase was washed with 5 % aqueous LiCl and $H_2O$, dried over $MgSO_4$ and the solvent was removed under reduced pressure. After purification by flash chromatography (pentane/$Et_2O$ 4:1) **13** was obtained as colorless solid (46 mg, 72 %). $^1$H-NMR (400 MHz, $CDCl_3$) 8.81 - 8.79 (*m*, 2 H), 8.05 (*s*, 1 H), 7.97 - 7.96 (*m*, 2 H), 7.52 - 7.50 (*m*, 2H).

### *8.3.14 4-Bromopyridine-2,6-dicarboxylic acid diethyl ester (**14**)*

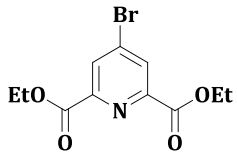


A mixture of chelidamic acid monohydrate (2.9 g, 14.4 mmol) and $PBr_5$ (25 g, 58 mmol) in $CCl_4$ (40 ml) was heated to reflux for 14 h. The reaction mixture was cautiously treated with EtOH (30 ml) and afterwards stirred at 80°C for 30 min. Ethanol was removed under reduced pressure. The remaining solution was poured into cold $H_2O$ (200 ml). The resulting colorless precipitate was isolated by vacuum filtration and washed with $H_2O$. After recrystallization from ethanol **14** resulted as colorless needles (3.0 g, 69 %). $^1$H-NMR (400 MHz, $d_6$-DMSO): 8.42 (*s*, 2 arom. H); 4.40 (*q*, *J* = 2.9, 4 H, $OCH_2$); 1.35 (*t*, *J* = 2.9, 6 H, $CH_3$); $^{13}$C-NMR (100 MHz, $d_6$-DMSO): 162.96, 149.07, 134.24, 130.55, 61.93, 14.00; ESI-MS (m/z): $[M+Na]^+$ calc. for $C_{11}H_{12}BrNO_4$, 324; found 324.

### *8.3.15 4-Bromopyridine-2,6-dicarboxylic acid dihydrazide (**15**)*

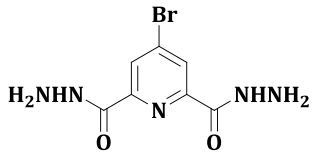


A solution of **14** (600 mg, 2.0 mmol) in ethanol (11 ml) was treated with hydrazine monohydrate (0.3 ml, 3 equiv.) and stirred at 80°C for 2h. The white suspension was filtered hot and the resulting precipitate was washed with ethanol and dried *in vacuo* to yield **15** as a colorless solid (500 mg, 92%). $^1$H-NMR (400 MHz, $d_6$-DMSO): 10.68 (*s br*, 2 H, NH), 8.25 (*s*, 2 arom. H), 4.69 (*s br*, 4 H, $NH_2$); $^{13}$C-NMR (100 MHz, $d_6$-DMSO): 160.57, 149.73, 134.95, 126.37.

*8.3.16 4-Bromo-2,6-diaminopyridine (**16**)*

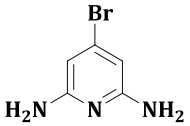

A suspension of **15** (500 mg, 1.82 mmol) in $H_2O$ (16 ml) was treated with HCl (32%, 0.8 ml) at room temperature. The resulting mixture was cooled to 0°C before $NaNO_2$ (227 mg, 3.29 mmol) in $H_2O$ (1.2 ml) was added dropwise. The pH was adjusted to 8 by the addition of saturated $NaHCO_3$. The resulting colorless solid was isolated by vacuum filtration and washed with $H_2O$. Without further purification the residue was dissolved in $CHCl_3$, dried with $MgSO_4$. After removal of the solvent under reduced pressure below 10°C, the colorless solid was dissolved in tert-butanol/toluene (1:5, 6 ml) and the resulting solution was refluxed for 19 h. The solvent was removed under reduced pressure and the resulting crude was purified by flash chromatography (toluene/EtOAc 8:1). The resulting colorless solid was dissolved in toluene, TFA (308 µl) was added, and the solution was refluxed for 2h. The solvent was removed under reduced pressure and the resulting crude was purified by flash chromatography (DCM/methanol 9:1) to yield **16** as a colorless solid (308 mg, 90 %). $^1$H-NMR (400 MHz, $CDCl_3$): 6.05 (*s*, 2 arom. H); 4.29 (*s br*, 4 H, $NH_2$).

*8.3.17 3,5-Dibromo-2,6-diaminopyridine (**17**)*

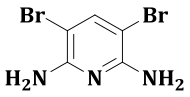

2,6-diaminopyridine (200 mg, 1.83 mmol) and NBS (652 mg, 2 equiv.) were stirred in DMF at 25 °C for 17 h. The reaction mixture was poured into $H_2O$ (80ml) before the product was extracted with DCM. The organic phase was washed with aqueous LiCl (5 %) and aqueous HCl (0.5 N) and dried over $MgSO_4$. The solvent was removed under reduced pressure to yield **17** (293 mg, 60 %). $^1$H-NMR (400 MHz, $d_6$-DMSO) 7.61 (*s*, 1 arom. H), 5.92 (*s br*, 4 H, $NH_2$).

*8.3.18 Tetrabromo-HpH$_2$Zn(OTf)$_2$ (**18**)*

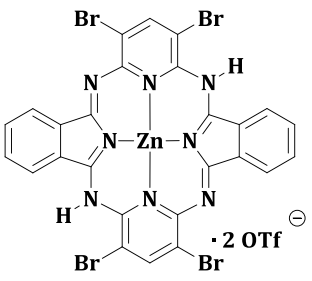

NBS (356 mg, 5 equiv.) was added to **3** (200 mg, 0.40 mmol) in DMF (1 ml). The resulting mixture was stirred at room temperature for 4h before it was layered with hexane (2 ml). The resulting precipitate was isolated by centrifugation and repeatedly washed with DCM. **6** was obtained as red solid in 42 % yield (138 mg). $^1$H-NMR (400 MHz, $d_6$-DMSO) 8.46 (*s*, 2 H), 7.83 - 7.81 (*m*, 4 H), 7.68 - 7.66 (*m*, 4 H).

# *LIST OF ABBREVIATIONS AND SYMBOLS*

***Abbreviations:***

| | |
|---|---|
| A | Adenine |
| C | Cytosine |
| CD | Circular Dichroism |
| CF | Correction Factor |
| DCM | Dichloromethane |
| DMF | N,N-Dimethylformamide |
| DMSO | Dimethylsulfoxide |
| DNA | Desoxyribonucleic Acid |
| ESI | Electrospray Ionisation |
| ESIPT | Excited State Intramolecular Proton Transfer |
| $Et_2O$ | Diethyl ether |
| EtOAc | Ethyl acetate |
| G | Guanine |
| Hp | Hemiporphyrazine |
| IC | Internal Conversion |
| ICT | Isothermal Calorimetry |
| IR | Infrared |
| LMCT | Ligand-to-metal Charge Transfer |
| MHp | Metallo Hemiporphyrazine |
| MeOH | Methanol |
| NBS | N-Bromosuccinimide |
| NLO | Non Linear Optics |
| NMR | Nucleic Magnetic Resonance Spectroscopy |
| Pc | Phthalocyanine |

| | |
|---|---|
| RNA | Ribonucleic Acid |
| SPR | Surface Plasmon Resonance |
| T | Thymine |
| TABC | Tetraazabacteriochlorin |
| TAC | Tetraazachlorin |
| TAiBC | Tetraazaisobacteriochlorin |
| TAP | Tetraazaporphyrin |
| TMPyP4 | *meso*-5,10,15,20-tetrakis-(N-methyl-4-pyridyl)porphine |
| UV/Vis | Ultraviolet/Visible |
| Zn-DIGP | Zinc tetrakis-(diisopropylguanidine) phthalocyanine |

***Symbols***

| | |
|---|---|
| $\delta$ | Chemical Shift |
| $\varepsilon$ | Molar Extinction Coefficient |
| $\lambda_{ex}$ | Excitation Wavelength |

# *REFERENCES*


1. Dahm, R., *Discovering DNA: Friedrich Miescher and the early years of nucleic acid research.* Human Genetics, 2008. **122**(6): p. 565-581.
2. Watson, J.D. and F.H.C. Crick, *Molecular Structure of Nucleic Acids: A Structure for Deoxyribose Nucleic Acid.* Nature, 1953. **171**(4356): p. 737-738.
3. Ghosh, A. and M. Bansal, *A glossary of DNA structures from A to Z.* Acta Crystallographica Section D, 2003. **59**(4): p. 620-626.
4. Wheeler, R. *A-DNA, B-DNA and Z-DNA*. 2007 February 9th 1007; Available from: http://en.wikipedia.org/wiki/File:A-DNA,_B-DNA_and_Z-DNA.png#file.
5. Franklin, R.E. and R.G. Gosling, *Molecular Configuration in Sodium Thymonucleate.* Nature, 1953. **171**(4356): p. 740-741.
6. Wang, A.H.J., et al., *Molecular structure of a left-handed double helical DNA fragment at atomic resolution.* Nature, 1979. **282**(5740): p. 680-686.
7. Herbert, A. and A. Rich, *The Biology of Left-handed Z-DNA.* Journal of Biological Chemistry, 1996. **271**(20): p. 11595-11598.
8. Sühnel, J., *Beyond nucleic acid base pairs: From triads to heptads.* Biopolymers, 2001. **61**(1): p. 32-51.
9. Hoogsteen, K., *The structure of crystals containing a hydrogen-bonded complex of 1-methylthymine and 9-methyladenine.* Acta Crystallographica, 1959. **12**(10): p. 822-823.
10. Leroy, J.-L., *The formation pathway of i-motif tetramers.* Nucleic Acids Research, 2009. **37**(12): p. 4127-4134.
11. Gellert, M., M.N. Lipsett, and D.R. Davies, *HELIX FORMATION BY GUANYLIC ACID.* Proceedings of the National Academy of Sciences, 1962. **48**(12): p. 2013-2018.
12. Hud, N.V., et al., *The Selectivity for K+ versus Na+ in DNA Quadruplexes Is Dominated by Relative Free Energies of Hydration: A Thermodynamic Analysis by 1H NMR†.* Biochemistry, 1996. **35**(48): p. 15383-15390.
13. Luedtke, N.W., *Targeting G-Quadruplex DNA with Small Molecules.* CHIMIA International Journal for Chemistry, 2009. **63**(3): p. 134-139.

14. Patel, D.J., A.T. Phan, and V. Kuryavyi, *Human telomere, oncogenic promoter and 5'-UTR G-quadruplexes: diverse higher order DNA and RNA targets for cancer therapeutics.* Nucleic Acids Research, 2007. **35**(22): p. 7429-7455.
15. Burge, S., et al., *Quadruplex DNA: sequence, topology and structure.* Nucleic Acids Research, 2006. **34**(19): p. 5402-5415.
16. Lane, A.N., et al., *Stability and kinetics of G-quadruplex structures.* Nucleic Acids Research, 2008. **36**(17): p. 5482-5515.
17. Blackburn, E.H., *Structure and function of telomeres.* Nature, 1991. **350**(6319): p. 569-573.
18. Sen, D. and W. Gilbert, *Formation of parallel four-stranded complexes by guanine-rich motifs in DNA and its implications for meiosis.* Nature, 1988. **334**(6180): p. 364-366.
19. Murat, P., Y. Singh, and E. Defrancq, *Methods for investigating G-quadruplex DNA/ligand interactions.* Chemical Society Reviews, 2011. **40**(11).
20. Bugaut, A. and S. Balasubramanian, *A Sequence-Independent Study of the Influence of Short Loop Lengths on the Stability and Topology of Intramolecular DNA G-Quadruplexes†.* Biochemistry, 2007. **47**(2): p. 689-697.
21. J.L, H., *Hunting G-quadruplexes.* Biochimie, 2008. **90**(8): p. 1140-1148.
22. Qin, Y. and L.H. Hurley, *Structures, folding patterns, and functions of intramolecular DNA G-quadruplexes found in eukaryotic promoter regions.* Biochimie, 2008. **90**(8): p. 1149-1171.
23. Maizels, N., *Dynamic roles for G4 DNA in the biology of eukaryotic cells.* Nat Struct Mol Biol, 2006. **13**(12): p. 1055-1059.
24. Oganesian, L. and T.M. Bryan, *Physiological relevance of telomeric G-quadruplex formation: a potential drug target.* BioEssays, 2007. **29**(2): p. 155-165.
25. McEachern, M.J., A. Krauskopf, and E.H. Blackburn, *TELOMERES AND THEIR CONTROL.* Annual Review of Genetics, 2000. **34**(1): p. 331-358.
26. Williamson, J.R., *G-Quartet Structures in Telomeric DNA.* Annual Review of Biophysics and Biomolecular Structure, 1994. **23**(1): p. 703-730.
27. Griffith, J.D., et al., *Mammalian Telomeres End in a Large Duplex Loop.* Cell, 1999. **97**(4): p. 503-514.
28. Roth, P.J.C., *Synthesis and Evaluation of Guanidino Phthalocyanines for G-quadruplex Binding*, in *Organic Chemistry*. 2008, University of Zürich: Zürich.
29. Shay, J.W. and W.E. Wright, *Telomerase therapeutics for cancer: challenges and new directions.* Nat Rev Drug Discov, 2006. **5**(7): p. 577-584.

30. Siddiqui-Jain, A., et al., *Direct evidence for a G-quadruplex in a promoter region and its targeting with a small molecule to repress c-MYC transcription.* Proceedings of the National Academy of Sciences, 2002. **99**(18): p. 11593-11598.
31. Fernando, H., et al., *A Conserved Quadruplex Motif Located in a Transcription Activation Site of the Human c-kit Oncogene.* Biochemistry, 2006. **45**(25): p. 7854-7860.
32. Cogoi, S. and L.E. Xodo, *G-quadruplex formation within the promoter of the KRAS proto-oncogene and its effect on transcription.* Nucleic Acids Research. **34**(9): p. 2536-2549.
33. Mergny, J.-L., et al., *Natural and pharmacological regulation of telomerase.* Nucleic Acids Research, 2002. **30**(4): p. 839-865.
34. Javier, C., A.R. Martin, and N. Stephen, *The Design of G-quadruplex Ligands as Telomerase Inhibitors.* Mini Reviews in Medicinal Chemistry, 2003. **3**(1): p. 11-21.
35. De Cian, A., et al., *Targeting telomeres and telomerase.* Biochimie, 2008. **90**(1): p. 131-155.
36. Monchaud, D. and M.-P. Teulade-Fichou, *A hitchhiker's guide to G-quadruplex ligands.* Organic & Biomolecular Chemistry, 2008. **6**(4).
37. Doherty, K.M., et al., *Tetraplex Binding Molecules as Anti-Cancer Agents.* Recent Patents on Anti-Cancer Drug Discovery, 2006. **1**(2): p. 185-200.
38. Tan, J.-H., L.-Q. Gu, and J.-Y. Wu, *Design of Selective G-quadruplex Ligands as Potential Anticancer Agents.* Mini Reviews in Medicinal Chemistry, 2008. **8**(11): p. 1163-1178.
39. Ou, T.-m., et al., *G-Quadruplexes: Targets in Anticancer Drug Design.* ChemMedChem, 2008. **3**(5): p. 690-713.
40. Georgiades, S.N., et al., *Interaction of Metal Complexes with G-Quadruplex DNA.* Angewandte Chemie International Edition, 2010. **49**(24): p. 4020-4034.
41. Haider, S.M., G.N. Parkinson, and S. Neidle, *Structure of a G-quadruplex–Ligand Complex.* Journal of Molecular Biology, 2003. **326**(1): p. 117-125.
42. Gavathiotis, E., et al., *Recognition and Stabilization of Quadruplex DNA by a Potent New Telomerase Inhibitor: NMR Studies of the 2:1 Complex of a Pentacyclic Methylacridinium Cation with d(TTAGGGT)4.* Angewandte Chemie International Edition, 2001. **40**(24): p. 4749-4751.
43. Fedoroff, O.Y., et al., *NMR-Based Model of a Telomerase-Inhibiting Compound Bound to G-Quadruplex DNA†.* Biochemistry, 1998. **37**(36): p. 12367-12374.
44. Reed, J., et al., *TRAP–LIG, a modified telomere repeat amplification protocol assay to quantitate telomerase inhibition by small molecules.* Analytical Biochemistry, 2008. **380**(1): p. 99-105.

45. De Cian, A., et al., *Reevaluation of telomerase inhibition by quadruplex ligands and their mechanisms of action.* Proceedings of the National Academy of Sciences, 2007. **104**(44): p. 17347-17352.
46. Grand, C.L., et al., *The Cationic Porphyrin TMPyP4 Down-Regulates c-MYC and Human Telomerase Reverse Transcriptase Expression and Inhibits Tumor Growth in Vivo 1 This research was supported by grants from the NIH and the Arizona Disease Control Research Commission.1.* Molecular Cancer Therapeutics, 2002. **1**(8): p. 565-573.
47. Izbicka, E., et al., *Effects of Cationic Porphyrins as G-Quadruplex Interactive Agents in Human Tumor Cells.* Cancer Research, 1999. **59**(3): p. 639-644.
48. Freyer, M.W., et al., *Biophysical Studies of the c-MYC NHE III1 Promoter: Model Quadruplex Interactions with a Cationic Porphyrin.* Biophysical journal, 2007. **92**(6): p. 2007-2015.
49. Izbicka, E., et al., *Telomere-interactive agents affect proliferation rates and induce chromosomal destabilization in sea urchin embryos.* Anti-Cancer Drug Design, 1999. **14**(4): p. 355-365.
50. Membrino, A., et al., *Cellular uptake and binding of guanidine-modified phthalocyanines to KRAS/HRAS G-quadruplexes.* Chemical Communications, 2010. **46**(4).
51. Shin-ya, K., et al., *Telomestatin, a Novel Telomerase Inhibitor from Streptomyces anulatus.* Journal of the American Chemical Society, 2001. **123**(6): p. 1262-1263.
52. Martino, L., et al., *Structural and Thermodynamic Studies of the Interaction of Distamycin A with the Parallel Quadruplex Structure [d(TGGGGT)]4.* Journal of the American Chemical Society, 2007. **129**(51): p. 16048-16056.
53. Pelton, J.G. and D.E. Wemmer, *Binding modes of distamycin A with d(CGCAAATTTGCG)2 determined by two-dimensional NMR.* Journal of the American Chemical Society, 1990. **112**(4): p. 1393-1399.
54. Chen, X., B. Ramakrishnan, and M. Sundaralingam, *Crystal structures of the side-by-side binding of distamycin to AT-containing DNA octamers d(ICITACIC) and d(ICATATIC).* Journal of Molecular Biology, 1997. **267**(5): p. 1157-1170.
55. Rodriguez, R., et al., *Ligand-Driven G-Quadruplex Conformational Switching By Using an Unusual Mode of Interaction.* Angewandte Chemie International Edition, 2007. **46**(28): p. 5405-5407.
56. Leonard, G.A., et al., *Self-association of a DNA loop creates a quadruplex: crystal structure of d(GCATGCT) at 1.8 å resolution.* Structure, 1995. **3**(4): p. 335-340.
57. Salisbury, S.A., et al., *The bi-loop, a new general four-stranded DNA motif.* Proceedings of the National Academy of Sciences, 1997. **94**(11): p. 5515-5518.

58. Kettani, A., A.R. Kumar, and D.J. Patel, *Solution Structure of a DNA Quadruplex Containing the Fragile X Syndrome Triplet Repeat.* Journal of Molecular Biology, 1995. **254**(4): p. 638-656.
59. Kettani, A., et al., *Solution structure of a Na cation stabilized DNA quadruplex containing G·G·G·G and G·C·G·C tetrads formed by G-G-G-C repeats observed in adeno-associated viral DNA.* Journal of Molecular Biology, 1998. **282**(3): p. 619-636.
60. Bouaziz, S., A. Kettani, and D.J. Patel, *A K cation-induced conformational switch within a loop spanning segment of a DNA quadruplex containing G-G-G-C repeats.* Journal of Molecular Biology, 1998. **282**(3): p. 637-652.
61. Arthanari, H. and P.H. Bolton, *Functional and dysfunctional roles of quadruplex DNA in cells.* Chemistry & Biology, 2001. **8**(3): p. 221-230.
62. Fiel, R.J., et al., *Interaction of DNA with a porphyrin ligand: evidence for intercalation.* Nucleic Acids Research, 1979. **6**(9): p. 3093-3118.
63. Han, F.X., R.T. Wheelhouse, and L.H. Hurley, *Interactions of TMPyP4 and TMPyP2 with Quadruplex DNA. Structural Basis for the Differential Effects on Telomerase Inhibition.* Journal of the American Chemical Society, 1999. **121**(15): p. 3561-3570.
64. Monchaud, D., et al., *“One Ring to Bind Them All”—Part I: The Efficiency of the Macrocyclic Scaffold for G-Quadruplex DNA Recognition.* Journal of Nucleic Acids, 2010. **2010**.
65. Elvidge, J.A. and R.P. Linstead, *976. Conjugated macrocycles. Part XXIV. A new type of cross-conjugated macrocycle, related to the azaporphins.* Journal of the Chemical Society (Resumed), 1952.
66. Fernández-Lázaro, F., et al., *Hemiporphyrazines as Targets for the Preparation of Molecular Materials: Synthesis and Physical Properties.* Chemical Reviews, 1998. **98**(2): p. 563-576.
67. Honeybourne, C.L., et al., *Nontemplate Syntheses of Complexes with Conjugated Mackocyclic Ligands*, in *Inorganic Syntheses*. 2007, John Wiley & Sons, Inc. p. 44-49.
68. Attanasio, D., I. Collamati, and E. Cervone, *Synthesis, characterization, and spectroscopic studies of some metal derivatives of hemiporphyrazine.* Inorganic Chemistry, 1983. **22**(22): p. 3281-3287.
69. Haberroth, K., et al., *Synthese und Charakterisierung neuer Hemiporphyrazinato-Nickelkomplexe.* Chemische Berichte, 1995. **128**(4): p. 417-421.
70. Hanack, M., K. Haberroth, and M. Rack, *Synthese und Charakterisierung von substituierten Nickelhemiporphyrazinen.* Chemische Berichte, 1993. **126**(5): p. 1201-1204.

71. Collamati, I. and E. Cervone, *Some μ-oxo compounds of iron-hemiporphyrazine. Synthesis and properties.* Inorganica Chimica Acta, 1986. **123**(3): p. 147-154.
72. Esposito, J.N., L.E. Sutton, and M.E. Kenney, *Infrared and nuclear magnetic resonance studies of some germanium phthalocyanines and hemiporphyrazines.* Inorganic Chemistry, 1967. **6**(6): p. 1116-1120.
73. Sakata, K., et al., *Characterization and spectral properties of oxovanadium(IV), palladium(II) and lead(II) complexes of hemiporphyrazine.* Inorganica Chimica Acta, 1989. **156**(1): p. 1-5.
74. Dini, D., et al., *Large Two-Photon Absorption Cross Sections of Hemiporphyrazines in the Excited State: The Multiphoton Absorption Process of Hemiporphyrazines with Different Central Metals.* Journal of the American Chemical Society, 2008. **130**(37): p. 12290-12298.
75. Sripothongnak, S., et al., *Synthesis and Characterization of Lithium Hemiporphyrazines.* Inorganic Chemistry, 2009. **48**(4): p. 1293-1300.
76. Sutton, L.E. and M.E. Kenney, *Infrared and nuclear magnetic resonance studies of some tin phthalocyanines and hemiporphyrazines.* Inorganic Chemistry, 1967. **6**(10): p. 1869-1872.
77. Peng, S.-M., et al., *Structural Relationships Between The Hemiporphyrazine Macrocyclic Ligand and Its Metal Complexes II. Planar Neutral Ligand, $C_{26}H_{16}N_8$, and Four Isomorphous Metal Complexes, [M($C_{26}H_{14}N_8$)($H_2O$)], M=Mn(II), Co(II), Cu(II), Zn(II).* Journal Chinese Chemical Society, 1986. **33**: p. 23-33.
78. Speakman, J., *The crystal structure of an analogue of nickel phthalocyanine.* Acta Crystallographica, 1953. **6**(10): p. 784-791.
79. Peng, S.-M., et al., *Structural Relationships Between The Hemiporphyrazine Macrocyclic Ligand And Its Metal Complexes I. Saddle Shaped Neutral Ligand Hydrate, $C_{26}H_{26}N_8.H_2O$, and Nickel Complex, [Ni($C_{26}H_{14}N_8$)].* Journal Chinese Chemical Society, 1986. **33**: p. 13-21.
80. Rack, M. and M. Hanack, *Ladder Polymers and Oligomers Based on Hemiporphyrazine.* Angewandte Chemie International Edition in English, 1994. **33**(15-16): p. 1646-1648.
81. Ruff, D.H., S. Fiedler, and M. Hanack, *Synthesis and characterization of new bis-dienophiles for Diels-Alder-polymerization.* Synthetic Metals, 1995. **69**(1–3): p. 579-580.
82. Rack, M., B. Hauschel, and M. Hanack, *Nickel Hemiporphyrazines as Bisdienes and Bisdienophiles: Synthesis and Characterization.* Chemische Berichte, 1996. **129**(2): p. 237-242.

83. Dirk, C.W. and T.J. Marks, *Cofacial assembly of partially oxidized metallomacrocycles as an approach to controlling lattice architecture in low-dimensional molecular solids. Synthesis and properties of cofacially joined silicon and germanium hemiporphyrazine polymers.* Inorganic Chemistry, 1984. **23**(25): p. 4325-4332.
84. Honeybourne, C.L. and R.J. Ewen, *Closed-shell crystal orbital calculations on columnar stacks of conjugated macrocyclic ligands.* Journal of Physics and Chemistry of Solids, 1984. **45**(4): p. 433-438.
85. Honeybourne, C.L. and R.J. Ewen, *Dark DC conductivity and spectroscopy of clean and gas doped thin films of organic semiconductors.* Journal of Physics and Chemistry of Solids, 1983. **44**(3): p. 215-223.
86. Honeybourne, C.L. and R.J. Ewen, *The enhancement of dark d.c. conductivity by gas adsorption on thin films of macrocyclic copper complexes.* Journal of Physics and Chemistry of Solids, 1983. **44**(8): p. 833-838.
87. Campaci, F. and S. Campestrini, *Catalytic olefin epoxidations with KHSO5: the first report on manganese hemiporphyrazines as catalysts in oxygenation reactions.* Journal of Molecular Catalysis A: Chemical, 1999. **140**(2): p. 121-130.
88. Kadish, K.M., K. Smith, and R. Guilard, *Handbook of Porphyrins and Related Macrocycles*. Vol. 15. 2003: Academic Press: Burlington, MA. 364.
89. Agostinelli, E., et al., *Hemiporphyrazine, a porphyrin-related macrocycle that induces rhombically compressed stereochemistries: structure and properties of bis(pyridine)(hemiporphyrazinato)nickel(II).* Inorganic Chemistry, 1984. **23**(8): p. 1162-1165.
90. Collamati, I., E. Cervone, and R. Scoccia, *Synthesis and reactivity of some Fe(II) and Mn(II) complexes with hemiporphyrazine.* Inorganica Chimica Acta, 1985. **98**(1): p. 11-17.
91. Bossa, M., et al., *On the electronic states of the extended porphyrin family.* Journal of Molecular Structure: THEOCHEM, 1995. **342**(1): p. 73-86.
92. Zakharov, A.V., M.G. Stryapan, and M.K. Islyaikin, *Structure, electronic and vibrational spectra and aromaticity of hemiporphyrazine and its hydrates: A density functional theory study.* Journal of Molecular Structure: THEOCHEM, 2009. **906**(1-3): p. 56-62.
93. Altucci, C., et al., *Excited state intramolecular proton transfer in free base hemiporphyrazine.* Chemical Physics Letters, 2002. **354**(1–2): p. 160-164.
94. Persico, V., M. Carotenuto, and A. Peluso, *The Photophysics of Free-Base Hemiporphyrazine: A Theoretical Study.* The Journal of Physical Chemistry A, 2004. **108**(18): p. 3926-3931.

95. Peluso, A., C. Garzillo, and G. Del Re, *Radiationless decay via ESIPT of the first excited singlet of the hemiporphyrazine.* Chemical Physics, 1996. **204**(2–3): p. 347-351.
96. Chizhik, A.M., et al., *Optical imaging of excited-state tautomerization in single molecules.* Physical Chemistry Chemical Physics, 2011. **13**(5).
97. Dini, D., et al., *Demonstration of the optical limiting effect for an hemiporphyrazine.* Chemical Communications, 2006(22): p. 2394.
98. Zimmermann, J., et al., *Excitonic Coupling between B and Q Transitions in a Porphyrin Aggregate.* The Journal of Physical Chemistry B, 2003. **107**(25): p. 6019-6021.
99. Sissa, C., et al., *Fluorescence Anisotropy Spectra Disclose the Role of Disorder in Optical Spectra of Branched Intramolecular-Charge-Transfer Molecules.* The Journal of Physical Chemistry B, 2011. **115**(21): p. 7009-7020.
100. Kobayashi, N. and A.B.P. Lever, *Cation or solvent-induced supermolecular phthalocyanine formation: crown ether substituted phthalocyanines.* Journal of the American Chemical Society, 1987. **109**(24): p. 7433-7441.
101. Van Duuren, B.L. and C.E. Bardi, *Reflectance Fluorescence Spectra of Aromatic Compounds in Potassium Bromide Pellets.* Analytical Chemistry, 1963. **35**(13): p. 2198-2202.
102. Wyman, G.M., *Measurement of Solid Samples on the Cary Spectrophotometer.* J. Opt. Soc. Am., 1955. **45**(11): p. 965-966.
103. Perez-Morales, M., et al., *Soret emission from water-soluble porphyrin thin films: effect on the electroluminescence response.* Journal of Materials Chemistry, 2009. **19**(24).
104. Fujitsuka, M., et al., *S2- and S1-states properties of zinc porphyrin polypeptides.* Journal of Photochemistry and Photobiology A: Chemistry, 2007. **188**(2–3): p. 346-350.
105. Akimoto, S., et al., *Excitation relaxation of zinc and free-base porphyrin probed by femtosecond fluorescence spectroscopy.* Chemical Physics Letters, 1999. **309**(3–4): p. 177-182.
106. Ficken, G.E., et al., *789. Conjugated macrocycles. Part XXXI. Catalytic hydrogenation of tetrazaporphins, with a note on its stereochemical course.* Journal of the Chemical Society (Resumed), 1958.
107. Fukuda, T. and N. Kobayashi, *Hydrogenated tetraazaporphyrins-old but new core-modified phthalocyanine analogues.* Dalton Transactions, 2008(35).
108. Fukuda, T., et al., *Synthesis and Spectroscopic and Electrochemical Studies of Novel Benzo- or 2,3-Naphtho-Fused Tetraazachlorins, Bacteriochlorins, and Isobacteriochlorins.* Chemistry - A European Journal, 2004. **10**(1): p. 117-133.

109. Makarova, E.A., et al., *Synthesis, Spectroscopic, and Electrochemical Studies of 1,2-Naphthalene-Ring-Fused Tetraazachlorins, -bacteriochlorins, and -isobacteriochlorins: The Separation and Characterization of Structural Isomers.* Chemistry - A European Journal, 2005. **11**(4): p. 1235-1250.

110. Makarova, E.A. and E.A. Lukyanets, *ChemInform Abstract: Design and Synthesis of Tetraazachlorins, Tetraazabacteriochlorins and Tetraazaisobacteriochlorins.* ChemInform, 2010. **41**(19): p. no-no.

111. Ruf, M., W.S. Durfee, and C.G. Pierpont, *Synthesis of a quinone-functionalized macrocyclic ligand and the intense fluorescence of its zinc complex.*Chemical Communications, 2004(8): p. 1022.

112. Aranyos, V., A. Castano, and H. Grennberg, *An Application of the Stille Coupling for the Preparation of Arylated Phthalonitriles and Phthalocyanines.* Acta Chemica Scandinavica, 1999. **53**: p. 714-720.

113. Cong, F.-D., et al., *Facile synthesis, characterization and property comparisons of tetraaminometallophthylocyanines with and without intramolecular hydrogen bonds.* Dyes and Pigments, 2005. **66**(2): p. 149-154.

114. Nettekoven, M. and C. Jenny, *The Development of a Practical and Reliable Large-Scale Synthesis of 2,6-Diamino-4-bromopyridine.* Organic Process Research & Development, 2002. **7**(1): p. 38-43.

115. Geiger, D.K. and R.G. Schmidt, *The synthesis of water-soluble hemiporphyrazine analogues.* Inorganica Chimica Acta, 1992. **197**(2): p. 203-207.

116. Dumas, A. and N.W. Luedtke, *Highly fluorescent guanosine mimics for folding and energy transfer studies.* Nucleic Acids Research, 2011. **39**(15): p. 6825-6834.

# *APPENDIX*

$^{1}$H-NMR spectrum of $HpH_2$ (**1**) in $d_6$-DMSO:

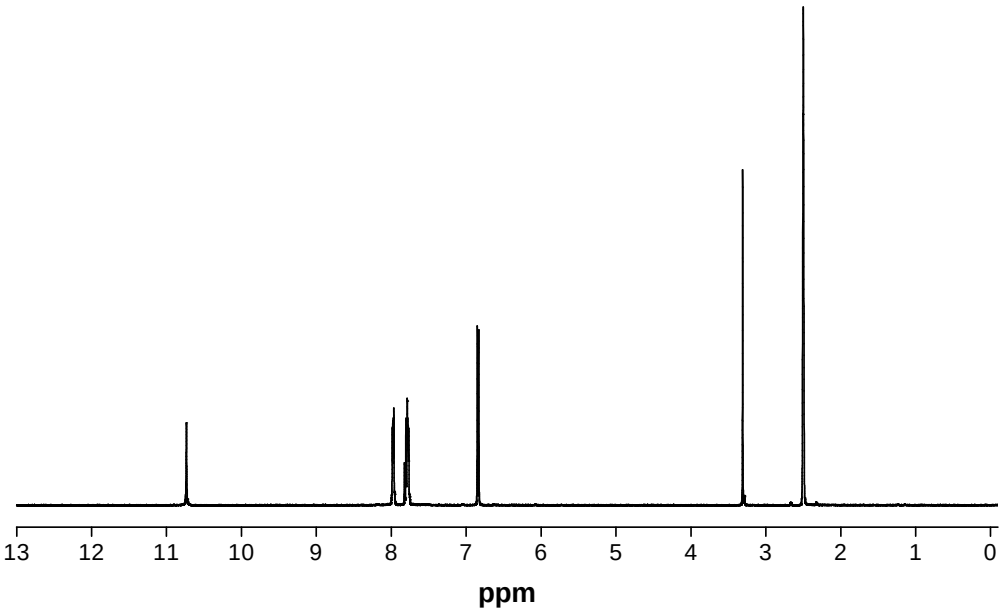


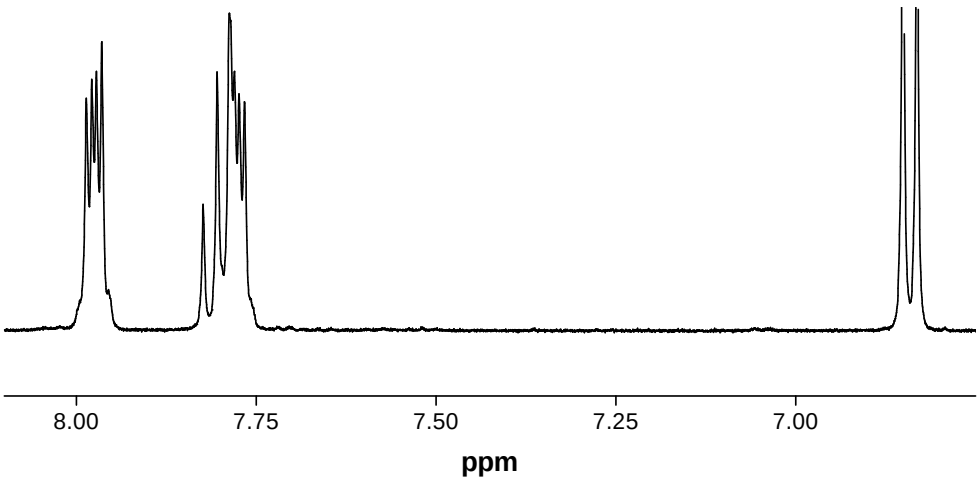

$^{1}$H-NMR spectrum of $HpH_2Zn(OTf)_2$ (**3**) in MeOD:

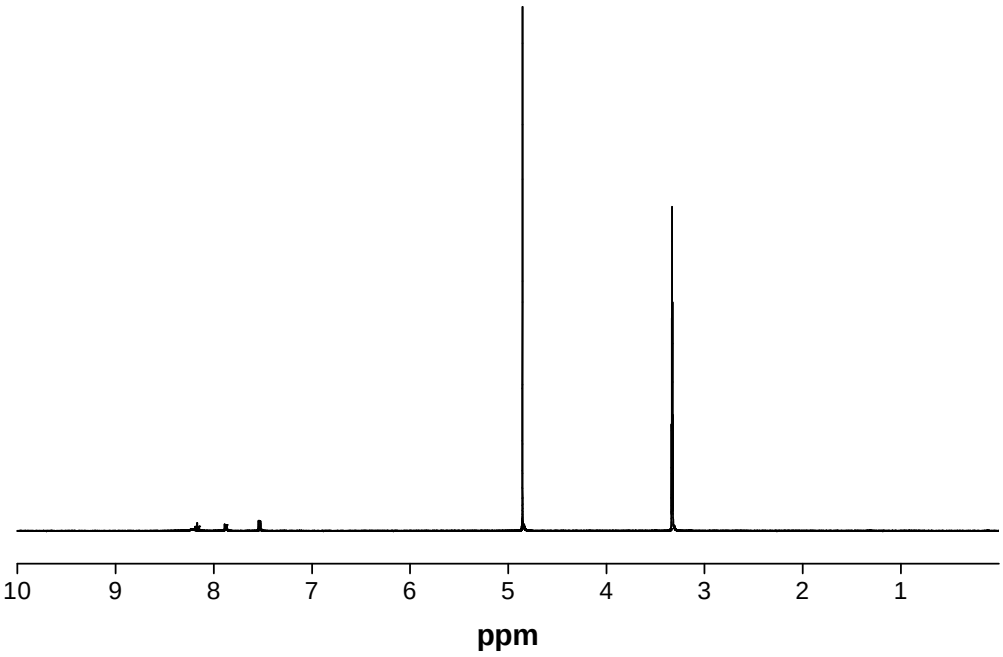


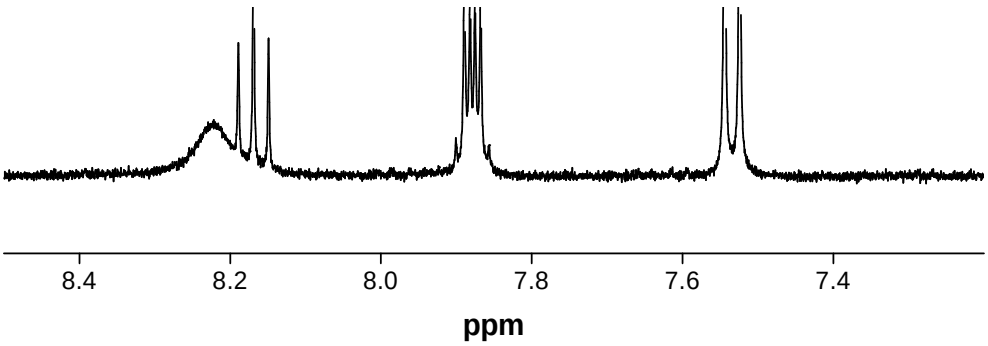

$^{1}$H-NMR spectrum of $HpH_4Zn(OTf)_2$ (**5**) in MeOD:

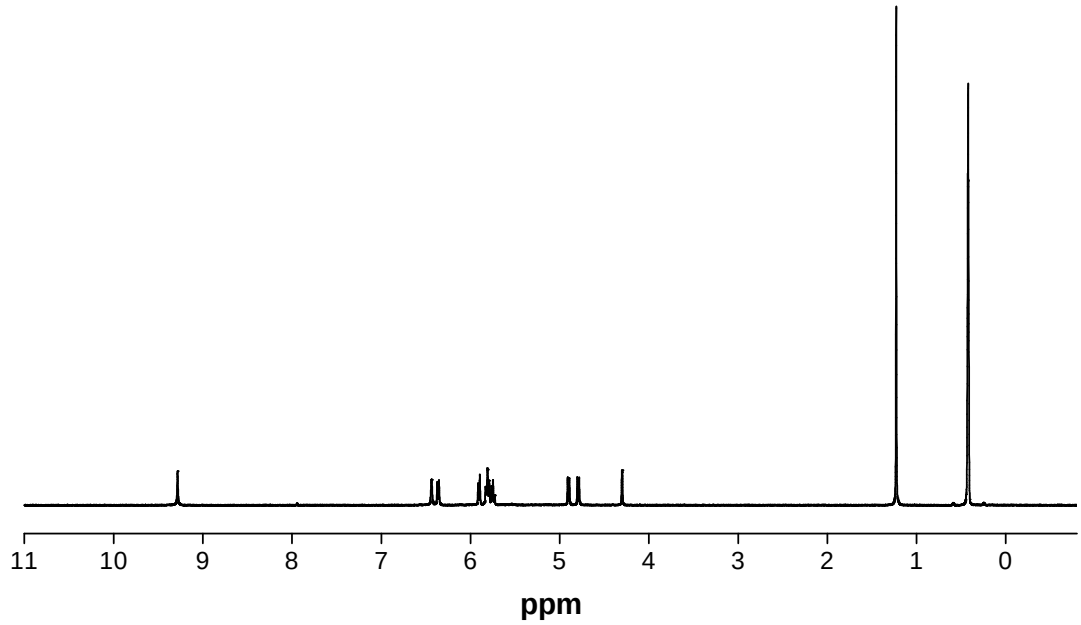


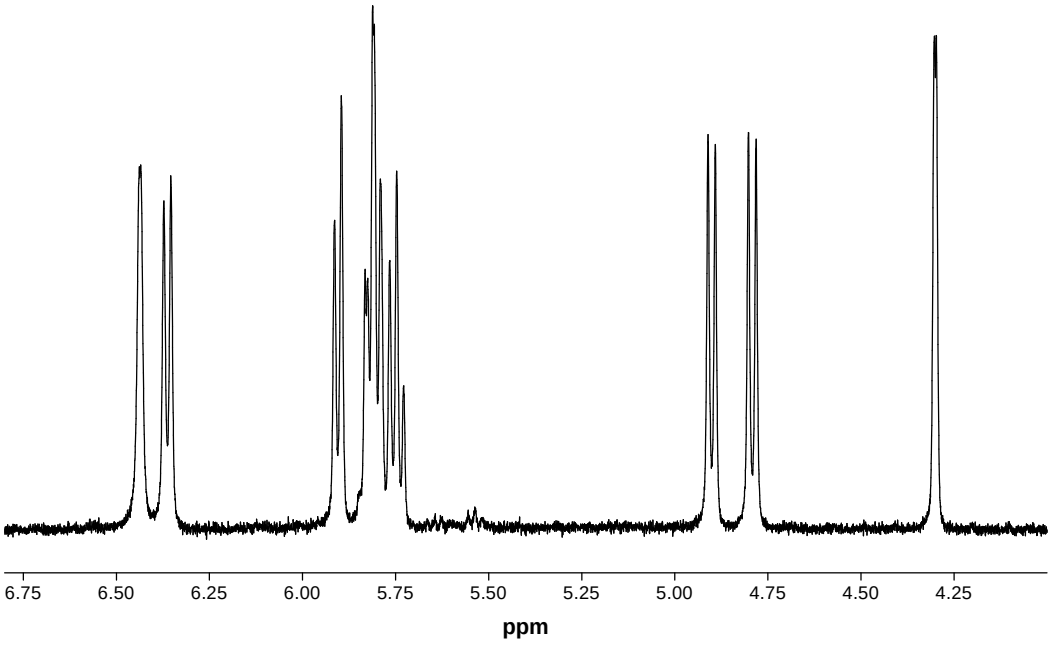

$^{1}$H-NMR spectrum of nitro-substituted Hp (**10**) in $d_6$-DMSO: